NTNU

Norwegian University of
Science and Technology

Seakeeping Analysis Comparison Between Viscous And Inviscid CFD

Joakim Tveiten Vigsnes

Marine Technology
Submission date: June 2018
Supervisor: Håvard Holm, IMT
Co-supervisor: Hans Jørgen Mørch, CFD Marine

Norwegian University of Science and Technology
Department of Marine Technology

NTNU
Norges teknisk-naturvitenskapelige universitet
Institutt for marin teknikk

HOVEDOPPGAVE I MARIN HYDRODYNAMIKK

Vår 2018

FOR

Stud.techn. Joakim Tveiten Vigsnes

Sammenlikning av ikke-viskøs og viskøs seakeeping-simulering av skip

Informasjon om hvilken tilleggsmotstand et skip opplever i en gitt sjøkondisjon er viktig i forbindelse med skrog-optimalisering. Eksisterende potensialteori-verktøy gir estimater på bevegelser og motstand med varierende grad av presisjon. Viskøs CFD vil kunne utfylle potensialteori, men er tidkrevende. Det er behov for verktøy som både er presist og tidseffektivt.

Kandidaten skal evaluere anvendbarheten til ikke-viskøse CFD seakeeping simuleringer. Dette vil blir gjennomført ved å gjøre og sammenlikne ikke-viskøse og viskøse CFD simuleringer av KVLCC2-skipet i regulære bølger. Dette skal gjennomføres ved bruk av softwaren STAR-CCM+. Oppgaven er begrenset til en skipsmodell, og en motsjøkondisjon, stille-vann og bølger, og en skråsjø kondisjon, grunnet mengden tid til rådighet. Kandidaten skal redegjøre for hvordan andre sjøkondisjoner og skrog kunne endret resultatene og gi anbefalinger til videre arbeid.

Det forutsettes at Institutt for marin teknikk, NTNU, fritt kan benytte resultatene i sitt forskningsarbeid, da med referanse til studentens arbeid.

Besvarelsen redigeres mest mulig som en forskningsrapport med resymé, konklusjon, litteraturliste etc. Ved utarbeidelsen av teksten skal kandidaten legge vekt på å gjøre den så kort, oversiktlig og velskrevet som mulig.

Besvarelsen leveres i ett eksemplar innen 25. juni 2018.

Håvard Holm
1.amanueensis

Preface

This thesis marks the end of the five years I have spent at the Norwegian University of Science and Technology (NTNU), doing my masters degree at the Department of Marine Technology. Throughout my studies, a common denominator has been my fascination for the hydrodynamic environment an arbitrary body is subjected to at sea. Naturally, this interest made me choose hydrodynamics as my specialty. Coupled with a curiosity for computational fluid dynamics, (CFD) this thesis epitomizes my academical inclination. I felt that combining ship hydrodynamics with CFD would bring me to the technological forefront of seakeeping analysis. With the work I have done for this thesis I feel that I have surpassed the original scope of understanding I had hoped to achieve. I have obtained a profound motivation for continuing my education within the hydrodynamic field, and I am certain that what I have learned during my master thesis, will be of great value to me in the coming years.

1. amuensis Håvard Holm has been a great supervisor during my master thesis. Both offering his expertise and time, in addition to motivation, he has helped me towards achieving the thesis I wanted.

The simulations performed in this thesis would not have been possible without the help of Hans-Jørgen Mørch. He has been a great help to me as a co-supervisor on the thesis, lending in abundance both his computational resources and experience whenever the need arose.

Lastly, I would like to extend my gratitude to Sintef Ocean, and even more spesifically to Haakon-Elizabeth Lindstad and Sverre Anders Alterskjær. Lindstad set me on the path of this master thesis, and both gave me great advice with regards to formulating the scope of the thesis.

Trondheim, 25.06.2018

Joakim Tveiten Vigsnes

Sammendrag

I dagens samfunn er det stort fokus på å skape et grønnere og mer bærekraftig miljø. Dette har ført til strengere krav til energiøkonomisk skipsdesign. For å imøtekomme disse kravene trengs det mer kunnskap om hvordan et skip responderer på ulike realistiske sjøkondisjoner. Presise beregninger på kondisjoner har vært tilskrevet modeltesting, og viskøse CFD simuleringer. Da tid er en begrenset ressurs innen ingeniør-virksomhet, og både modelltester og viskøs CFD er tidkrevende prosesser, vil det ha stor verdi å finne frem til mer presise og tids-effektive metoder.

Denne oppgaven utforsker muligheten for å benytte ikke-viskøse CFD simuleringer til seakeeping-analyser. Ettersom bølgemotstand og skipsbevegelser er ansett for å være trykk-dominerte fenomener, så er hypotesen at en ikke-viskøs - og viskøs simulering burde gi relativt like resultater på slike analyser. Både ikke-viskøse og viskøse simuleringer er gjort for stille-vann kondisjoner og bølger i ren motsjø og skråsjø.

Modellen brukt i analysene er skipsmodellen KVLCC2, i en skala på 1:58, og den kommersielle softwaren STAR-CCM+ er blitt brukt til å gjennomføre simuleringene. Eksperimentelle resultater er hentet fra CFD Workshop'en i Gøteborg fra 2010, for stille-vanns og motsjøkondisjonene. Ettersom det ikke fantes tilgjengelig publisert eksperimentell data på skråsjø analyser, var det viktig at resultatene fra de to andre kondisjonene samstemte med de eksperimentelle verdiene. Hvis det var tilfelle, så ville det numeriske oppsettet være validert, og resultatene fra skråsjø-simuleringene ville følgelig være mer troverdige.

En numerisk slepetank har blitt satt opp, og en flat-VOF og en 5te ordens tilnærming av Stokes bølgen er blitt brukt til å modellere fri overflate for henholdsvis stille-vann og bølgekjøringene. Overset mesh-teknikken er blitt brukt i bølgekjøringene, for å ta hensyn til de store bevegelsene som finner sted. Modellen var satt til å kunne bevege seg i hiv og stamp i stille-vann og motsjø kjøringene. I skråsjø kondisjonen var også modellen fri til å bevege seg i rull.

For stille-vanns kondisjonen klarte ikke den ikke-viskøse solveren å beregne trykk-motstanden med god presisjon, på grunn av dens avhengighet til viskøse krefter. Da den bare klarte å estimere omlag 35% av trykkraften, blir den ikke-viskøse solveren ansett for å ikke være anvendbar til slike beregninger. Grunnen til et så lavt samsvar mellom beregninger ligger i det lave Froude-tallet for modellen, Fn=0.142. Ved høyere Froude-tall er det forventet at den ikke-viskøse og viskøse simuleringen gir mer samsvarende resultater.

De endelige resultatene for bølge-kondisjonene i denne oppgaven viser at den ikke-viskøse koden klarer å beregne tillegsmotstanden og bevegelsene i bølger med en tilfredsstillende presisjon. Ved inkluderingen av stille-vanns friksjonskraften, oppnår den ikke-viskøse simuleringen et totalmotstandsavvik på 2.988% relativt til eksperimentelle resultater for mot-sjø kondisjonen. I tillegg presterte den bedre på translasjons- og rotasjonsberegninger enn en del av de andre resultatene gjengitt i CFD workshopen, [Larsson, Stern, and Visonneu 2010]. I skråsjø-kondisjonen fikk den et 4.4%, 0.06%, 5.29% og 11.9%-avvik på den 0te harmoniske amplituden relativt til den viskøse simuleringer for henholdsvis den trykkmotstanden, hiv-, rull- og stamp-bevegelsen. Begge bølgesimulerings-resultater lider av en fri-overflate modellering som gjengir en bølge som er asymmetrisk om fri-overflate ved stillevann. Til tross for dette er de gode nok til å indikere at de resulterende kreftene og bevegelsene er trykk-dominerte.

Ut fra resulatene ble det dokumentert at friksjonsmotstanden substantielt varierte med den innkommne bølgevinkelen, og at det ikke var noe tidsbesparinger for den ikke-viskøse koden i skråsjø. Uten bedre estimater for friksjonsmotstanden til flere sjøkondisjoner, og en betraktelig økning i tidseffektivitet, er den ikke-viskøse koden, basert på de oppnådde resultatene, ansett for å være uegnet til slike analyser.

Summary

With the global community's increased focus on a green and more sustainable environment, stricter demands are being invoked on ship design. Consequently, knowledge on how the vessel responds in a realistic sea-condition is needed, in order to hydrodynamically optimize the hull. Accurate calculations on this topic has been the domain of model tests and viscous CFD simulations. However, since time is of the essence with regards to engineering analysis, and both model-testing and viscous CFD simulations still are time-consuming analyses, there is a need for more efficient ways of accurate calculation.

This thesis investigates the applicability of inviscid CFD simulations to seakeeping analysis. As ship resistance and motions in waves is widely regarded as a pressure-dominated system, the hypothesis is that the inviscid simulation should not differ by too much, compared to viscous CFD results. If the two simulations concur with regards to the results, the inviscid simulation should be the preferred method, as it is computationally faster. Both an inviscid and RANS-simulation are done for calm-water, head-wave and oblique-wave condition.

The vessel used in the analyses is the ship model KVLCC2, at a 1:58 scale, and the commercial software STAR-CCM+ is used for the CFD-simulations. From the CFD workshop in Gothenburg 2010 experimental results for the calm-water and head-wave simulations were obtained. As there did not exist any published experimental results on the oblique wave-condition, it was crucial that the calm-water and head-wave simulations agreed with the experimental data. This way, the numerical set-up could be verified and the oblique-condition results would have more credibility.

A numerical wave tank was set up, and a flat VOF-wave and a 5th order approximation to the Stokes wave was used to model the calm-water and wave-simulations, respectively. The overset mesh technique has been implemented for the wave-analyses, in order to cope with the large motions that occur. The model was allowed to move in heave and pitch for the calm-water and head-wave simulations. In oblique wave conditions, the vessel was also allowed to move in roll.

For the calm water condition, the inviscid simulation was unable to compute the pressure resistance, due to the fact that the pressure resistance was dominated by viscous forces. Only able to calculate approximately 35% of the pressure force, the inviscid solver is deemed not applicable for this condition. This is due to the low Froude number of the vessel, Fn=0.142, and it is expected that for larger Froude numbers, the difference between the viscous and inviscid simulation will become smaller.

The results obtained for the wave-conditions in this thesis indicates that the inviscid solver was able to compute the resistance and motions in waves to a satisfactory level of accuracy. With the inclusion of the calm water frictional resistance a 2.988% deviancy from experimental results was obtained for the total resistance in the head-wave condition. It also achieved a level of accuracy for the motions that outperformed some of the results published in the 2010 CFD workshop, [Larsson, Stern, and Visonneu 2010]. For oblique waves it managed to obtain a 4.4%, 0.06%, 5.29% and 11.9% deviancy for the pressure resistance, heave-, roll- and pitch-motion, respectively for the 0th harmonic amplitude of the time-series. These results, along with the head-wave simulation, suffered from an asymmetric representation of the surface-elevation, around the mean-free-surface at for calm waters. Still, they do indicate that the forces and motions occurring are pressure-dominated.

It was found that the frictional resistance varied substantially with wave-heading angle, and that there was no computational gain with an inviscid solver for oblique conditions. Without a better estimate for the frictional resistance than the calm water resistance, and improved computational efficiency, the inviscid solver is deemed as not applicable, on the basis of the results obtained in this thesis.

Contents

List of Figures

Nomenclature

Abbreviations

CAD	Computer Aided Design
CAE	Computer Aided Engineering
CFD	Computational Fluid Dynamics
D.E	Discretization Error
DNS	Direct Numeric Solver
EEDI	Energy Efficiency Design Index
IMO	International Maritime Organization
KVLCC2	Kriso Very Large Crude Carrier 2
LES	Large-Eddy Simulation
M.E	Modelling Error
NS	Navier-Stokes
PDE	Partial Differential Equation
PF	Potential Flow
R.E	Round-off Error
RANS	Reynolds-Averaged-Navier-Stokes
RPM	Rankine Panel Method
STAR	STAR-CCM+
T.E	Truncation Error
UN	United Nations
URANS	Unsteady-Reynolds-Averaged-Navier-Stokes
VOF	Volume Of Fluid

List of Symbols

α_{w_k}	Interpolation weights
$\boldsymbol{f}$	Body-acceleration
Δp	Difference in pressure
δ	Boundary Layer thickness
δ_{ij}	Kronecker delta function
ϵ	Turbulent dissipation rate

ϵ_W	Dimensionless wave-amplitude
$\eta_{3,4,5}$	Heave-,roll- and pitch-motion, respectively
$\frac{H}{\lambda}$	Wave-steepness
γ	Forcing coefficient
λ	Wave-length
μ	Dynamic viscosity of fluid
μ_T	Turbulent viscosity
∇	Differential Operator
ν	Kinematic viscosity
ν_T	Characteristic velocity scale of turbulence
ω	Wave-frequency in radians
$\overline{k}$	Kinetic energy of turbulence
$\overline{var}, \widehat{var}$	Mean and fluctuating part of a variable, respectively
ϕ	Current solution of the transport equation
ϕ_{D_k}	Function-value at point D_k
ϕ_{P_i}	Interpolated function-value at node P_i
ρ	Density of fluid
ρ^*	Value which the solution is forced towards
τ	Shear stress in the fluid
τ_{ij}	Viscous stress tensor
$\mathbf{V}$	Velocity vector in all three dimensions
$\tilde{v}$	Wall friction velocity
$\vec{\zeta}$	Vorticity
$\vec{i}, \vec{j}, \vec{k}$	Vector denotions in the x-,y- and z-direction, respectively
ξ	Local pressure gradient
ζ_A	Incident wave-amplitude
ζ_B	Free surface elevation at point B
C_F	Friction coefficient
C_T	Total resistance coefficient
c_W	Phase velocity of waves
$E\%D$	Relative error in %
f_1, f_2, n_d	Parameters of the wave-damping model
f_e	Encounter frequency in Hz
f_W	Initial wave-frequency in Hz
g	Gravity
L_A	Length from the origin to the inlet
L_F	Length from the origin to the outlet

p	Pressure
P_n	nth harmonic amplitude
R_P	Pressure resistance
R_T	Total resistance
R_V	Viscous Resistance
R_W	Wave Resistance
S_{ij}	Rate of mean strain tensor
T_e	Encounter period
u'	Velocity in x-direction with no pressure loss in the boundary layer
$u, v, worU, V, W$	Velocity component in x-,y- and z-direction respectively
u^+	Dimensionless velocity
U_e	Max velocity in the outer layer
u_I, v_I, w_I	Velocity components of the wave-orbit motion
x_{sd}, x_{ed}	Start- and end-point for wave damping length
y^+	Dimensionless distance from wall
y_n	Phase of nth harmonic amplitude
B	Length from the origin to the bottom-boundary
CFL	Courant-Friedrichs-Lewy number
Fn	Froude number
k	Wave-number
l	Characterstic length scale of turbulence
M	Mach Number
Rn	Reynolds number
S	Length from the origin to the side-boundary
T	Length from the origin to the top-boundary

Chapter 1

Introduction

1.1 Motivation

Since the dawn of man the sea been crucial for the survival of humanity. By offering an abundance of food and serving as a way of transportation when a relocation was necessary, it has always been an environment which we needed to master. To ensure a safe voyage or fishing trip, boats would have to be built as sturdy and stable as possible, and this required knowledge. Over the millenniums the evolution of the boat-building technique has enabled us to build larger and faster ships that could carry more load and traverse the waters more safely. Even though the ships of today do not resemble their more primitive ancestors, they are still built upon the same physical reasoning. However, in order to continue the technological advance of the ship-building industry, new ways of engineering are necessary.

Certain ship types, such as bulk-ships, have become subjected to a trend where the the ability to carry a larger load is more important than fuel-efficiency. As fuel-cost has historically been lower than crew and management cost, i.e fixed costs, with regards to the operation of cargo-vessels, ship design did not focus on the fuel-efficiency of the vessel, [Lindstad et al. 2013]. This resulted in full-bodied, almost prismatic, ships being built with the intention to carry as much as possible at the lowest expense. Nowadays, according to [Lindstad et al. 2013], fuel costs relate to 50% of the total costs, so the conventional hull shapes are not as economical as they were. In addition, the maritime society has become much more aware of the need to contribute to the reduction of environmental deteriorating gas-emissions. The Energy Efficiency Design Index was recently implemented, demanding a minimum energy efficiency for new vessels, [IMO 2017]. This minimum requirement will only become more and more strict, and a lot of the current ship-designs will not be operable in their current state. With this incentive, the need for more innovative and complex hulls may arise, and thus requiring more complex methods of calculation.

As potential flow (PF) theory has served the engineering community well over the years, and will continue to do so in the future, it neglects and simplifies certain physical aspects that may be important in some cases. While it does capture the general picture of the physical phenomenon it is describing, the information it omits is necessary to know before more advanced designs can be made.

Computational Fluid Dynamics (CFD) is not in itself a new field of engineering, as it has existed for a large portion of the latter stages of the 20th century. However, it has during the recent years, with the growing computational resources, gained more traction in the engineering community. Serving as a mean to further dive into the physical aspects of fluid dynamics, it achieves to represent the physical image with a much more detailed resolution. There exists different types of CFD - methods, namely Reynold's Averaged Navier-Stokes (RANS), Large-Eddy Simulations (LES) and Direct Numerical Solver (DNS), and all give a more descriptive physical picture than potential flow theory. Thus, with a better understanding of the physics occurring, ship design can be optimized

and improved for better sea-faring, less fuel-consumption and moreover a safer voyage for the passengers aboard.

The prevailing arguments against CFD have been that it is time-consuming and that it requires an educated and experienced individual to achieve accurate results, as the simulations require a substantial amount of tailoring to each individual problem. As computers nowadays become more and more powerful, the former argument is on the path of becoming obsolete, and with commercial softwares, such as Star-CCM+ (STAR) boasting an easy-to-use interface, the latter argument also seems to carry less and less weight as time progresses. However this is not to say that one would not need any pre-existing knowledge with CFD before using the softwares, but rather that the road to CFD-illumination would be significantly shorter.

Although CFD seems to be the prevailing method for an accurate description of fluid related problems, apart from the euphoric scenario where the Navier-Stokes equation is analytically solved, it is important to distinguish between problems that need a complex CFD-solver, and those that do not. Potential methods, such as panel-methods, are great for pressure-dominated systems, and they will always be much faster than any CFD-solver. As mentioned, DNS is the most accurate solver, with LES following and RANS methods being the least accurate of the three. While RANS needs considerably less computational resources than the other two aforementioned methods, it is still very time-consuming compared to potential-theory programs. An interesting compromise between CFD and portential flow theory, could be inviscid CFD.

Ship resistance and general seakeeping are most commonly perceived as pressure-dominated phenomenons. Thus a viscous CFD solver may require too much time compared to the potential gain in accuracy. Inviscid CFD neglects only the viscous terms in the Navier-Stokes equation, while potential theory assumes an irrotational, inviscid and incompressible flow-system. In addition, the inviscid simulations have the advantage that they can estimate higher order velocity and pressure terms, which the potential methods neglect. Therefore, inviscid CFD is a more accurate physical solver than potential theory, and may prove to be the ideal compromise between potential-theory analysis, and viscous CFD simulations.

1.2 Scope of Thesis

The purpose of this master thesis is to investigate the difference between inviscid CFD and viscous CFD, using the commercial software STAR-CCM+. The elements subjected to comparison are the pressure resistance, and motions of the KVLCC2 model ship, as presented in [Larsson, Stern, and Visonneau 2014].

The report will contain a literature study on the topic of added resistance in waves, and a theoretical explanation of the fluid dynamics involved in CFD. This will include a chapter on how the different tools in STAR works, and why they have been used for the simulations in this thesis.

The model is in a scale of 1:58, and calm water simulations will initially be performed and compared with similar experimental results from the Gothenburg workshop. The point of this is to verify that the numerical and physical, as well as the gridding of the domain are accurately calibrated and are able to capture the physics.

After this, the model will be subjected to incoming waves in head sea both to further test the accuracy of inviscid simulations. An important part of seakeeping tests in waves is the modelling of the incoming waves, and therefore this area of the simulations will be given some additional attention in the report.

The last condition will have the vessel subjected to oblique waves. The results from this will be followed by a discussion around the usefullness of inviscid CFD, with remarks on the result's validity for other ship types and a conclusion will be made regarding the applicability of the inviscid solver. Lastly, a section with suggestions for further work will be included.

Chapter 2

Ship Resistance

Ship resistance can be divided into many components, but they all have the same thing in common; they all express energy removed from the system. In this report it is the hull resistance that will be calculated and compared to experimental results, so all other resistance components will not be further discussed in this report.

The resistance a hull experiences as it propagates through the water can be divided into three components, [Molland et al. 2011a]:

1. Frictional Resistance

   Comes from the shear tangential forces acting on the hull surface

2. Pressure Resistance

   Arises from the forces acting normally on the hull surface

3. Total Viscous Resistance

   Pressure loss in the aft of the ship, the wake, results in a viscous drag force

The pressure force can be further divided into a viscous pressure component, and a wave component. This wave component comes from the waves the ship generates by its own when it traverses the water. Figure 2.1 gives a visual representation of the basic resistance components of a hull.

The following method of calculating the wave and viscous resistance, can be found in [Molland et al. 2011b], and is presented to give the reader an understanding of how the resistance components can be calculated. Consider a model held in a stream of velocity U, with no waves, and a control volume given as in figure 2.2. The wave-elevation generated by the hull can be calculated, and thus the energy removed from the system - wave resistance, can be estimated. The wave resistance can be estimated by equation 2.1, and the total viscous resistance by equation 2.2.

$$R_W = \frac{1}{2}\rho_w g \int_{-b/2}^{b/2} \zeta_B^2 dy + \frac{1}{2}\rho_w \int_{-b/2}^{b/2}\int_{-h}^{\zeta_B} (v_I^2 + w_I^2 - u_I^2) dz dy \tag{2.1}$$

$$R_V = \iint_{wake} [\Delta p + \frac{1}{2}\rho_w (u'^2 - u^2)] dz dy \tag{2.2}$$

Where:

R_W: Wave Resistance

R_V: Viscous Resistance

ρ: Density of fluid

g: Gravitational acceleration

ζ_B: Free surface elevation at position B in the control volume

u_I, v_I, w_I: Velocity components of the wave orbit motion in the x-, y- and z-direction, respectively

Δp: Loss of pressure in the boundary layer

u': Velocity in x-direction, if there was no pressure loss in the boundary layer

u: Actual velocity in x-direction

As can be seen from equation 2.1 and 2.2, information regarding the pressure- and velocity distribution is needed to calculate the forces. In the following section, the application of fluid mechanics, and CFD will be introduced to show how this can be done. Although, as long as there is structure above the free-surface, there will be a resistance component due to air. In the CFD-simulation this component will be present in the pressure and viscous shear terms, as the solver computes the resistance based on a eulerian multiphase mixture.

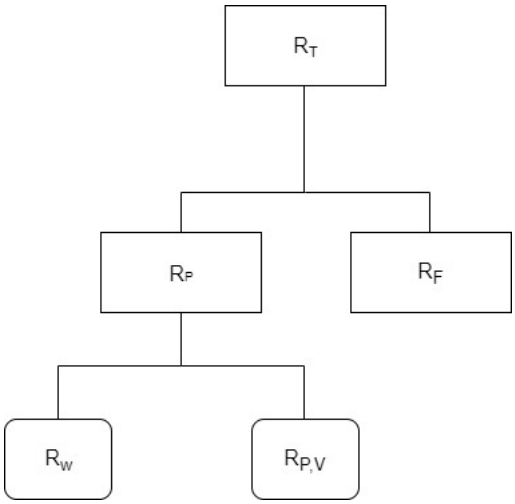

Figure 2.1: Resistance components for a hull in calm-water conditions

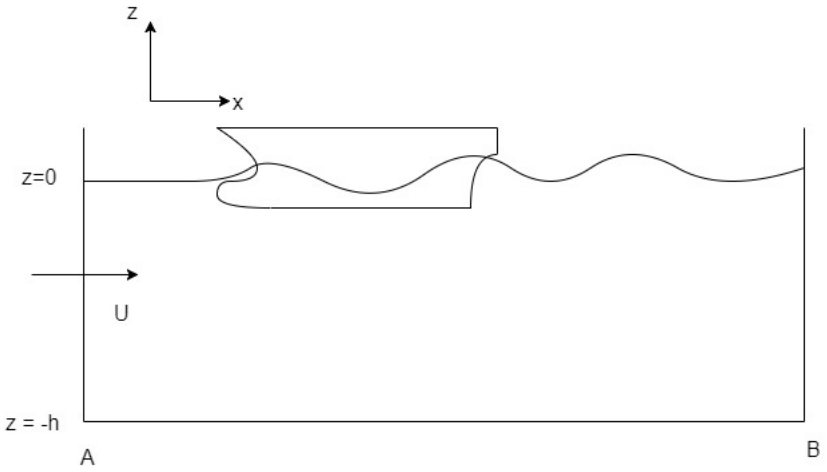

Figure 2.2: Control volume of model held in a stream of velocity U

Chapter 3

Added Resistance In Waves - A literature study

Throughout the years, ship design has heavily relied on hull optimization with regards to calm water resistance. Model testing and potential theory programs as well as empirical programs are all heavily used tools in the ship building community, and with good reason as they all predict the calm water resistance (with decreasing order of accuracy). While the information regarding the wave pattern the ship itself creates is useful, and calm water testing should be done, it is not these conditions operating ships most likely will encounter at sea. As waves will, in most conditions, be present it is also important to know about the added resistance in waves, and how the hull itself can be optimized with regards to this.

This section revolves around the basic theory surrounding added resistance in waves, and will give a literature review of the state-of-the art methods for predicting it. A discussion will ensue, in order to establish the most promising methods of calculating the added resistance.

3.1 Added Resistance - A Physical Understanding

As a ship traverses through the water, the system will be affected by two different wave-systems. The first is the wave pattern the ship makes as it pushes itself through the water, as discussed in section 2. The second is the incident wave that hits the ship, causing a radiated wave system to occur from induced ship motions and diffracted waves which are reflected from the ship itself. Both of these are mostly pressure related forces. While the calm water waves generated by the ship are a steady wave pattern, yielding a constant resistance, the incident waves will oscillate between decelerating and accelerating the system as the wave propagates along the ship. This, naturally, means that the incident wave imposes an oscillating force on the system, a force which varies greatly with wave-conditions, ship-geometry, and vessel heading. According to Arribas, [Arribas 2007], the added resistance can be divided into three components:

1. The diffracted waves when the wave hits the ship, and the radiated waves generated by the ship motions, called drifting force
2. Diffraction effect from the interaction between the diffracted and radiated waves
3. Viscous effects from damping of motions.

Intuitively one can surmise that the added resistance is mainly dependent on the following parameters:

- Wave amplitude
- Ship speed

- Wave length
- Wave heading
- Ship form

The dependence on wave length is naturally closely related to its relative size to the ship length. The aforementioned radiated and diffracted wave system each has their own area of significance with respect to the wavelength/vessel-length ratio, $\frac{\lambda}{L_{PP}}$. This can be viewed in figure 3.1.

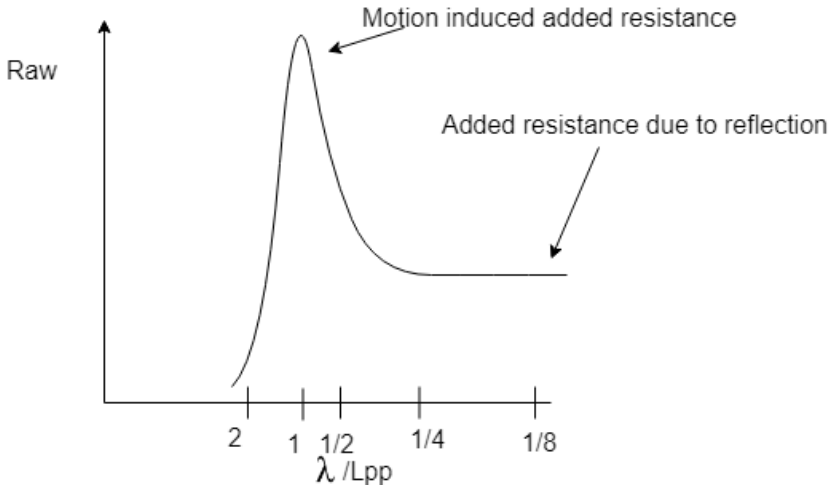

Figure 3.1: Added resistance dependency on wave length, adapted figure from [Boom et al. 2008]

From figure 3.1 it is natural to deduce that it is the drifting force which makes up the major part of the added resistance. According to [Arribas 2007], the added resistance is for all practical purposes a pressure related phenomenon. Due to this experimental test can be Froude scaled to accurately model the added resistance.

Experimental results have shown that the added resistance in waves is proportional to the square of the amplitudes of the incident wave, [Gerritsma and Beukelman 1971]. Due to this, it is extremely important to model the wave amplitudes correctly when doing seakeeping simulations with waves present.

As mentioned earlier, the viscous term of the added resistance is very small compared to the pressure related terms, and is as such often neglected. However this argument is often made on the basis of head sea conditions, which Arribas and many others, argue is the most severe condition. However, time may have proven this assumption wrong, as CFD-simulations have shown that oblique waves conditions of $10° - 20°$ yielded the highest added resistance, [Volker and Couser 2014]. Since oblique sea introduces other motions on the vessel such as yaw, roll, sway, the added resistance becomes a much more complex term to calculate. As such, other wave conditions than head waves may have a larger contribution from the viscous terms which goes unbeknownst in potential theory.

3.2 Added Resistance - Calculation Approaches

Over the years, several different approaches to estimate the added resistance in waves have been submitted. Including CFD the other ways of estimating the aforementioned resistance is through the use of experimental methods, empirical methods, or through potential flow theory.

3.2.1 Experimental Methods

Model tests have been the pinnacle of accurate resistance calculations for as long as its existence. As far as ship-resistance calculations go, they tend to be accurate, as the resistance field is pressure dominated. This means Froude scaling can be applied, without giving too much thought to the difference in the Reynold's number between the model and the full scale. However, while this is true for calm water and head waves, where it is the pitch and heave motions which are of importance, it may not be the case for oblique conditions. During oblique conditions viscous damping plays a larger roll on motions, and thus resistance, and the importance of a correctly scaled Reynold's number increases. However, on model scale they are very accurate, as they measure the actual physics occurring, and is as such the most accurate way of doing a seakeeping analysis.

3.2.2 Empirical Methods

Empirical methods have the advantage that they are easily implemented, and thus can be quite useful at an early stage in the design phase. They are mostly formulas based on regression mathematics applied to data gathered from experimental results. Due to this the methods have a tendency to lack a general applicability, and one should take care not to violate the conditions when using them.

Different formulas has been proposed over the years, and one of the earlier is the equation proposed by Kreitner [Kreitner 1939], equation 3.1 as given by [Volker and Couser 2014]:

$$R_{aw} = 0.64 g H_s^2 B^2 C_B \rho \frac{1}{L_{wl}} (\frac{2}{3} + \frac{1}{3} \cos \beta) \tag{3.1}$$

Where:

- H_s - Significant wave height
- B - Ship beam
- C_B - Block coefficient
- L_{wl} - Length at waterline
- β - Wave encounter angle

This formula was compared to CFD calculations by Volker and Couser, and showed deviations between 20-110%, [Volker and Couser 2014]. Later the method STAWAVE1 was proposed by STA-JIP, [Boom et al. 2008]. This formula is taking the area if which the incident wave hits when encountering the ship by the use of a parameter called bow length. This means the length from the tip of the bow to the position where the beam of the ship is at 95% of the full beam. The method is preliminary designed for short wavelengths, i.e, where the wave pattern is mostly caused by reflected waves and induced motions can be neglected. As a consequence of using the bow length as a parameter, the wave encounter angle was also limited to $\pm 45°$ off the bow,[ITTC 2014a].

Another estimation proposed by STA-JIP is STAWAVE2, [Boom et al. 2008]. This method is developed for added resistance calculations in both long and short waves. While Boom et al. concluded with the fact that both STAWAVE1 and STAWAVE2 showed great improvements compared to existing methods, at that time, they are still limited by their relatively narrow area of applicability. For STAWAVE2 the following limitations are, [ITTC 2014a]:

1. $75m < L_{PP} < 350m$
2. $4 < \frac{L_{PP}}{B} < 9$
3. $2.2 < \frac{B}{T} < 5.5$
4. $0.1 < Fn < 0.3$

5. $0.5 < C_B < 0.9$
6. Wave heading angle, $\pm 45°$ off the bow

A newer addition to the empirical calculation-methods is the semi-empirical method proposed by [S. Liu et al. 2016]. While claiming a mean absolute percentage error of $16,3\%$ the equation is only valid in head sea waves, [S. Liu et al. 2016]. It is important to mention that the purpose of the equation is to be used in early stages where only the main parameters of the ships is known, and only with limited computational tools at hand.

3.2.3 Numerical Methods

Potential flow theory and CFD are the two groups that makes up the numerical methods for computing the added resistance in waves. According to Newman the slender-body theory originated from the field of aerodynamics, with the pioneering work of Korvin Kroukovski to adapt this to ship motions, [Newman 1977]. Thus application of potential flow theory has existed since the mid 50s and the different methods of calculations are many. It is still present in the engineering society, albeit in a more advanced form, and is probably the most used theory in softwares specialized in marine hydrodynamics.

While the topic of turbulent, and viscous flow is not new to the scientific society, as witnessed by the ever perplexing Navier-Stokes equation, CFD was introduced when computers became a much used tool for engineering purposes. As computers became more powerful, their applicability to fluid flow problems grew. CFD-softwares using RANS and URANS solvers are becoming more and more able to handle fluid flow problems with high Reynolds numbers, [Steen 2014]. While its more complex siblings, LES and DNS, still has a long way to go before they can be applied in the industrial world, they are still the most accurate ways to model a viscous, turbulent flow.

Far Field

Maruo developed a formula to calculate the added resistance in waves, based on the velocity potential of the incident wave and the potentials stemming from the reflected and radiated waves caused by the body, [Maruo 1957]. With the basis in momentum conservation in an area enclosed by the surface S, Maruo assumed the energy flux through the body to be zero [O. M. Faltinsen 1990]. This formula was, according to [O. M. Faltinsen 1990], later generalized by Longuet Higgins to include finite water depths. [Gerritsma and Beukelman 1971] states that Joosen expanded Maruo's expression to included a larger domain of wave frequencies.

Gerritsma and Beukelman developed their own method of approximating added resistance in waves, by calculating the radiated energy from the body, using strip theory around the body.

Direct Pressure Integration

Direct pressure integration, or near field method, is meant for waves with small wavelengths, as it is calculated from the reflected wave system. It is approximated by looking at the problem as incident waves hitting a vertical wall, [O. M. Faltinsen 1990]. The equation by O. M. Faltinsen to calculate the drift-forces on a floating body, was later revised by [O. Faltinsen et al. 1980] to account for forward motion for all wave headings.

Strip Theory

Strip theory is a much used method for computing hydrodynamical forces and motions. It rests on the assumption that the body is slender, i.e, much longer than it is wide, and as such there is more flow variations in the cross-sectional plane than in the longitudinal. The wetted body is then

divided in to a finite number of 2D cross-sections where the forces and motions are computed, and then a summation of all the cross-sectional ensues to get the forces on the body as a whole, see figure 3.2, [O. M. Faltinsen 1990].

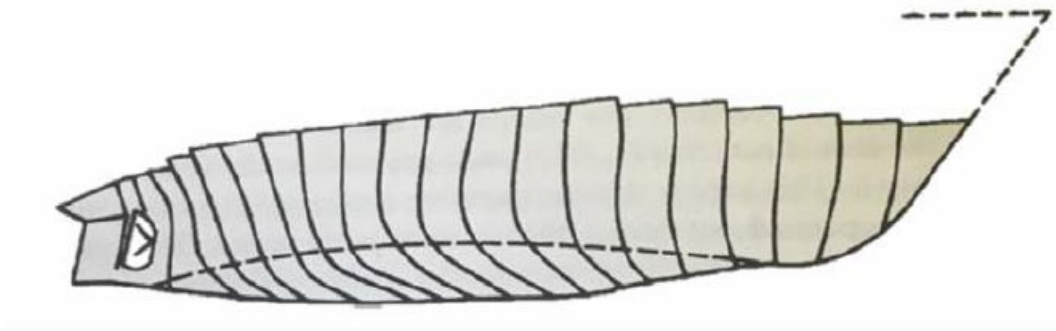

Figure 3.2: Strip theory approach dividing the ship into cross-sectional strips, [O. M. Faltinsen 1990]

A very much used variation of the strip theory method is the STF strip method proposed by [Salvesen et al. 1971]. According to Volker most of today's variations of strip methods are based upon this method, [Volker 2012]. A method revolving around high vessel speeds has been developed, and is appropriately called high-speed strip theory (HSST), [Volker 2012]. It is appropriate for $Fn > 0.4$, and it calculates the ship motions by the use of linear potential theory.

Subramanian and Beck developed a time-domain body-exact strip theory to predict the maneuvering of a vessel in calm and regular waves, [Subramanian and Beck 2015]. They claim to be able to capture the essence of the physical aspects of the phenomeon.

Panel Methods

Whereas the strip theory transforms 2D strips into 3D solutions, panel methods discretize the model in 3D using panels. A method of this is the Green's function method, where the Green's function represents the velocity potential due to a pulsating source at a singular point under the free surface. The method distributes panels on the mean wetted surface of the body. The Laplace equation, radiation condition and the free-surface condition are automatically fulfilled for the velocity potential on each panel, [Volker 2012]. Hong et al. claims to capture the trend of the Fn-dependent variations of added resistance in advancing waves, [Hong et al. 2016]. A 3D translating and pulsating (3DTP) source panel method has been used to solve the radiation/difraction problem. Wu et al. supports the use of Green's function for computing the second-order forces on a floating structure, claiming it to provide an efficient and sufficiently accurate option for this use, [Wu et al. 2017].

Another much used panel method, is the Rankine panel method (RPM). While both the free-surface in the near-field and the hull itself has to be discretized by panels it is, according to [Volker 2012], the best potential method to approximate the seakeeping problem. A type of discretized Rankine grid can be viewed in figure 3.3.

This method has been subjected to much research, as for instance by [Shao and O. Faltinsen 2010] when they proposed a body-fixed coordinate system for weakly-nonlinear problems to avoid the derivatives in the body-boundary-conditions. In addition, work done by [Sclavounos and Borgen 2004] on a high-speed vessel with hydrofoils, improved the RPM by including flow separation in the transom stern. Flow separation at the transom stern was according to Volker and Couser an area of inherent weakness for both the Green's function method, and RPM, [Volker and Couser 2014].

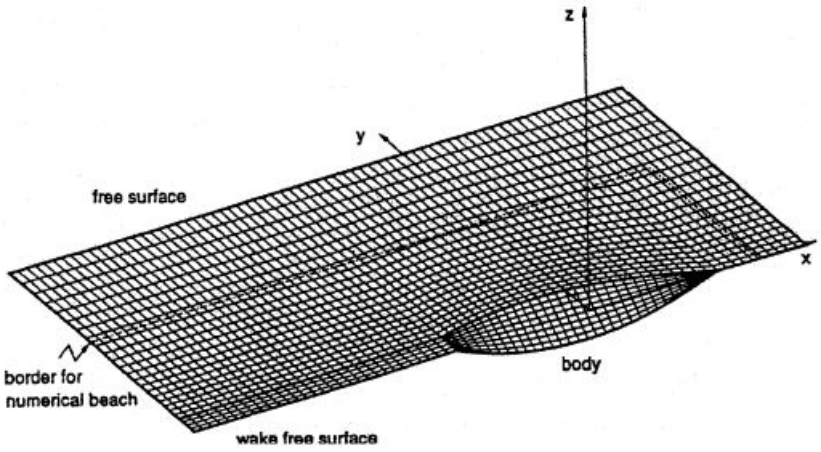

Figure 3.3: Discretized Rankine grid, [Sclavounos and Borgen 2004]

RANS Methods

Practical problem-solving with CFD regarding fluid flow became possible when computers became powerful enough to solve the different problems within a reasonable time-limit. A very popular CFD method is the RANS (Reynolds-Averaged-Navier-Stokes) which time-averages the turbulence over an area using semi-empirical turbulence models. A more detailed description of the theory behind the RANS method will follow in the next section. A lot of research and comparison with experimental results has been done with this method, for several different CFD solvers. As such its capabilities are well documented. Seakeeping isn't highly dependent on turbulent fluctuations, so the RANS method models all the relevant physics of the problem, [Volker and Couser 2014]. As CFD computes the velocity and pressure of every cell in the domain, it is easy to obtain the integrated pressure forces on the body. It is not, however as easy to model the free surface.

As mentioned, there is a lot of research revolving RANS methods, and one of the biggest contributors to this are the "Workshops on CFD in Ship Hydrodynamics", going back to as far as 1980 [Larsson, Stern, and Visonneau 2014]. The proceedings of the 2010 workshop are publicized, but the newer proceedings from the workshop in Tokyo, 2015, has yet to become available.

A lot of different cases were tried out during the 2010 workshop, and the accuracy between CFD results compared to EFD results varied from case to case, [Stern et al. 2014]. The seakeeping results compared the 0th and 1th harmonic amplitude, and the highest error for the 1th amplitude was 34% and 18% for the 0th amplitude of the resistance, [Stern et al. 2014].

Another seakeeping analysis was performed by Claus D. Simonsen et al., were the KCS model was subjected to both calm waters and regular head waves. Here, an Unsteady RANS (URANS) method was used, and for the error for the resistance's 0th amplitude varied between $2.3\% - 13.5\%$, [Claus D. Simonsen et al. 2013]. As can be seen, while the aforementioned results for seakeeping analysis are better than what both empirical and potential methods can achieve, their variation in accuracy is quite high.

Islam et al. compared a RANS CFD simulations with potential flow simulations, and concluded that RANS outperformed the potential code in regards to added resistance, [Islam et al. 2017]. However, motions in regular head waves were computed at a similar level of accuracy. This is most likely due to the fact that heave and pitch motion are mainly caused by radiated waves, and not viscous forces, [Volker and Couser 2014]. Thus, viscous modelling would for all practical purposes be redundant in regards to modelling heave and pitch motions.

3.3 Discussion

If the question is which type of method yields the most accurate results, the answer is the experimental method. As the CFD methods can have problems with short waves and with $Fn = 0$, among others, their general applicability is reduced, [Stern et al. 2014]. However, that is not to say they cannot achieve accurate results in these conditions, but rather that it may be difficult, and that the accuracy of a RANS solver is hard to generalize as it highly depends on the case at hand.

The accuracy of an empirical added-resistance equation is very dependent on the case. As stated above, its accuracy can differ from "passable as an initial estimate" to "complete nonsense". They can serve a useful purpose in giving a quick, initial estimate, but are not applicable when accuracy is demanded.

The literature regarding potential methods gave an image of a type of method that accurately captures the seakeeping characteristics. However, often the results were published with only a graphical comparison, and then a statement concluding that the potential method yields "fairly accurate" or "acceptable" results. This is a rather ominous sign, as a difference between the EFD and PF should be given as a relative error in percentage for it to be accurately evaluated. It is easy enough to make two lines look similar in a graph, simply by manipulating the graphs. Thus, it is hard to exactly specify the level of accuracy of a PF method, but as Islam et al. states, PF is not as accurate as RANS with regards to added resistance.

While both PF method and RANS method have their own advantages, and disadvantages, it could be possible to combine them. The combination of a system where the far field domain is solved by a PF solver and an inner domain solved by a CFD method is a concept that has been looked into. Malenica et al. looked into how such a coupling would interfere with the local fluid flow solution around the body. While they stated that this was possible, and had its advantages, it was not a method without problems. Some were related to the deduction of the velocity potential from the RANS solution, separation of the potential and non-potential parts of the RANS solution, consistency of the linearization and the accurate evaluation of the potential flow, [Malenica et al. 2017].

Another way to compromise between potential flow theory and RANS is to build a solver around the Euler equations. Here the non-viscous Navier-Stokes equation is solved on a CFD grid. The advantage of this is that there is no need to solve the boundary layer flow, and no turbulence models are required. In other words, there is a large potential gain in time-saving compared to RANS simulations. [Yang et al. 2015] used a Cartesian grid based Euler solver to compute the added resistance in head waves, and concluded that the solver managed to capture the physics with good accuracy. A comparison of the Euler method with strip theory and the RPM was done on a number of different ship models, and the added resistance in head waves were reported to be of similar accuracy, [Seo et al. 2013]. Again, without a numerical difference given for the different methods, it is hard to evaluate what "similar accuracy" means. While both pitch and heave can be modelled by potential methods with great success, the added resistance is another subject. As [Volker and Couser 2014] states, it is in oblique sea that much more complex physics arise, and simplified methods such as potential theory won't cut it.

From this literature study it has become apparent that, apart from experimental methods, RANS or similar viscous CFD methods are the most accurate ways to capture the seakeeping problem, although, it is very time demanding. In time this disadvantage will fade away as computers will undoubtedly increase in computational capacity. However, if it is possible to save time by using simplified methods, that still captures the physics of the flow problem, this should be done. As there is a lot of proof that the Euler solver is good enough in head waves, this thesis will check if the same can be said for oblique waves.

Chapter 4

Computational Fluid Dynamics - CFD

CFD is based upon the fundamental equations of fluid dynamics. According to [Ransau 2003a], they give a mathematical description of Newtonian flows, often referred to as the Navier-Stokes (NS) equation. This equation is based on the following three principles:

- Mass is conserved
- Momentum is conserved
- Energy is conserved

When these principles are applied to a fluid flow problem, it gives rise to the aforementioned Navier-Stokes equation, as given in [Pletcher et al. 2013a]:

$$\rho\frac{D\mathbf{V}}{Dt} = \rho\mathbf{f} - \boldsymbol{\nabla}p + \frac{\partial}{\partial x_j}[\mu(\frac{\partial u_i}{\partial x_j} + \frac{\partial u_j}{\partial x_i}) - \frac{2}{3}\delta_{ij}\mu\frac{\partial u_k}{\partial x_k}] \tag{4.1}$$

Where:

$\frac{D\mathbf{V}}{Dt}$ - Acceleration of fluid

$\mathbf{f}$ - Body-acceleration, in many cases gravity, g

∇p - Differentiated pressure

μ - Dynamic viscosity of fluid

$\frac{\partial u_i}{\partial x_j}$ - Partial derivation of velocity in i-direction with respect to j-dimension

δ_{ij} - Kronecker delta function

Equation 4.1 describes an incrompressible, Newtonian fluid flow problem. As this report will focus on ship resistance, the two fluid flows modelled is water and air. Water is by all practical means incompressible, and as given in [Pletcher et al. 2013b], air can be assumed to be incompressible, for fluid velocities below 100 m/s, or $M < 0.3$, where M is the Mach-number.

Equation 4.1 describes the entire fluid flow problem in the three dimensions. Although it is only one, albeit complex, equation it has perplexed researchers and scholars since its creation. As of yet there exists no direct, analytical solution, however there has been successful adaptations, with numerical methods, and physical reasoned simplifications. In this report a RANS solver was used to obtain the results. While a DNS solver, or even a LES solver could be used with potentially greater success, the computational time would become too large to be practical for the scope of this report.

The Euler equation that is solved in the inviscid simulation of this thesis, is identical to equation 4.1, apart from the viscous term, i.e last term on the right-and side of the equation. As the pressure and velocity is calculated in the same way for Euler and NS, apart from the viscous term, the Euler method is not given any more heed in this section.

4.1 RANS - Renyolds Averaged Navier-Stokes

One of the simplifications to solve the Navier-Stokes equation, is to assume a time averaging of the equation, which has become known as Reynolds Averaged Navier-Stokes, or the Reynolds equation. Here, the quantities are split into mean components and fluctuating components:

$$u = \bar{u} + \hat{u}; \quad v = \bar{v} + \hat{v}; \quad w = \bar{w} + \hat{w}; \quad \rho = \bar{\rho} + \hat{\rho} \quad p = \bar{p} + \hat{p} \tag{4.2}$$

Where:

$\overline{var}$: Mean value of variables

$\widehat{var}$: Fluctuating part of variables

By definition, the mean of a fluctuating component is zero, but the mean of the product of two fluctuating components is, in general, not zero. Thus, by introducing these mean and fluctuating components in equation 4.1 and averaging the whole equation, we get for an incrompressible fluid, as given in [Pletcher et al. 2013c]:

$$\frac{\partial}{\partial t}(\rho\overline{u_i}) + \frac{\partial}{\partial x_j}(\rho\overline{u_i u_j}) = -\frac{\partial \overline{p}}{\partial x_i} + \frac{\partial}{\partial x_j}(\overline{\tau_{ij}} - \rho\overline{\hat{u_i}\hat{u_j}}) \tag{4.3}$$

Where

τ_{ij}: Viscous stress tensor, given as:

$$\overline{\tau_{ij}} = \mu(\frac{\partial \overline{u_i}}{\partial x_j} + \frac{\partial \overline{u_j}}{\partial x_i}) \tag{4.4}$$

This introduces a new component to the Navier-Stokes equation, namely, the Reynold stress tensor,$\overline{\hat{u_i}\hat{u_j}}$.

From this point of view it is hard to see why this helps modelling the NS equation. This stress tensor only introduces new unknowns to the equation, thus requiring additional equations to "close" the system of equations. However, these new unknowns have more transparent solutions, simplifying the NS equation. This is done by turbulence modelling.

4.2 Turbulence Modelling

The Bousinesq equation, relating the turbulent shear stress to the rate of mean strain through eddy viscosity, can be shown as for the general Reynolds stress tensor as, [Pletcher et al. 2013d]:

$$-\rho\overline{\hat{u_i}\hat{u_j}} = 2\mu_T S_{ij} - \frac{2}{3}\delta_{ij}(\mu_T \frac{\partial u_k}{\partial x_k} + \rho\overline{k}) \tag{4.5}$$

Where:

μ_T: Turbulent viscosity

S_{ij}: Rate of mean strain tensor

$\overline{k}$: Kinetic energy of turbulence

Further the turbulent viscosity, μ_T, can be expressed as:

$$\mu_T = \rho \nu_T l \tag{4.6}$$

Where:

ν_T: Characteristic velocity scale of turbulence

l: Characteristic length scale of turbulence

In order to establish an accurate model the turbulent viscosity, appropriate measures needs to be taken to model ν_T and l. There exists two different categories of turbulence models whose purpose is to close the Reynolds equations, [Pletcher et al. 2013d]:

- Category 1:
  Models using the Boussinesq assumption, also known as turbulent viscosity models
- Category 2:
  Models enabling closure of the Reynolds equation without the use of the Boussinesq assumption

There also exists a category 3, where the models are not entirely based on the Reynolds equations, such as the LES-methods. In this report, the turbulence model of choice is the k-ϵ model, which is a category 1 turbulence model, which will be discussed further. Consequently, category 2 and 3 models will not be subjected to further discussion. The choice of turbulence model and the reason behind it, will be further discussed in the section covering the numerical set-up.

4.3 Boundary Layer Theory

The concept of a boundary layer was first deduced by Ludwig Prandtl, [Pletcher et al. 2013e]. He argued, from experimental studies that for high Reynolds numbers, there existed a thin film of fluid very close to the surface of an object, where viscous effects were at least as important as inertia effects. This region's thickness, δ, was assumed to be of a length much smaller than the streamwise length of the object itself, $\frac{\delta}{L} << 1$. According to [Cengel and Cimbala 2010a], the boundary layer is defined as the thickness of the region measured from the surface of the object, to the point where the velocity component of the parallel flow reaches 99% of the fluid speed outside the boundary layer.

Consider a smooth, circular surface submerged in infinite fluid, in a 2D flow, with a uniform flow, U, going in the x-direction, as depicted in figure 4.1. The shear stress in the fluid can be, according to [Pettersen 2007], expressed as:

$$\tau = \rho \nu \frac{du}{dy} = \mu \frac{du}{dy} \tag{4.7}$$

Where:

ν: Kinematic viscosity

As can be seen from figure 4.1, the flow close to the surface will change drastically as it follows the surface of the body. When the flow initially hits the surface, at the stagnation point, the velocity will go towards zero, as it cannot penetrate the surface. This implies an increase in pressure, following the Bernoulli equation for a steady, incrompressible flow, equation 4.8. The flow will gain velocity and lose pressure as it follows the surface, and it will go through different stages, as depicted in figure 4.1:

- Stage A
  The build up of a boundary layer, as it is zero at the surface, due to the no-slip condition, and reaches eventually the speed of the surrounding flow.

- Stage B
  The boundary layer is fully developed, with its max velocity
- Stage C
  The fluid close to the surface loses velocity as it is affected by the nearby no-slip area.
- Stage D
  Separation point. As given by equation 4.7, the term $\frac{du}{dy}$ becomes negative due to the shear forces in the fluid. This results into a reversed fluid flow, causing the creation of vorticity, as given by equation 4.9, which leads to vortex shedding.

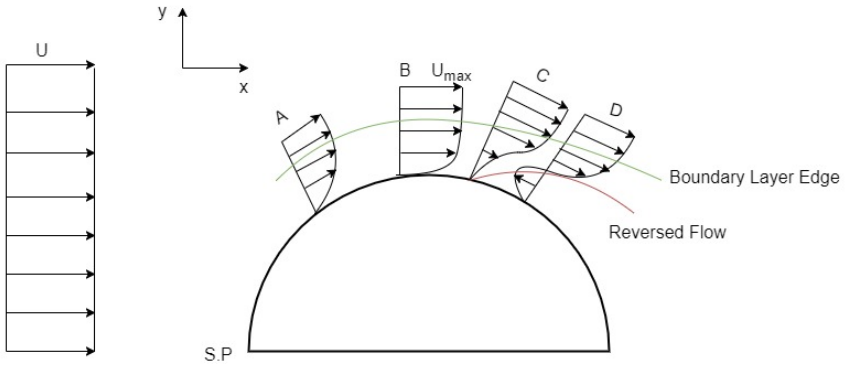

Figure 4.1: Depiction of the boundary layer around a circular 2D cylinder in uniform flow

The Bernoulli equation for a steady, incompressible flow as given by [Cengel and Cimbala 2010b]:

$$p + \rho\frac{U^2}{2} + \rho g z = constant \tag{4.8}$$

The vorticity in a 2D flow, in the x-y plane, can according to [Cengel and Cimbala 2010c], be expressed as:

$$\vec{\zeta} = (\frac{\partial v}{\partial x} - \frac{\partial u}{\partial y})\vec{k} \tag{4.9}$$

The vorticity in a flow is directly linked to the vortex shedding behind the object, and is therefore an important parameter when it comes to pressure estimations. Having a too coarse mesh in the boundary layer, will then inaccurately model the boundary layer, leading to faulty vorticity. This will in turn yield an inaccurate wake which will produce a wrong estimate for the resistance and motions.

4.3.1 Turbulent Velocity Profile

Taking into account that half of the simulations in this report revolves around a turbulent flow, it is important to know how to model the turbulent velocity profile close to the surface. According to [Cengel and Cimbala 2010d], the turbulent velocity profile can be divided into four regions:

- Viscous Sublayer
  A very thin layer, that is closest to the surface. Here the velocity profile is almost linear and the flow is streamlined.
- Buffer Layer
  Turbulent effects are becoming increasingly significant, but the viscous dominates.
- Overlap Layer/Inertial Sublayer
  Larger influence of the turbulent effects, but they are still not dominant

- Outer Layer/Turbulent Layer
  The turbulent effects here dominates over the viscous effects

To achieve a good representation of boundary layer, and thus the turbulent velocity profile, the challenge is to find a way to model this correctly. According to [White 2006], the velocity profile in the viscous sublayer, and the velocity profile in the outer layer can be expressed by equation 4.10 and 4.11, respectively:

$$\frac{\overline{u}}{\tilde{v}} = f(\frac{y\tilde{v}}{\nu}) \tag{4.10}$$

$$\frac{U_e - \overline{u}}{\tilde{v}} = g(\frac{y}{\delta}, \xi) \tag{4.11}$$

Where:

$\tilde{v} = (\frac{\tau}{\rho})^{\frac{1}{2}}$ is called the wall friction velocity

U_e: Max velocity in the outer layer

ξ: Local pressure gradient

In order to find a suitable description of the buffer layer, the expressions for the viscous and outer layer are equated, resulting in the following expression, called law of the wall:

$$f(\frac{\delta\tilde{v}}{\nu}\frac{y}{\delta}) = \frac{U_e}{\tilde{v}} - g(\frac{y}{\delta}) \tag{4.12}$$

For equation 4.12 to be true, the functions f and g has to be logarithmic functions, [White 2006]. Defining the non-dimensionalized distance and velocity as:

$$y^+ = \frac{y\tilde{v}}{\nu}; \quad u^+ = \frac{U_e - \overline{u}}{\tilde{v}} \tag{4.13}$$

We see that the law of the wall equation simplifies to:

$$y^+ = u^+ \tag{4.14}$$

According to [White 2006] the velocity profile is modelled accurately when the y^+ values lies in the following region; $35 \leq y^+ \leq 350$. However for smaller values of y^+, thus in the buffer and viscous layer, the law-of-the-wall estimates the profile inaccurately as it assumes a logarithmic profile, while it is closer to linear. However, this brings an eventual solution a lot closer to what is physical, and the law-of-the-wall is being implemented in the CFD-industry through so-called wall functions, as it is applicable to almost all wall-bounded turbulent boundary layers, [Cengel and Cimbala 2010e]. The regions of the velocity profile can be seen in figure 4.2. An estimate of y^+ can be obtained, by using the following equations, given by [O. M. Faltinsen 2005], and equation 4.10 and 4.13:

$$C_F = \frac{0.066}{(\log(Rn) - 2.03)^2} \tag{4.15}$$

$$C_F = \frac{\tau}{0.5\rho U^2} \tag{4.16}$$

Where:

C_F: Friction coefficient

Rn: Reynolds number

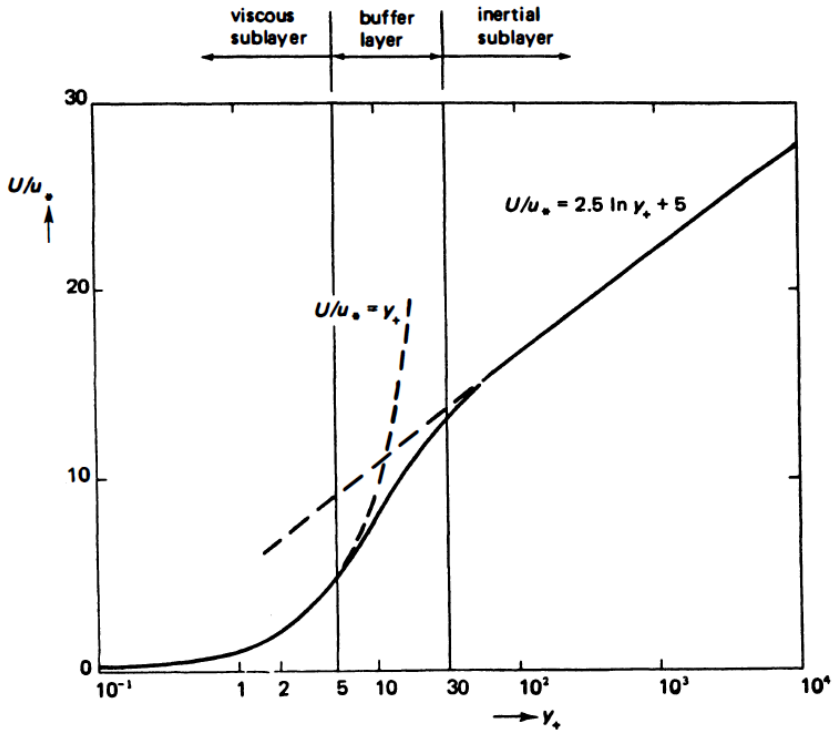

Figure 4.2: Turbulent velocity layer, as given by [Tennekes and Lumley 1972]

To get an estimate of the boundary layer thickness, equation 4.17 as proposed by [O. M. Faltinsen 2005] can be used:

$$\delta = \frac{0.16x}{(Rn_x)^{\frac{1}{7}}} \tag{4.17}$$

Where:

x: Position of calculation along the streamwise length on the surface of the object

4.4 Errors Associated With CFD

CFD has many applications, and can be used to solve a large variety of different cases. Regardless of how different the CFD problem at hand is, be it combustion of gases in a piston, or the motions a spar-buoy experiences when subjected to irregular waves, they all need to go through the same "recipe". These steps of solving an engineering problem with CFD could be, according to [Ransau 2003b], arranged as depicted in figure 4.3.

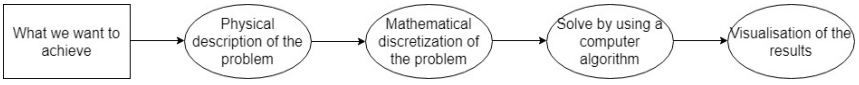

Figure 4.3: Steps of gaining a solution with CFD

In other words, the physical problem in the real world will be, after thoroughly understood, transformed into the mathematical world. By simple reasoning, one could perceive the problems in mapping every random parameter occurring in the real world mathematically. Even if the real world transformation was a success, it still needs to be subjected to a computer algorithm solving the mathematical world. Thus there are two transformations in order to solve what is happening

in the real world, and naturally there will be errors related to this. Figure 4.4 shows the general mapping of a physical problem, and the errors associated with each step.

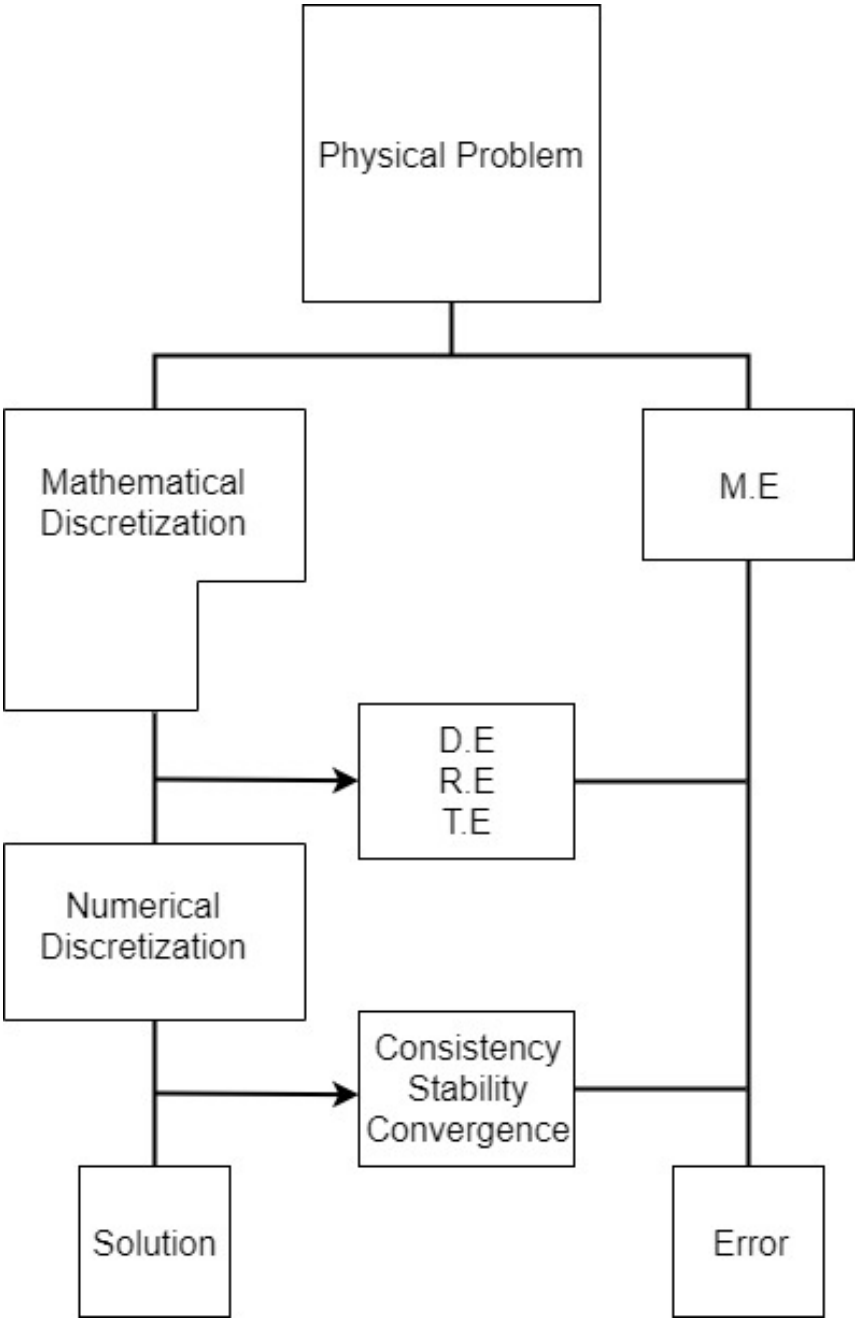

Figure 4.4: Errors associated with CFD

Where:

M.E: Modelling Error

D.E: Discretization Error

R.E: Round-off Error

T.E: Truncation Error

Modelling Error

Modelling the real world with mathematical expressions implies using formulas that describes the physical phenomena accurately. Although there exists complex mathematics that can describe most physical phenomena occurring in the world, there will always exists a level of randomness with each unique case, which these formulas are not able to capture. The modelling error will then become the sum of the short-comings of the mathematical formulas, and the errors associated with random, non-quantifiable, parameters.

Discretization Error

Regarding the transformation from the analytic world, to the numerical one, the discretization error will stem from the simplifications that numerics introduces. As many of the formulas introduced by the mathematical modelling cannot, as of yet, be solved analytically, they are solved numerically. Due to this, the error associated with dividing the area of calculation into discrete sums of which you solve the equations, will be present.

Round-off Error

This error is associated with the precision of each calculation. While rounding up a number from 1.0089 to 1.009 in a series of 20 calculations might not make much of a difference, but when the number of iterations become significantly larger, each round-off will contribute, and eventually a significant error might be present.

Truncation Error

In order to solve the mathematical problem, a CFD code will divide the control volume into discrete points of which it solves the equations. As with a partial derivative, the code calculates this by means of finite differences. The difference between the partial differential equation, PDE, and the finite difference equation, FDE, representation is called the truncation error, T.E, [Pletcher et al. 2013f]. The finite difference is dependent on how fine the gridding, $\Delta x, \Delta y, \Delta z$, and the timestep, Δt is. And, according to [Pletcher et al. 2013f], $T.E \longrightarrow 0$ as $\Delta t, \Delta x, \Delta y, \Delta z \longrightarrow 0$.

Consistency

According to [Pletcher et al. 2013f], a finite difference scheme is said to be consistent, if the T.E goes to zero as the mesh is refined. A scheme is said to be consistent if it yields the same result when the simulation is run multiple times.

Stability

For a code to be stable, it is required that the errors from the code do not increase from one timestep to the next. A well-known condition for stability is the Courant-Friedrichs-Lewy number, defined by [Pletcher et al. 2013f] as:

$$CFL = \frac{u\Delta t}{\Delta x} \quad , \frac{v\Delta t}{\Delta y}, \quad \frac{w\Delta t}{\Delta z} \leq 1 \tag{4.18}$$

Equation 4.18 says that in order to have stability, the flow cannot travel further than one cell-length during one time-step. However, according to [CD-Adapco 2018], using an implicit unsteady scheme, the CFL-number can rise high above 1 and still yield accurate results. This may be a subject up for debate, regarding its universal validity, rather than more case-dependent, as [Böhm

and Graf 2014] concluded that for free-surface simulations, a $CFL \geq 0.5$ could yield numerical inaccuracies.

Convergence

According to [Pletcher et al. 2013f], a stable scheme is also convergent as given by the Lax's equivalence theorem: "Given a properly posed initial value problem and a finite difference approximation to it that satisfies the consistency condition, stability is the necessary and sufficient condition for convergence".

Chapter 5

Model Description

A central part of this thesis is the comparison between viscous and inviscid CFD not only in head sea waves, but also in oblique sea. As there is far less literature regarding seakeeping in oblique sea, it was important to ensure that the numerical set-up is validated in head sea. This way, with validated head-sea waves, the argument that the oblique sea simulations are also valid would carry much more weight. As there exists a lot of experimental and numerical results on the KVLCC2 vessel, it was chosen as the subject for simulation.

The KVLCC2, or Kriso Very Large Crude Carrier 2, was according to [Larsson, Stern, and Visonneau 2014] designed at the Korea Research Institute for Ships and Ocean Engineering in 1997. Its sole purpose is to be used as a test case for CFD simulations, and therefore there has been done a lot of experimental tests on it. A visual of the vessel can be viewed in figure 5.1 and full scale and model scale data is shown in table 5.1.

As can be seen in figure 5.1 the non-purple part of the figure is an additional part not originally included in the CAD-file from [Larsson, Stern, and Visonneau 2014]. The reason for this is that in certain instances it is impossible to avoid water on deck with the original CAD file. This was deemed much more harmful to the results than what an increased area above the free-surface would be, [Guo et al. 2012]. Therefore the lines from the CAD file has been linearly extrapolated to increase the height above the free-board. The CAD file was extracted from the work of [Rørvik 2016], which is the same file as the one from [Stern et al. 2014], except that it also includes the extrapolated part.

Table 5.1: Main characteristics of the KVLCC2

Symbol	Unit	Ship	Model
Scale	[-]	1	58
L_{PP}	[m]	320	5.5172
B	[m]	58	1
T	[m]	20.8	0.3586
D	[m]	30	0.5172
C_W	[-]	0.9077	0.9077
C_B	[-]	0.8098	0.8098
Displacement	$[m^3]$	312,622	1,6023

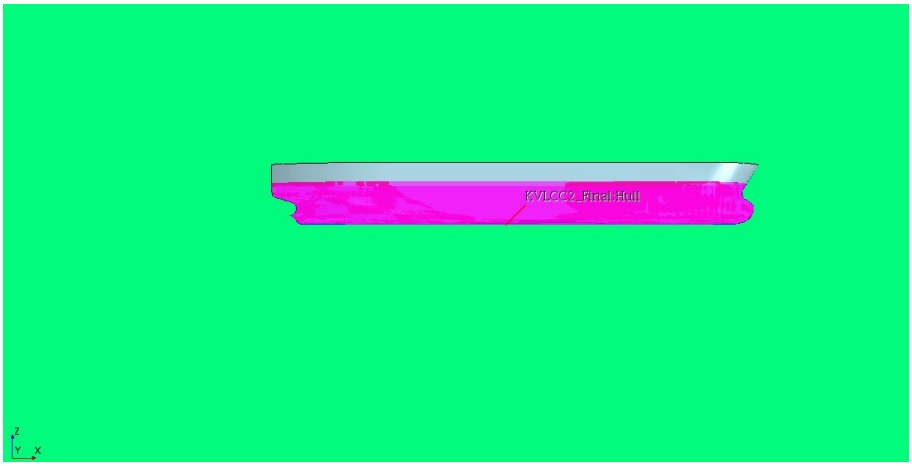

Figure 5.1: Geometrical representation of the KVLCC2 hull

Chapter 6

Computational Method

As of today there exists a lot of different softwares that solve physical problems with CFD. Among these there are the well known ANSYS FLUENT, OpenFOAM, and of course the program used in this report; STAR-CCM+ (STAR). With these programs there also are a lot of solvers, each designed to accurately solve a certain type of problem. The same can be said for boundary conditions, and a lot of other parameters involved in generating an accurate and stable simulation. While the previous section might illuminate the theory behind CFD, it does not show it in practise. This section will go through the main steps behind the set-up for the simulations. There are some differences between the set-ups for the different seakeeping conditions, so in this section all the models used in the simulations will be introduced. Then in the result section the choice of model for each simulation will be discussed.

To do a CFD simulation in STAR the following steps needs to be addressed:

- Geometry import
- Region and boundary condition specification
- Generate a suitable mesh
- Proper physical model has to be chosen, with initial conditions
- Establishing a correct solver
- Defining stopping criteria
- Creating monitors and plots to retrieve significant information
- Visualizing the obtained results

6.1 STAR-CCM+

STAR is a Computer Aided Engineering (CAE) program for solving multidisciplinary problems, developed by CD-Adapco. It has a lot of integrated platforms, making it possible to go from conceptual design in its CAD platform to full visualization of the simulation in the same interface.

It is based on the finite volume method, with a lot of different options for solving physical problems. STAR includes a lot of options when it comes to CFD analysis, a lot more than is covered in this section, and is in the right hands a very powerful engineering tool.

6.2 Defining Regions And Boundary Conditions

While calm water, head waves and oblique waves requires different set-up, they share some common denominators. A towing tank was modelled for the background region for all the simulations. However, the tank does not have the same dimensions for the different conditions, and for the wave-simulations an overset mesh has been implemented. The reasons for these changes will be further discussed in the result section.

Figure 6.1 shows a visual representation of the regional discretization. For the calm water simulation, the overset interface is not present.

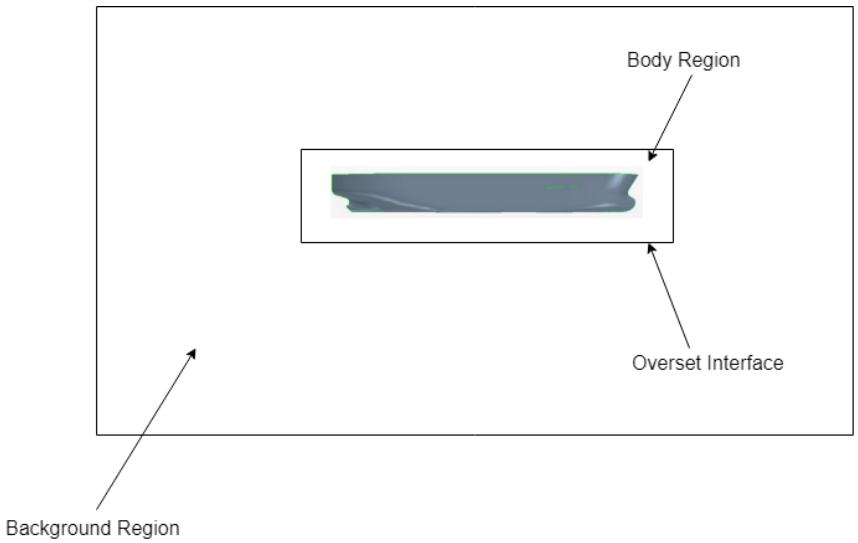

Figure 6.1: Regional discretization

6.2.1 Boundary Conditions

Different types of boundary conditions is demanded for the different simulations present in this thesis, and the different choices will be clarified in their own sections revolving around the specific simulations. While the names of the boundary conditions and their main function might be similar to other software's boundary conditions it would be naive to think they are identical. Therefore the rest of the section will be an overview of the aforementioned boundary conditions as they are described in [CD-Adapco 2018].

Velocity Inlet

This is a Dirichlet boundary condition, in other words, it allows the user to specify the value in which the inflow is supposed to take. According to [CD-Adapco 2018], the pressure is extrapolated from the adjacent cells using reconstruction gradients. As the simulations either involve a calm water towing experiment, or a ship with forward motions having incoming waves from different headings, this is a natural boundary to use at the inlet face.

In addition, the boundary calculates the flux of the fluid flow, enabling a positive flux to be an outlet and a negative flux as an inlet. This way, it is a useful boundary to use at other boundaries, apart from the outlet. It is also advised by [CD-Adapco 2018] to use the inlet boundary condition whenever possible when a VOF-wave model is enabled.

Pressure Outlet

For subsonic flows, which this is, the outlet pressure is specified directly. This, too, being a Dirichlet boundary condition, the outlet pressure is specified to be the hydrostatic pressure of the initial wave-condition. Since the VOF wave is a multiphase wave, including both air and water, it accurately determines the outlet pressure, if the VOF solution is able to accurately model the two different phases. In addition, to inhibit wave reflection either VOF Wave Damping Boundary option or the Wave Forcing option can be used at this boundary.

Wall Boundary Condition

The wall boundary condition models an impermeable wall which fluid flow is either confined in, or kept from penetrating. It prevents any flux through the boundary, and only allows flow to move tangentially with the surface of the boundary. Wall-boundaries can either have a slip-wall or a non-slip wall condition, where the slip-wall lets the fluid that is in the slip-region move with the velocity of the wall boundary without any shear-stress occurring. Conversely the no-slip condition will enable the shear-stresses. Naturally this boundary condition is specified for the ship model with the no-slip condition, as flow through the hull is not physical, and the shear stress at the surface is needed for resistance calculations.

Symmetry Plane

Sometimes, while inhibiting a flux through a surface is desirable, but not parallel at the surface, a symmetry plane condition may be applied instead of a wall condition. Here the flow is mirrored around the boundary, effectively inhibiting any flow from leaving the domain. This is equivalently of having the mesh mirrored around that symmetry plane. Therefore, in simulations having a symmetry plane this is a prerequisite as it halves the computational domain.

Overset Mesh

When an overset mesh method is implemented the inner domain, as shown in figure 6.1, needs its own boundary conditions, to successfully communicate with the outer domain. The overset mesh boundary condition is chosen at all the faces which is in the inner domain. An exception is the boundary that lies in the outer domain's symmetry plane. Here, the symmetry boundary condition is applied. This is due to that an overset mesh analysis demands that any faces between the background domain and the overset domain that are parallel, share the same type of boundary condition. This will be further explained in its own section.

6.3 Physics Continuum

Using STAR there exists several different physics that can be modelled. These falls into the following categories, as given by [CD-Adapco 2018]:

- Fluid Mechanics (Multiphase Flow options)
- Materials
- Heat Transfer
- Motion
- Reacting Flows
- Electrochemistry

- Plasma
- Electromagnetism
- Aeronautics
- Computational Rheology

Considering that the simulations are seakeeping analysis, the physic models chosen for the simulation involves both motions and fluid mechanics. The models chosen for the viscous and inviscid simulations can be seen in table 6.1 and 6.2, respectively.

Table 6.1: Chosen physics models, viscous simulation

Field of Physics	Model
Space	Three-Dimensional
Time	Implicit Unsteady
Fluid Mechanics	Eulerian Multiphase
	RANS
	VOF
	Segregated Flow
	Realizible k-ϵ Two-Layer
	Two-layer Y+ Wall Treatment
Other Models	Gravity
	VOF Waves

Table 6.2: Chosen physics models, inviscid simulation

Field of Physics	Model
Space	Three-Dimensional
Time	Implicit Unsteady
Fluid Mechanics	Eulerian Multiphase
	Inviscid
	VOF
	Segregated Flow
Other Models	Gravity
	VOF Waves

Modelling Time

For time-modelling there are two main choices one can choose between: explicit or implicit methods. Explicit methods has the advantage that they compute the values for each time-step by using the values from the previous time-step. Therefore no additional system of equations is needed to obtain the values at the present time-step. This makes the explicit method fast, but it also falls prey to strict stability requirements, like the CFL-requirement mentioned previously. Therefore with simulations with transient phases, where flow velocities become temporarily large, the explicit method will fail.

The other time-modelling choice is the implicit method. Here the values are computed for the new time-step by using values at the same time-step. This requires a system of equations to obtain the values, due to the increased number of unknowns. This makes the implicit method slower than the explicit, but it is also unconditionally stable. Therefore it can violate the CFL-condition without crashing. This in turn allows for a coarser time-step and thus a more time-efficient simulation. There are limitations for the time-step for implicit schemes involving free-surface simulations, and

wave-simulations, and the choice of time-implicit scheme will be shown and argued for in each of the separate simulation-sections.

The two different time-discretization schemes used for the simulations in this thesis, are the first-order and second-order implicit time discretization. The difference is that the second order time scheme approximates the transient term on the new time-step with the values at that time step, along with the two previous time-steps. The first order scheme only uses the new time-step along with the previous time-step. For rigid body motion, the second order time-scheme also uses a second order grid flux equation as opposed to the first order grid flux equation found for the first-order time scheme. This makes the second-order time scheme more accurate when there are a lot of changes in the flow with respect to time, but it also makes it more sensitive to the CFL condition.

Spatial Discretization

The convection of the variables is very important to model accurately. In STAR there are several convection schemes connected to the Segregated Flow solver; 1st and 2nd order upwind schemes and 3rd order MUSCL, [CD-Adapco 2018]. STAR suggests a 2nd order upwind scheme for convection, as it will give as good or better, albeit slower, than the 1st order method. Therefore the 2nd order method is chosen for all convection schemes in the simulations.

Volume Of Fluid - VOF

According to [CD-Adapco 2018], the VOF-method works very well for a multiphase case were the area of mixture is small relative to the domain, and it is all concentrated in the same area. This is why it is very suitable for modelling the free surface.

As given by [Ransau 2003c], the method introduces a function that takes the value 1 if the cell is only occupied by the fluid and zero if no fluid is present. The value of the function will therefore find itself between $0 \leq \phi \leq 1$, and a high resolution mapping of the mixture area will then give the free-surface.

In a free-surface simulation, the water and air particles will be separated in the cell by a sharp interface. Standard higher-order schemes such as second-order upwind and central differencing would fail in capturing this sharp interface, [CD-Adapco 2018]. Therefore, the VOF method in STAR makes use of the High-Resolution Interface Capturing (HRIC) method to model the free-surface more accurately. According to [Rhee et al. 2005], the HRIC method is a blend between downwind and upwind method such that a cell does not get overflown or underflown by the computed fluxes from the volume fraction. The blending of the two discretizations is determined by the local Courant number, the relative position of the free-surface to the cell were the flux is computed and the local volume fraction distribution, [Rhee et al. 2005].

VOF Waves

The VOF Wave model has been chosen to model the velocity of the ship, and naturally the incoming waves. According to [CD-Adapco 2018] also the air of the domain is modelled with this, ensuring an accurate estimation of the air resistance the model will face. There exists several different options for wave modelling in STAR, but the ones present in this thesis are the following:

1. VOF Flat Wave
2. 1st Order Wave
3. 5th Order Wave

The flat wave initializes the flow at the free-surface with a velocity, but without any other motion than in the specified direction (x, y or z). As such, it is perfect for modelling the velocity of a vessel during calm water.

The 1st order wave is modelled after the first order approximation of the Stokes theory of waves. It models the free-surface elevation, as given in equation 6.1 by [Pettersen 2007].

$$\zeta = \zeta_A \cos(kx - \omega t) \tag{6.1}$$

Where:

- ζ_A - wave-amplitude
- k - wave-number
- ω - wave frequency

The 5th order wave is modelled after the fifth order approximation of the Stokes theory of waves. Naturally, by including more terms, it resembles the wave more realistically, than what the first order approximation does. STAR models the 5th order approximation by equation 6.2, as given by [Fenton 1985].

$$\begin{aligned} k\eta(x) = kd + \epsilon_W \cos(kx) + \epsilon_W^2 B_{22} \cos(2kx) + \\ \epsilon_W^3 B_{31}(\cos(kx) - \cos(3kx)) + \\ \epsilon_W^4 (B_{42} \cos(2kx) + B_{44} \cos(4kx)) + \\ \epsilon_W^5 (-(B_{53} + B_{55}) \cos(kx) + \\ B_{53} \cos(3kx) + B_{55} \cos(5kx)) + 0(\epsilon_W^6) \end{aligned} \tag{6.2}$$

Where:

- ϵ_W - dimensionless wave amplitude, i.e wave steepness, $\epsilon = \frac{kH}{2}$
- B_{ij} - dimensionless constants

The boundary conditions at the outlet boundary has for all the different simulations in this thesis been set to the hydrostatic pressure of the initial wave system. However, when the flow is disturbed by the body, the flow approaching the outlet is not the same as the one at the inlet. In order to force the flow behind or far to the sides of the vessel towards the initial condition, wave forcing and damping has been implemented.

The damping option, uses the method derived by [Choi and Yoon 2009] and introduces a vertical resistance to vertical motions at a specified length in front of the boundary face, as shown in equation 6.3. This reduces the wave elevation and effectively damping them out before they reach the boundary surface. This helps inhibit wave reflection at the boundaries.

The wave forcing is achieved by adding a source term to the transport (momentum) equation. This method has its origins in the Euler Overlay Method by [Kim et al. 2012], and the source term is added by the use of equation 6.5.

$$S_Z^d = \rho(f_1 + f_2|w|)\frac{e^\kappa - 1}{e^1 - 1} \tag{6.3}$$

Where:

$$\kappa = \left(\frac{x - x_{sd}}{x_{ed} - x_{sd}}\right)^{n_d} \tag{6.4}$$

- x_{sd} - starting point for wave damping (propagation in x-direction)
- x_{ed} - end point of wave damping (boundary)
- f_1, f_2, n_d - parameters of the damping model

$$q_\phi = -\gamma\rho(\phi - \phi^*) \tag{6.5}$$

Where:

- γ - forcing coefficient
- ϕ - the current solution of the transport equation
- ρ^* - value which the solution is forced towards

Flow Solver and Turbulence Modelling

The Segregated Flow solver was enabled, due to the fact that [CD-Adapco 2018] recommended it for incompressible subsonic flows, which this is.

The two-layer realizible $k-\epsilon$ scheme was chosen with wall functions. [CD-Adapco 2018] state that this type of turbulence modelling will give better results than a standard $k-\epsilon$ scheme as it can be used to successfully model the viscous sub-layer. The wall functions are included to give the model more flexibility. The turbulence model $k-\omega$ SST could probably also have been used with success, and it has been used in other simulations, as by [Claud D. Simonsen et al. 2013]. However, the $k-\omega$ SST has its forte in modelling the viscous sublayer, [Klein et al. 2014]. As the results in this simulation is more dependent on pressure forces than viscous forces, this is not assumed to be of much importance, and the two-layer realizible $k-\epsilon$ with y^+ wall treatment is deemed sufficient.

The correct boundary layer thickness with respect to y^+ values was calculated by the use of the method shown in section 4. The boundary layer thickness was set at a size to obtain an y^+ value around 50, which is recommended by [CD-Adapco 2018].

DFBI - Dynamic Fluid Body Interaction

The Dynamic Fluid Body Interaction - DFBI option in STAR is made to calculate the translations, rotations, pressure- and shear forces the fluid imposes on the body, [CD-Adapco 2018]. By using this option, it is possible to allow, and monitor, the motions and forces that is exerted on the vessel.

6.4 Overset Mesh

Overset mesh, or chimera grid, technique is a method developed to increase the computational accuracy when simulating motions. According to [Hadzic 2006] when dealing with severe motions a standard structured, or unstructured grid, will be exposed to too large deformations and thus in need to regenerate the whole mesh. As with free-surface simulations this could lead to the free-surface to "fall out" of the refined mesh-area and into the more coarse regions. This in turn will lead to inaccurate results. With the overset mesh present, only local regeneration of cells needs to be implemented, and not on a global scale. In other words, there exists valid reasons to implement an overset mesh when it comes to simulations involving motions. This section will give a brief introduction into how it works, and thus why it has been implemented in some of the simulations in this thesis. This section is heavily based on the dissertation from [Hadzic 2006], as the overset mesh tool in STAR is based on it, and for a more detailed explanation of the overset mesh the reader is encouraged to read the dissertation.

[Hadzic 2006] presents a method which is designed to:

- achieve a strong coupling of all grids for an efficient iterative solution up to the round-off level of residuals
- provide smooth solutions in overlapping regions

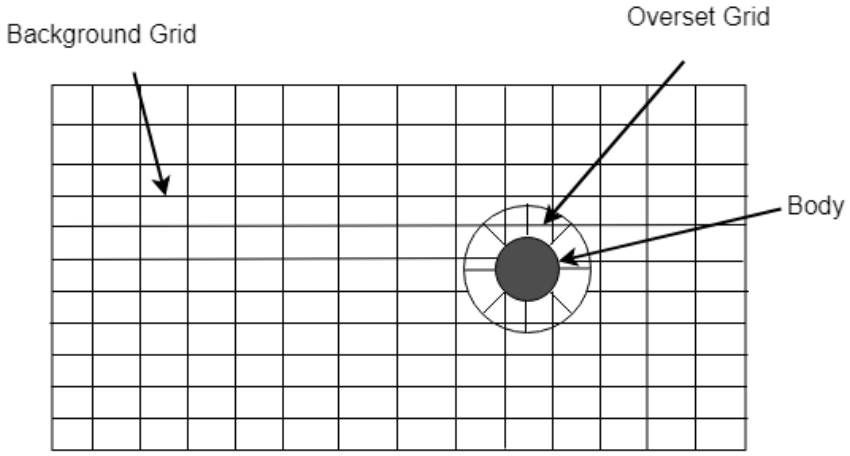

Figure 6.2: Background and overset mesh topology

- achieve global mass conservation across all grids
- be applicable to arbitrary polyhedral grids
- allow an arbitrary motion of bodies relative to each other

The overset mesh technique relies on dividing the mesh domain into a stationary background domain, and a sub-domain, as seen in figure 6.2. The method developed by Hadzic is grounded in two principal elements:

- decomposition of computational domain into sub-domains, and generation of a suitable grid in each sub-domain
- development of an coupling method for an accurate, efficient and unique solution of the governing equations on the overlapping grids.

An advantage with this set-up is that different grids can be developed for the background and the sub-domains, meaning separate grid controls and thus a more transparent mesh-control system.

The overset grid, or inner grid, is directly embedded in the background grid, meaning that the body which is of computational interest lies over the background grid. The background cells that are overlapped by the inner grid and the body, are thus outside of the computational domain, and needs to be removed from the ensuing simulations. Therefore, they can be physically removed which in turn will lead to fewer cells and less demanding computational resources. However, with a moving body the background cells that the body overlaps will change throughout the simulation and cells can therefore not be permanently removed as they might become part of the computational domain later in the simulation. Therefore, instead of removing the cells, they are as Hadzic calls them, inactive (hole) cells. To determine whether a cell is to be inactive or not, an artificial boundary between the body and the background mesh has to be created. Figure 6.3 shows the overlapping area between the inner grid and the background grid, the nodes in the centers of cells lying along the artificial boundary is marked with a "$\circ$". The nodes denoted as interpolation cells are cells obtaining the necessary computational information through interpolation by nearby "donor cells" in the other grid. In order to obtain a smooth inter-grid communication two steps are needed, as according to [Hadzic 2006]:

1. Hole cutting, to assess which cells are outside of the computational domain
2. Identification of interpolation stencils which are used to construct the interpolation formulas for grid coupling

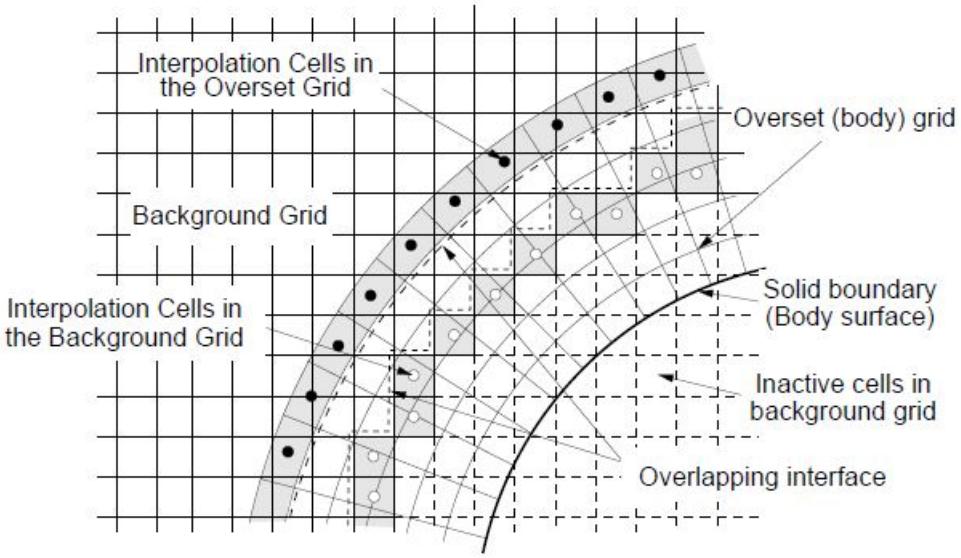

Figure 6.3: Overlapping grid interface, [Hadzic 2006]

Hole Cutting

The hole cutting procedure is very important as it determines which cells are to be excluded from the simulation, and which are kept as active. To ensure grid-interaction an overlapping area is kept which will contain the interpolation cells and donor cells. Figure 6.4 shows how this in practice is carried out. The curve, S, separates the cells in the background, the ones inside the curve will be inactive, and the ones outside is a part of the computational domain and active. However, as mentioned, an overlapping region to ensure grid-interaction is needed, so the area between the overset grid and the curve S will be denoted as the overlap region. Within this region the cells are kept, to exchange information between the two grid-domains.

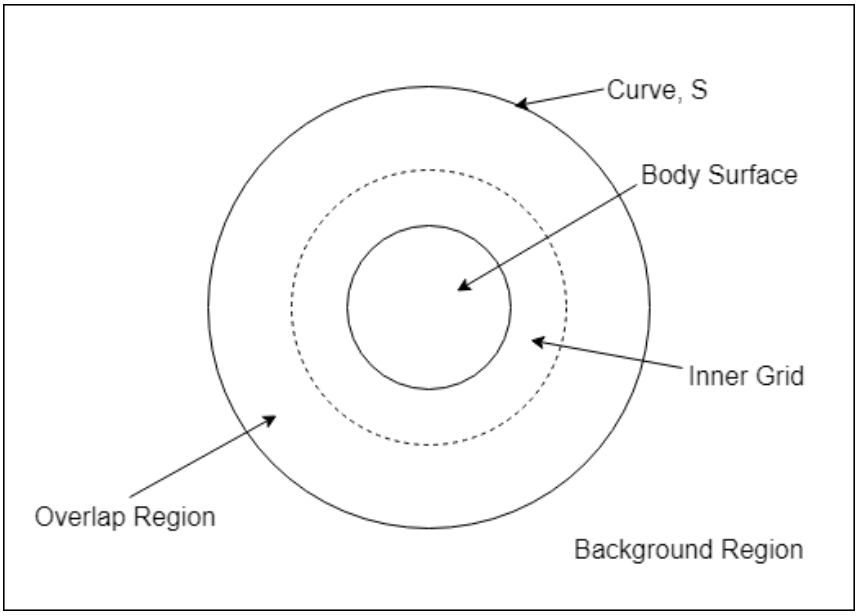

Figure 6.4: Discretization of the grid during hole cutting

Interpolation Stencils

As mentioned, the interpolation cell receives information from the donor cells that lies in the grid that overlaps it, so a good coupling between these two types of cells is required. According to Hadzic, the simplest method of interpolation scheme requires that only one cell whose centroid lies closest to the centroid of the interpolation cell should be identified. This is a so-called host cell, and if there is to be any other contributing donor cells they have to lie in the immediate "neighbourhood" of the host cell.

When all the donors are determined the value transferred to the interpolation cell is, according to [Hadzic 2006], determined through the use of equation 6.6.

$$\phi_{P_i} = \sum_{k=1}^{N_D} \alpha_{w_k} \phi_{D_k} \tag{6.6}$$

Where:

- ϕ_{P_i} - Interpolated function value at node P_i
- ϕ_{D_k} - Function value at point D_k
- α_{w_k} - Interpolation weights

Solution Procedure

With the inter-grid communication working at a satisfactory level, it is now a matter of accurate solving the governing equations. The solution needs to take the precence of holes in the grid into account, and provide grid couplings in overlapping areas. The treatment of inactive cells, grid coupling, and mass conservation through boundaries will not be given in detail here, but can be viewed in [Hadzic 2006]. Figure 6.5 shows the solution procedure of the overset grid technique.

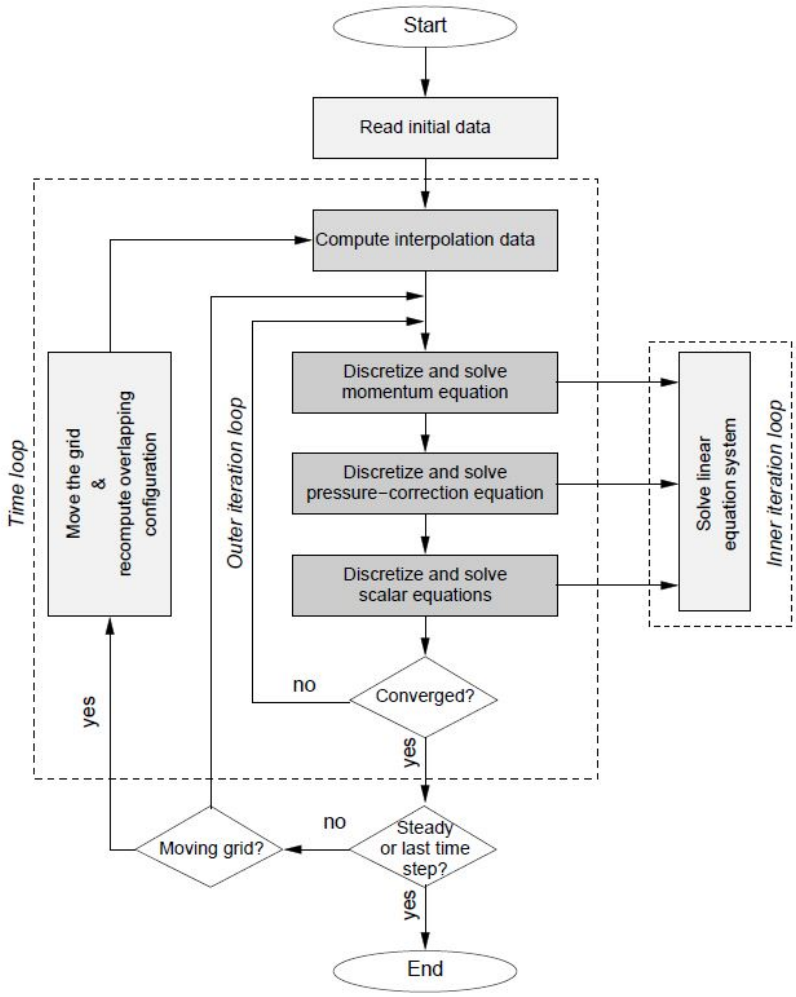

Figure 6.5: Overlap solution procedure, [Hadzic 2006]

Chapter 7

Results

As there are three different conditions tested in this thesis, the most transparent way of presenting them is to make a separate section for each of the simulation-types with their own go-through of the simulations and discussion. These sections will include the general set-up of the specific simulation, the obtained results and finally a discussion of the aforementioned results. This way it will be easier for the reader to follow the steps that were taken for each of the simulation-types. It is important to mention that the denotion η_3 and η_5 refers to the heave and pitch translation, also denoted as sinkage and trim, respectively. This is not to confuse the reader, but done to avoid repetitiveness in the paragraphs. In addition, to separate between the results from the two simulation types for each condition, the phrases "inviscid" and "viscous" are used to denote the results obtained in the inviscid and viscous simulation, respectively.

The set-up sub-section will include the specific domain and numerical set-up used for that particular simulation. As none of the simulations initially yielded satisfactory results, the changes implemented to the simulation and the subsequent difference in the result will be included here.

The result section will present the final results obtained, and a few, very short comments are made here. The ensuing discussion of the validity and overall quality of the results will be saved for the subsequent discussion sub-section.

In order to argue that the oblique simulation yields accurate results, a validation is necessary. As there do not exist any experimental oblique seakeeping tests with this model, at least none were found by the author, the only validation of the seakeeping set-up is with experimental results from head waves. The variables from the model tests are given in the 0th and 1th amplitudes of the time-dependent signal. This means the time-series that are measured during the simulations have to be Fourier transformed into the frequency domain.

The comparison between the experimental and numerical results are done by error estimating with the use of equation 7.1

$$E\%D = 100\frac{(D-S)}{D} \tag{7.1}$$

Where:

- D - Experimental result
- S - CFD result

As the calm water simulation approaches a quasi-steady result, statistical values, such as mean and standard deviations of variables will be presented to evaluate the convergence of the simulation.

Fourier Transformation of Results

The source of comparison is the 2010 Gothenburg Workshop in CFD, which contains experimental and numerical results on the model used in this thesis. While the Fourier transform is a well known, and much used, theory it will be given in brief here. This method is taken directly from [Stern et al. 2014].

The frequency of encounter for the ship, in Hz, is expressed as in equation 7.2:

$$f_e = f_w + \frac{U}{\lambda} \tag{7.2}$$

Where:

- f_w - initial wave frequency

The mean. phase and amplitude of the time history of the parameter $P(X, x, z, \Theta, \xi)$ are determined by using a Fourier series as follows:

$$P(t) = \frac{P_0}{2} + \sum_{n=1}^{N} P_n \cos(2\pi f_e t + \Delta\gamma_n) \tag{7.3}$$

$$\Delta\gamma_n = \gamma_n - \gamma_1 \tag{7.4}$$

$$a_n = \frac{2}{T}\int_0^T P(t)\cos(2\pi f_e t)dt \tag{7.5}$$

$$b_n = \frac{2}{T}\int_0^T P(t)\sin(2\pi f_e t)dt \tag{7.6}$$

$$P_n = \sqrt{a_n^2 + b_n^2} \tag{7.7}$$

$$\gamma_n = \arctan(-\frac{b_n}{a_n}) \tag{7.8}$$

Here, P_n is the n-th harmonic amplitude and y_n is the corresponding phase. Only the 0th and 1st harmonic amplitude will be computed and compared to the Gothenburg CFD results. The 0th and 1st harmonic amplitude corresponds to the mean and linear term of the unsteady time-history of the variable, respectively.

7.1 Calm Water Simulations

Calm water results are an important corner-stone for the validity of the rest of the simulations. While solver-options and physics-models may differ from calm-water - to wave-simulations, the over-all set-up is very much alike. It is therefore important to acquire good results at this stage, since if the calm water simulations are not accurate, one cannot expect to have any success with the regular-wave simulations.

Wave probes, which were used to measure the surface elevation along a line, had to be implemented in the domain at the same places as those that were used in the experiments. According to [Larsson, Stern, and Visonneau 2013], the following wave cuts were used: $\frac{y}{L_{PP}} = 0.0964, 0.1581, 0.2993$.

Set-up

With the calm-water simulation it is important to assess where there is a lot of changes to the fluid flow. As the velocity of the vessel is modelled by a flat-VOF-wave approaches with a velocity corresponding to $Fn = 0.142$, there is very little change in the fluid flow, especially far out in the domain. With this in mind, the need for a fine mesh only arises in areas where there occurs disturbances to the fluid flow. For the grid generation, it was important to identify areas of physical importance for the resistance, and motion calculations. As it is the waves generated by the vessel that represents the pressure-related resistance of the vessel, it is important to have a grid that captures this flow field accurately. In addition, for viscous solvers, the vortex shed behind the vessel is also important, so a finer grid is required here. With a shrewdly made mesh, cells can be as fine as they need, and grow to a set base-size to decrease the cell count, and increase the computational time. The final list of areas of interest is as follows:

- Free-surface
- Wave pattern generated by the vessel (transverse and divergent)
- Wake of the vessel
- Boundary layer and mesh close to the vessel

While coarsening the mesh away from the vessel is important, it was found that altering the vertical height of the cells in the free-surface in front, and around the vessel, gave an unstable and inaccurate free-surface. In addition, the horizontal mesh size was kept at a fixed size, only to be refined in the areas around the vessel, as this was also found to have a positive effect on the end-result. Therefore, the free-surface mesh was set to have a uniform size in the vertical direction, only to be coarsened far behind the vessel, and the horizontal size was kept at the same base-level throughout the domain except for the refinements around the vessel. With all the refinements of the mesh, the final cell-count became approximately 4.2M and 3.7M cells for the viscous and inviscid simulation, respectively. This difference is naturally due to the fact that there is no need for a boundary-layer mesh for the inviscid simulation.

As [Larsson, Stern, and Visonneau 2013] mentions, the Froude number is quite low, and thus the fundamental wavelength is also very low, $\lambda_f = 2\pi Fn^2$, so a large number of cells across the wavelength are needed to capture the free-surface accurately. This requirement is also present for the wave height. From [CD-Adapco 2018] a vertical realization of between 10-20 cells is necessary to capture the wave elevation. ITTC also recommended not using anything less than 40 cells over the wavelength, [ITTC 2014b]. However they also stated that this could be an unnecessary demand for low Fn simulations. This requirement is not followed in the far-field of the domain, due to the fact that there is nothing happening with the flow with respect to time, in this area. This is also due to the fact that increasing the cell size on the longitudinal directions far away from the vessel helps the wave dampening of the system and thus aids in the avoidance of wave reflections at the boundaries.

For RANS simulations a boundary layer mesh is needed to calculate the flow in the viscous sublayer. The size of the inner cells is dependent on the y^+ - value, which in turn is dependent on the fluid flow. A y^+ - value corresponding to 50 was estimated through use of the equations listed in chapter 4, as this value was found to yield the best results, both by [Azcueta 2001], and [CD-Adapco 2018].

To capture the Kelvin (divergent) wave system, volume controls were used and put in a triangular shape to mimic the Kelvin angle of 19.5° with respect to the center-line. The wave system mesh was refined in four layers, in order to have a smooth transition from coarse to fine mesh. This is due to the fact that an abrupt, large increase in mesh size can lead to reflection of the flow and cause instabilities. Therefore, the mesh was set to grow slowly throughout the domain in order to inhibit this. The final mesh-generation can be seen in figure 7.1 and 7.2. These figures do not represent the final simulation, but they are coarsened figures for the purpose of visualization.

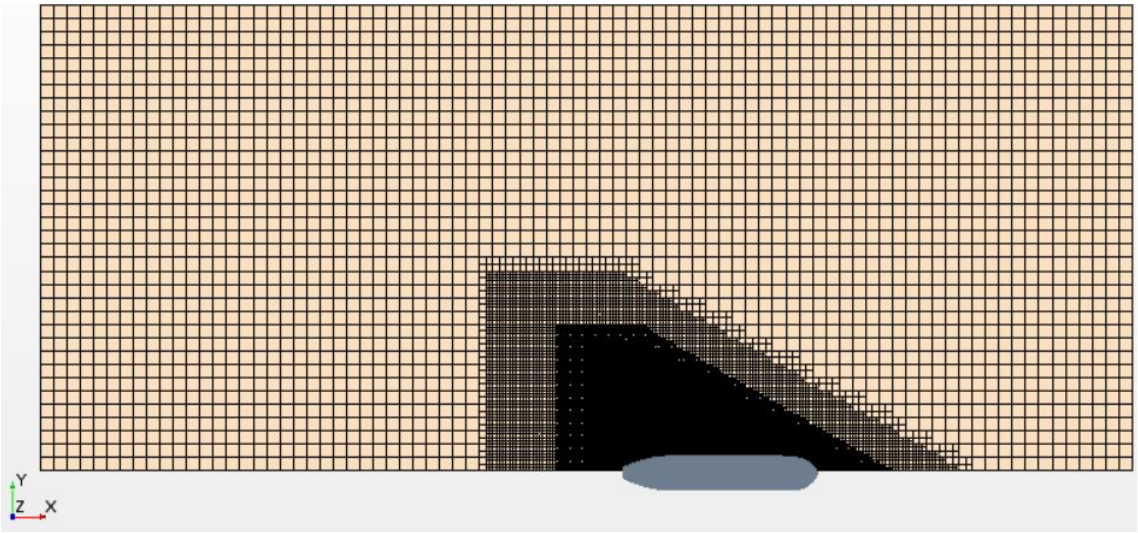

Figure 7.1: Free-surface mesh in the horizontal plane, calm water simulations

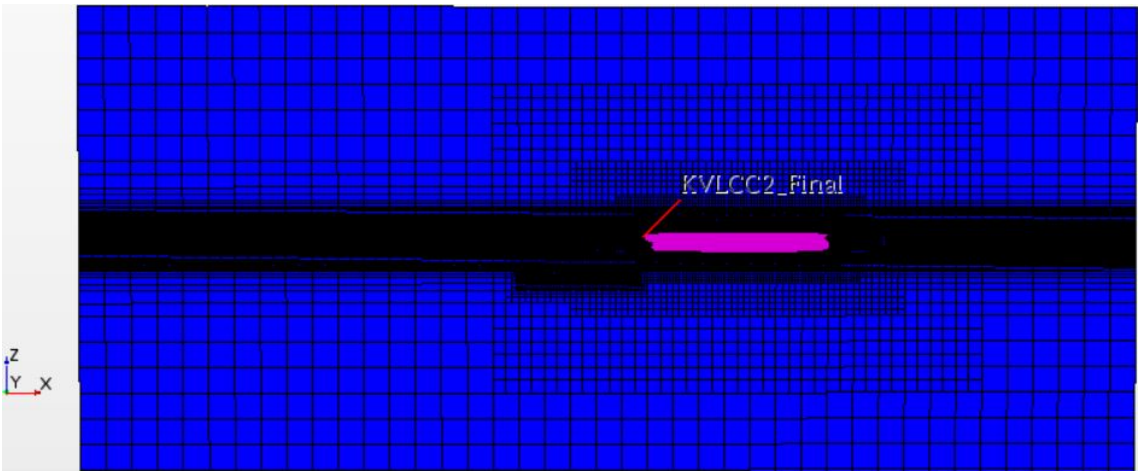

Figure 7.2: Mesh-generation overview in mid-ship xz-plane, calm water simulations

As the calm water simulations are to reach a quasi-steady state at some point, the time-discretization was set at 1st order. Due to the fact that the computed values are to reach a fixed value, the inner iterations for each time-step was set at 10. This is a conservative number, as a lower value would probably still yield accurate results. The inner iterations of the 6DOF-solver, which computes the forces and motions on the body, was set at 5, as according to recommendations from [CD-Adapco 2018].

At the boundaries, wave damping was enabled to force the solution towards the flat-wave condition. The wave-damping model is enforced at a boundary by specifying a damping length which defines the length from the boundary at which the damping starts. damping-length needs approximately two wave-lengths to completely dampen the wave. Therefore a relatively large lateral domain had to be used in order for the damping to work as it should. The finalized domain had the following dimensions, where all the measurements are taken from the coordinate-system origin to the respective boundary:

Table 7.1: Main dimensions of the computational domain, calm water

Dimension	Value
L_A	$3.2L_{PP}$
L_F	$2.9L_{PP}$
S	$2.9L_{PP}$
T	$1.3L_{PP}$
B	$2.6L_{PP}$

Where:

- L_A - origin to the outlet boundary
- L_F - origin to the inlet boundary
- S - origin to the side boundary
- T - origin to the top boundary
- B - origin to the bottom boundary

Results

The comparison between EFD and the RANS and Euler simulation, can be seen in table 7.2, and the viscous and inviscid pressure resistance can be seen in table 7.3.

The surface elevation plots can be seen in figures 7.3-7.5, and it is noticeable how similar they are, indicating that the waves generated by the body are pressure related forces, as indicated by wave-theory.

Table 7.2: EFD and CFD comparison of variables for RANS and Euler simulation, calm-water

Simulation	Variable	Value	E%D
EFD	C_T [-]	4.11E-3	-
	η_3 [mm]	-4.37	-
	η_5 [deg]	0.132	-
RANS	C_T [-]	4.05E-3	1.46
	η_3 [mm]	-5.67	-29.75
	η_5 [deg]	0.127	3.79
EULER	C_T [-]	0.292E-3	92.89
	η_3 [mm]	-5.68	-29.98
	η_5 [deg]	0.126	4.55

Table 7.3: Viscous and inviscid pressure resistance

$R_{P,Viscous}$ [N]	$R_{P,Inviscid}$ [N]
3.726	1.294

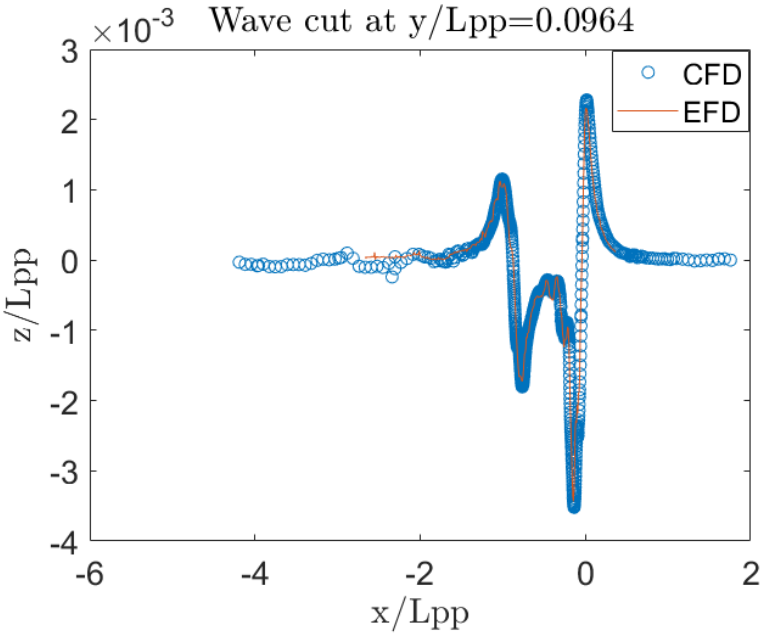

(a) RANS

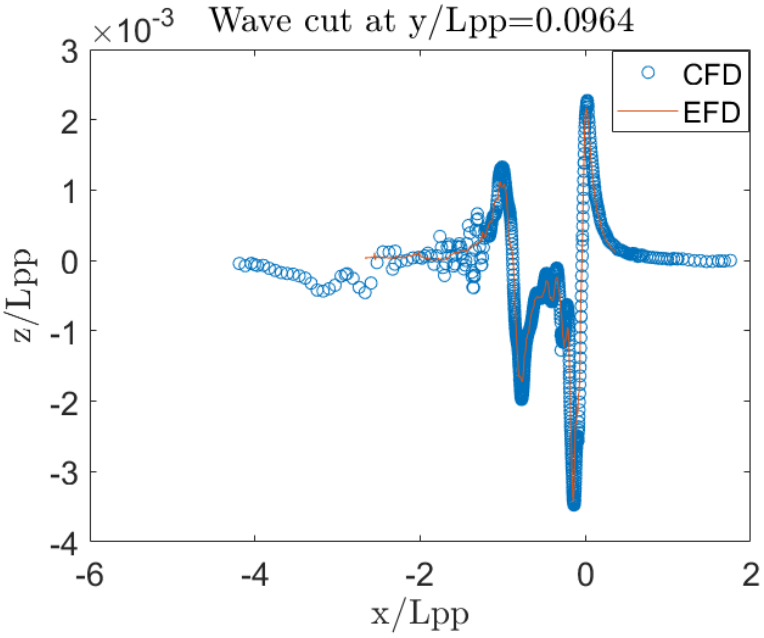

(b) Euler

Figure 7.3: Surface elevation plot at $\frac{y}{L_{PP}} = 0.0964$

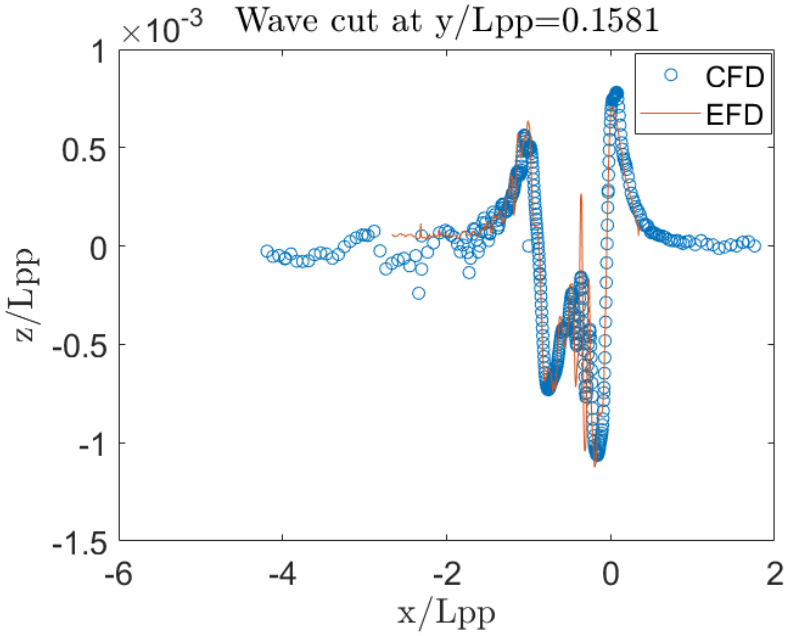

(a) RANS

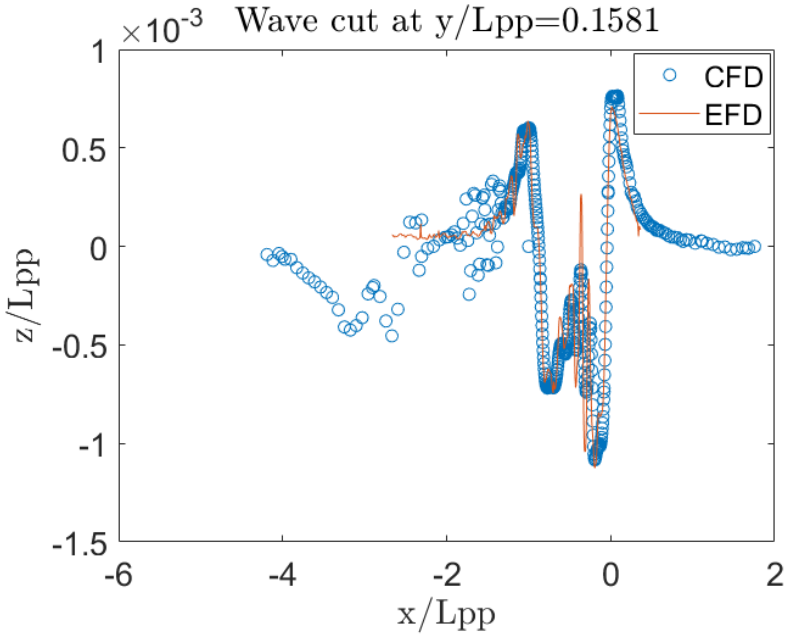

(b) Euler

Figure 7.4: Surface elevation plot at $\frac{y}{L_{PP}} = 0.1581$

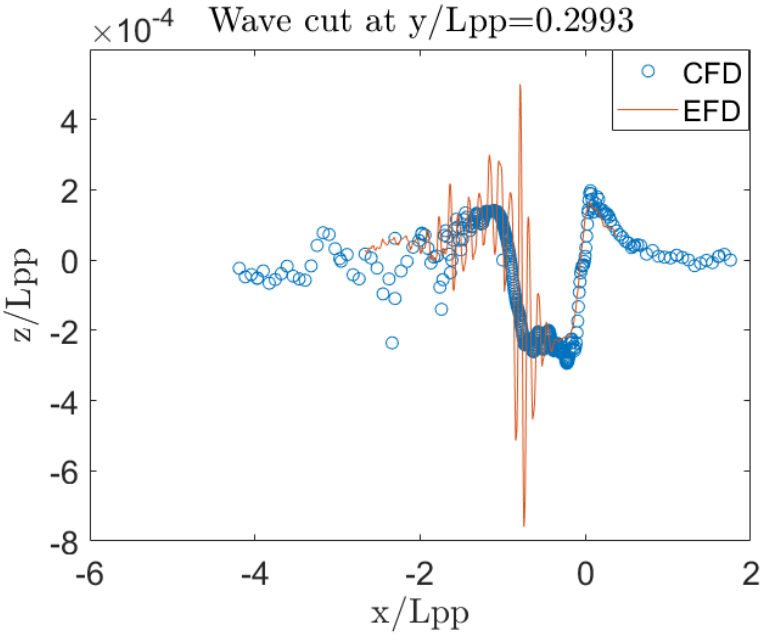

(a) RANS

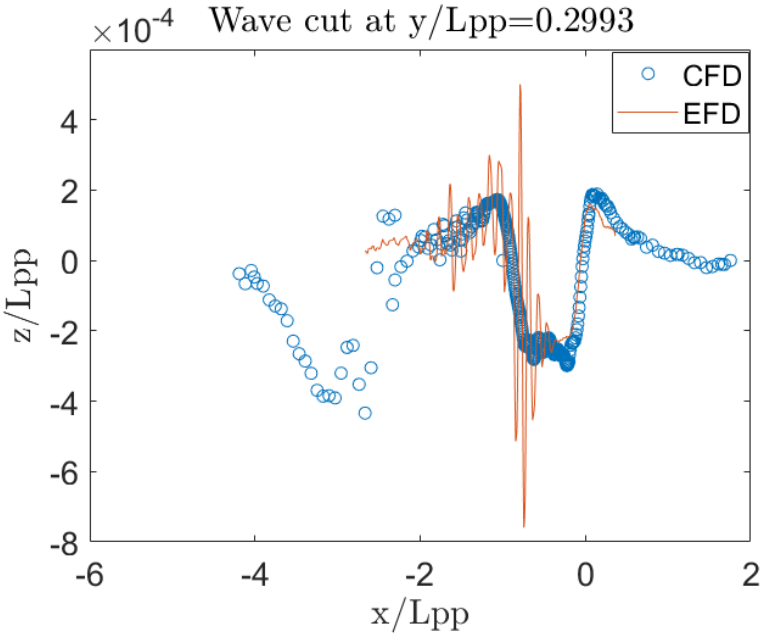

(b) Euler

Figure 7.5: Surface elevation plot at $\frac{y}{L_{PP}} = 0.2993$

Discussion

The viscous simulation agrees well with the experimental result on the resistance coefficient. Naturally, the inviscid simulation is way off on this value, but this is expected as it does not include its main contributor, the frictional resistance. However, the Euler simulation does calculate the motions of the vessel just as accurate as the RANS simulation, suggesting that these parameters are, as expected, pressure dominated forces. The sinkage of the vessel is inaccurately calculated, as it nearly deviates 30% from the experimental values. While this is a substantial relative error, the values computed are very small, so a small difference in value leads to a large relative error. The discretizational error could be the culprit, and with a refined mesh and adjusted time-step it is expected to drop. It would have been an advantage to check this, but due to computational time, and the fact that the simulations do capture the physical image occurring, it is deemed of less importance than completing the other simulations.

The viscous part of the pressure resistance is very substantial to the total pressure resistance. This can easily be seen from table 7.3, where the inviscid pressure calculation is off by 65%, relative to the RANS calculation. The deviancy makes up approximately 13% of the total resistance, so even if one were to suplement the Euler simulation with a good frictional resistance estimation, the total resistance would still be inaccurate. However, it is expected that the inviscid simulations will become more accurate with an increased Froude number. With a $Fn = 0.142$ the inviscid pressure resistance is evidently very low. When the velocity of the vessel puts the Froude number above 0.2 the waves generated by the vessel will become much larger than they are now, and thus yield a much lower relative error for the inviscid simulation. The relative difference between the viscous and inviscid pressure resistance is also expected to be far less for the regular waves simulations.

Both the viscous and inviscid simulations model the free-sureface elevation with an acceptable accuracy. However, the plots seems the decrease in accuracy the further away the wave-cuts are from the vessel. The magnitude of the oscillations are far smaller for the wave-cut that is the furthest away from the vessel, compared to the one that is closest, and the small values of oscillation can be partly blamed for this. Of course, the oscillations from the model tests might be subjected to errors themselves, as such violent oscillations with such small values can be hard to measure accurately. The inviscid simulation seems to have trouble with modeling the surface-elevation in the wake, compared to the viscous model. This is seen from figures 7.3, 7.4 and 7.5 at $\frac{x}{Lpp} = -2$. This could be due to the viscous dissipation that is not present in the Euler simulations. As the rest of the results agreed fairly well with the experimental values, and the flow-field was captured with reasonable accuracy, any further analysis with regards to enhance the surface-elevation plots were not conducted. The smallest mesh-size in the free-surface was approximately 3mm, and it is expected that with a finer mesh in the free-surface and a coherently smaller time-step, the free-surface is expected to be modelled with a greater success.

While a 1st order time-discretization scheme has been used, which is unconditionally stable, a time-step analysis could be beneficial to the final result. A simulation including a free-surface deserves extra attention with regards to the CFL number, as there are a lot of changes near the interphase between the air and water. Böhm and Graf suggested a CFL number below 0.5 and indicated that above this could yield numerical instabilities. While this could be true with a free-surface where a lot of changes occur over time, such as a wave-simulation, there is not that much happening during a calm-water simulation test. This is evident by the accurate computed results, but a smaller time-step could prove beneficial for the standard deviation of the resistance. As seen in Appendix A, the standard deviation is around 1% of the total value, so while this is deemed as quasi-steady, a smaller time-step could reduce it. However, it is likely that it would yield a free-surface realization, as with a small enough cell-size and a coherently small time-step, the changes in the fluid flow with time could be captured. From figures 7.4 and 7.5 the values for the abrupt, and large oscillations seems to be "smeared" to a more steady value. A too high CFL number could lead to important fluid flow information passing through a cell without being taken into account. For these surface elevation plots, which seems more time-dependent than the resistance and motion calculations, a second-order time scheme might be more appropriate.

As the mesh count of around 4M cells is finer than a lot of comparative papers published on the

same topic, there is reason to believe that the cell-count can be reduced without compromising the results. A domain-analysis could have been done, in order to see if the computational domain can be reduced. In addition, if a time-step analysis has been computed, a mesh-refinement analysis can be done to see how coarse the mesh can be, and still obtain accurate results. These analyses would give a more time-efficient, and as such a more sophisticated simulation, but as the next simulations are regular wave-simulation it was not done, as the result would not be directly transferable. The waves would impose a stricter demand to the time-discretization and if the time-scheme would be changed to 2nd order, a completely new time-step analysis would have to be done. In addition, wave-modelling has its own requirements when it comes to free-surface meshing, so the results obtained at the calm-water mesh analysis would be useless in this aspect. They would have been done, if there was time to spare, but due to the large computational time for the oblique simulations, there was simply not enough time to do this. As this is the initial simulation, made only to support the argument that the regular wave simulations are accurate and stable, further analysis of domain-, grid- and time-dependency has not been conducted. As the main part of this thesis is to evaluate oblique sea conditions with viscous and inviscid simulations, these tests are deemed more important to do at the regular wave simulations, as these have more in common with the oblique condition. And as such, these results were deemed as sufficiently good, making further analyses in the calm water condition superfluous.

There is no doubt that more accurate results can be achieved with regards to the results obtained here. However, as the standard deviations of the variables, listed in Appendix A, are low for both simulations it would seem that the physical and numerical set-up is stable enough to capture the physics of the problem. It is therefore deemed good enough to use this set-up as the basis for the regular wave condition.

7.2 Head Wave Simulations

As the wave-resistance is proportional to the squared of the incoming wave-amplitude, it is important to model the waves accurately. In chapter 6 a number of different methods for wave-modelling was introduced, and in order to establish what could be the best set-up, a lot of simulations were conducted at this stage, with respect to wave modelling. Another reason for doing a lot of simulations at this stage is because there are no available sources or experiments on oblique seakeeping with the KVLCC2, so the regular waves had to be validated in its stead.

Set-up

The wave-characteristics can be viewed in table 7.4. The wave is the exact same as the one that was used by NTNU in the experimental studies on the same model, [Stern et al. 2014].

Table 7.4: Regular wave characteristics

Parameter	Value
λ/L	0.9171
H/λ	1/34
Fn	0.142

As the wave-system imposes a larger change in the free-surface over time, a 2nd order time-discretization was initially chosen. The relation between the wave propagation, and the chosen time-step is crucial for the modelling of the wave-propagation over time. According to [Jin et al. 2017] the time-step should be chosen based on equation 7.9. This corresponds well with the recommendation from [CD-Adapco 2018], albeit with a safety factor of 2. The time-step was then set accordingly to equation 7.9.:

$$\Delta t = \frac{T_P}{4.8N} \tag{7.9}$$

Where:

- T_P - wave period
- N - number of cells per wavelength

The velocity of the vessel could either be modelled by moving the vessel and grid with the fixed ship velocity, or by having an incoming current and wind equivalent to the ship velocity in addition to the incoming waves. The latter was chosen, due to the fact that most literature found used this kind of a set-up and the experience of the author with STAR did not encourage any more stray from the trodden path than necessary. In addition, a moving grid would increase the computational time, and for these types of simulations the potential gain in accuracy is arguably not enough to justify it. A Stokes 1st order wave was initially chosen to model the wave train, for computational efficiency.

For each solver there are under-relaxation factors that aids the convergence of the solution. For simulations reaching steady-state solutions these can be set higher than for transient solutions, and for the calm water simulations they were set at 0.7, 0.4, 0.8 and 0.8 for the velocity, pressure, volume fraction and turbulence model respectively. The pressure and volume fraction parameter were kept at the same value, but the velocity and turbulence parameter were changed to 0.8 and 0.6, respectively, due to the recommendation by [CD-Adapco 2018].

The mesh size was set to have 80 cells over a wavelength, and 20 cells in the waveheight, as was suggested by [Jin et al. 2017]. In addition the overset mesh technique was used in order to model the motions of the vessel more accurately. This inner domain was made just large enough to encapsulate the vessel, with an extra space of 50cm in every direction. This was due to the fact that if a large overset mesh domain was made, the pitch angle of the model would yield large translations to the outer cells in the overset mesh, and thus could crash the simulation due to a lack of interpolation cells.

The cells in the free-surface were set to grow in the horizontal plane as they moved further away from the vessel. A wave damping boundary condition was enabled at the boundaries. This resulted in a poorly realized free-surface, as seen from figure 7.6. Notice the contour bar at the bottom of the figure, showing that even the largest values were far away from the actual wave amplitude ($\pm 7.5cm$).

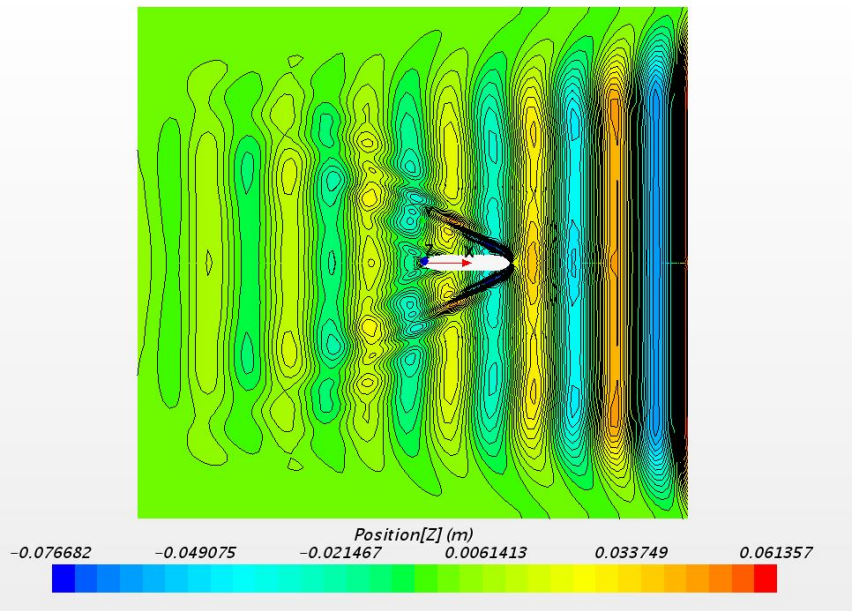

Figure 7.6: Poorly realized free-surface with wave damping model, head-wave simulation

Due to this, the wave damping boundary condition was changed to a wave forcing boundary, and

implemented at the outlet, side and inlet of the domain. This would keep a steady free-surface throughout the domain, as well as inhibit wave reflections of the bow to hit the inlet, and disturb the solution. As the wave forcing length is supposed to be around the length of the vessel, the domain to the sides were shrunk to decrease the computational time. The result of the free-surface realization can be seen in figure 7.7 and the resulting domain can be seen in table 7.5.

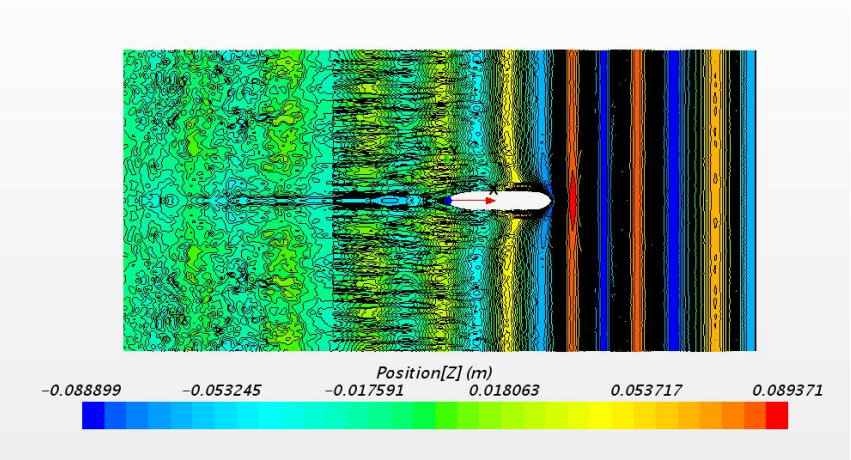

Figure 7.7: Free-surface realization with poor constructed mesh and wave-forcing model, head-wave simulation

Table 7.5: Main dimensions of the computational domain, regular waves

Dimension	Unit	Value
L_A	L_{PP}	3.4
L_F	L_{PP}	2.25
S	L_{PP}	1.74
T	L_{PP}	0.5
B	L_{PP}	1.74

As can be seen from figure 7.7 the incoming wave amplitudes now matched better with the target value, but disturbances in the free-surface occurs straight after the waves hits the vessel. This is due to the cells in the free-surface getting expanded far out in the domain. As the solution now is being forced towards a wave-amplitude of 7.5cm throughout the domain, the mesh needs to be just as fine at the sides and in the aft as at the inlet. In addition, it was found that the values of the wave amplitude got distorted near where the mesh changed size. Therefore, the mesh was set to have a uniform vertical and horizontal size throughout the domain, and the areas of mesh-transitions were moved farther away from where the wave actually was. This greatly increased the cell count for the simulation, but as can be seen in figure 7.8, it greatly improved the free-surface realization.

Initial Results

The contour plots above are great for an initial evaluation of the free-surface, but they do not give an exact image of the resulting wave-elevation. Therefore, point-probes were set at three different lines in the free-surface, 0.05m, 2m and 6m in y-direction measured from the origin. Along these lines, three points were set at, 11m, 7.5m and 0m in x-direction measured from the origin, and these points measured the surface elevation.

The wave-elevations from the initial simulations can be seen in figure 7.9, 7.10 and 7.11 representing the wave-probes from the line lying in the xz-plane with $y = 2m$ with x-position equal to 11m and 7.5m, respectively. The two red lines indicate what level the model is specified to reach.

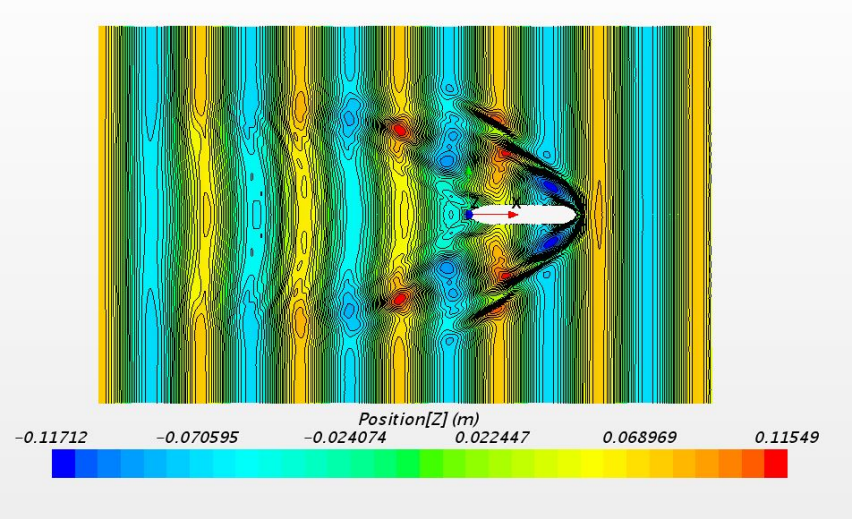

Figure 7.8: Steady free-surface realization with wave forcing model, head-wave simulation

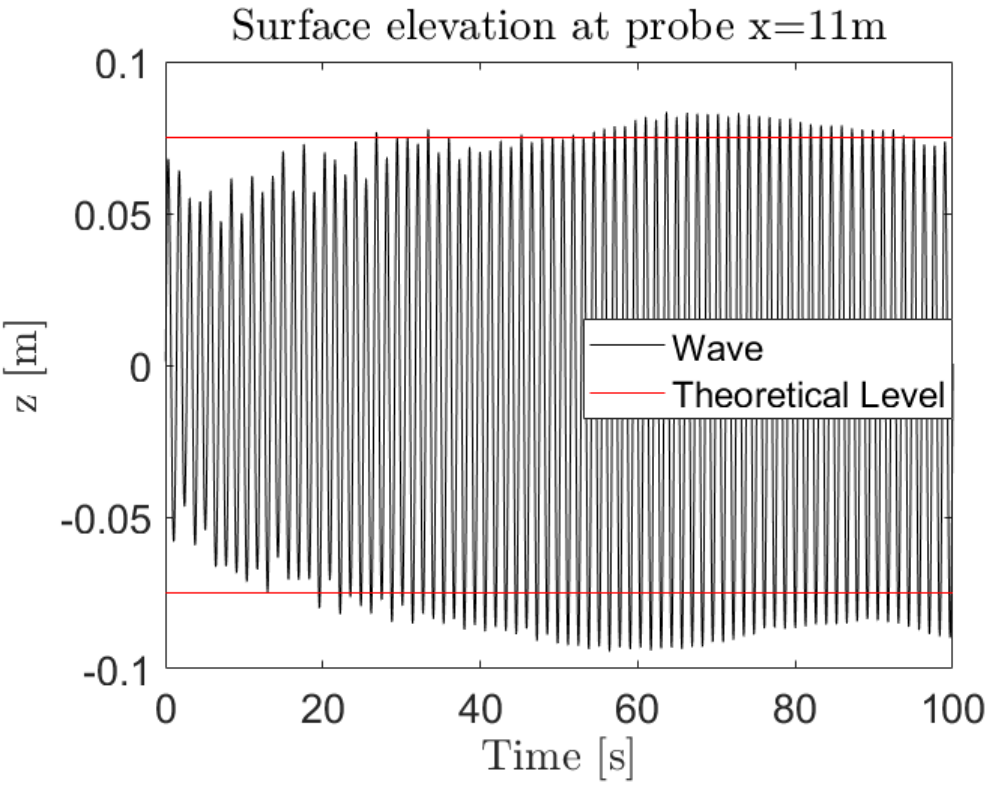

Figure 7.9: Wave probe at y=2m, x=11m, 2nd order time discretization, $CFL > 1$

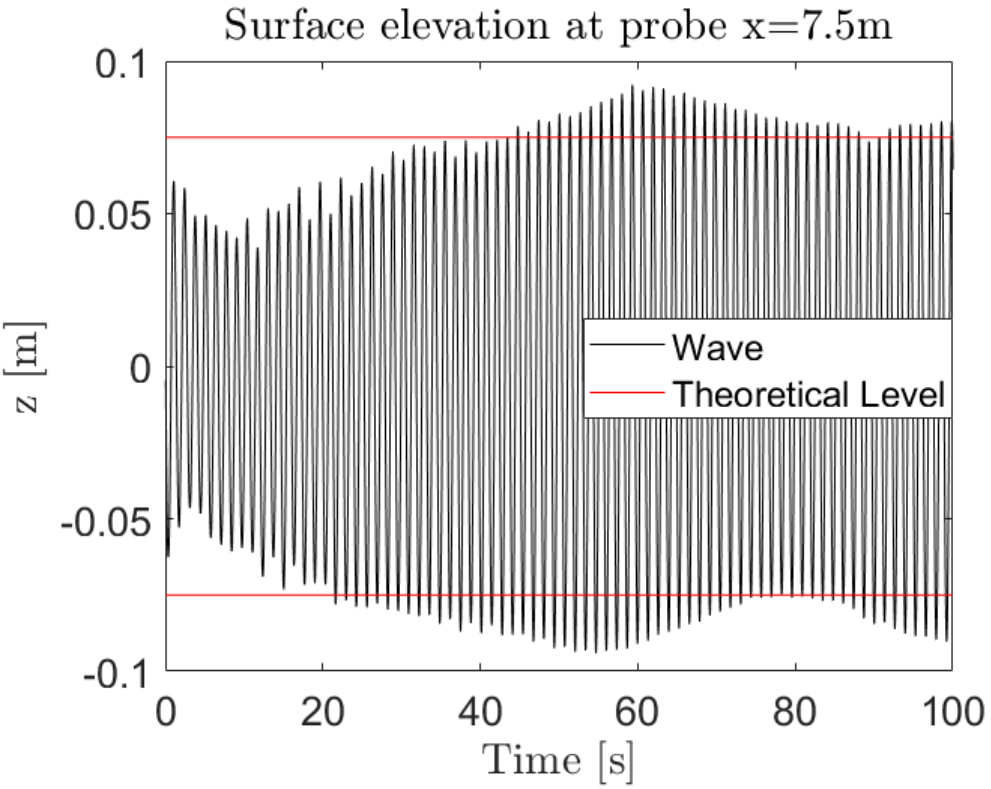

Figure 7.10: Wave probe at y=2m, x=7.5m, 2nd order time discretization, $CFL > 1$

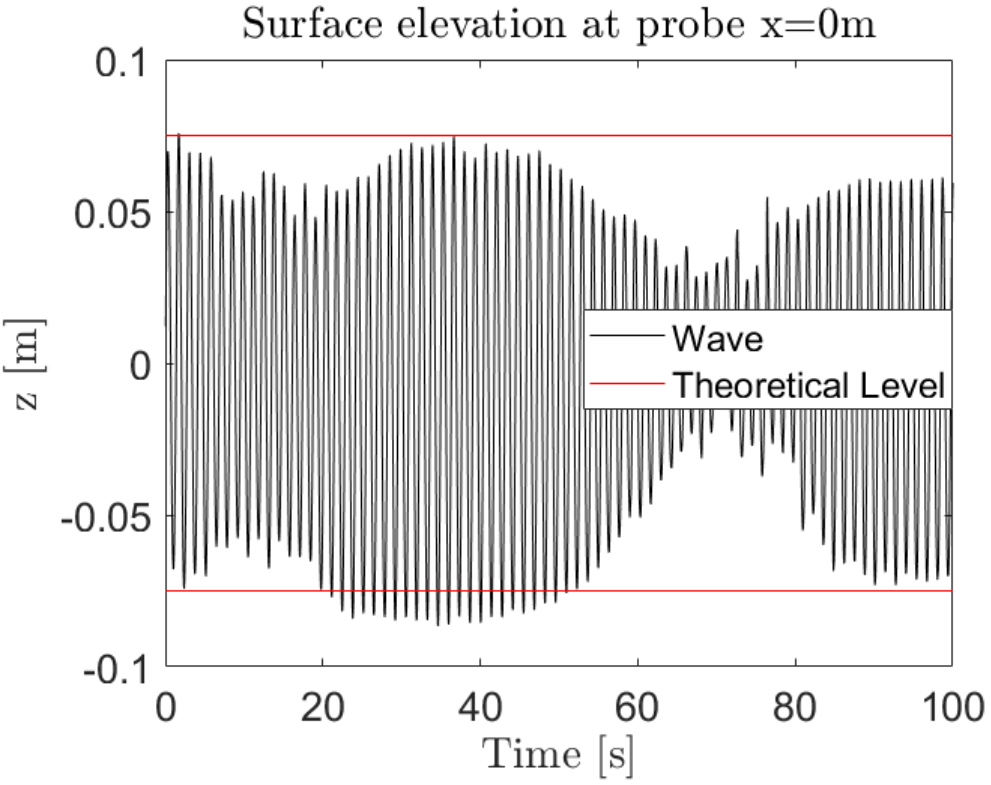

Figure 7.11: Wave probe at y=2m, x=0m, 2nd order time discretization, $CFL > 1$

As can be seen from the figures above, the wave is not being accurately modelled. According to [CD-Adapco 2018], the 2nd order time-discretization is more CFL-dependent than the 1st order time-scheme. Therefore, the instabilities seen above could stem from a too large CFL number in the free-surface which was higher than 1 in cells very close to the hull. As decreasing the time-step would increase the computational time, and time was of the essence at this stage, an attempt to try the 1st order scheme was made. This attempt was folly, as the 1st order time-discretization scheme dampens the wave elevation through the domain, as can be seen by figure 7.12, 7.13 and 7.14, showing wave probes at x = 11m, 7.5m and 0m from the origin, respectively.

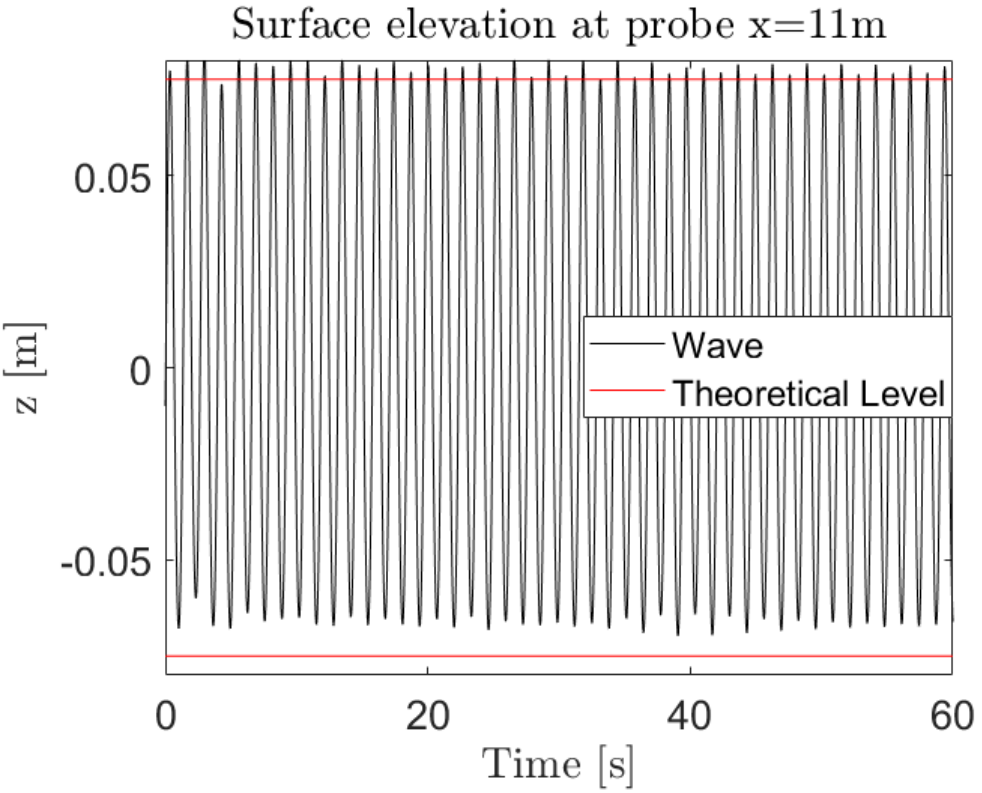

Figure 7.12: Wave probe at y=6m, x=11m, 1st order time discretization, $CFL > 1$

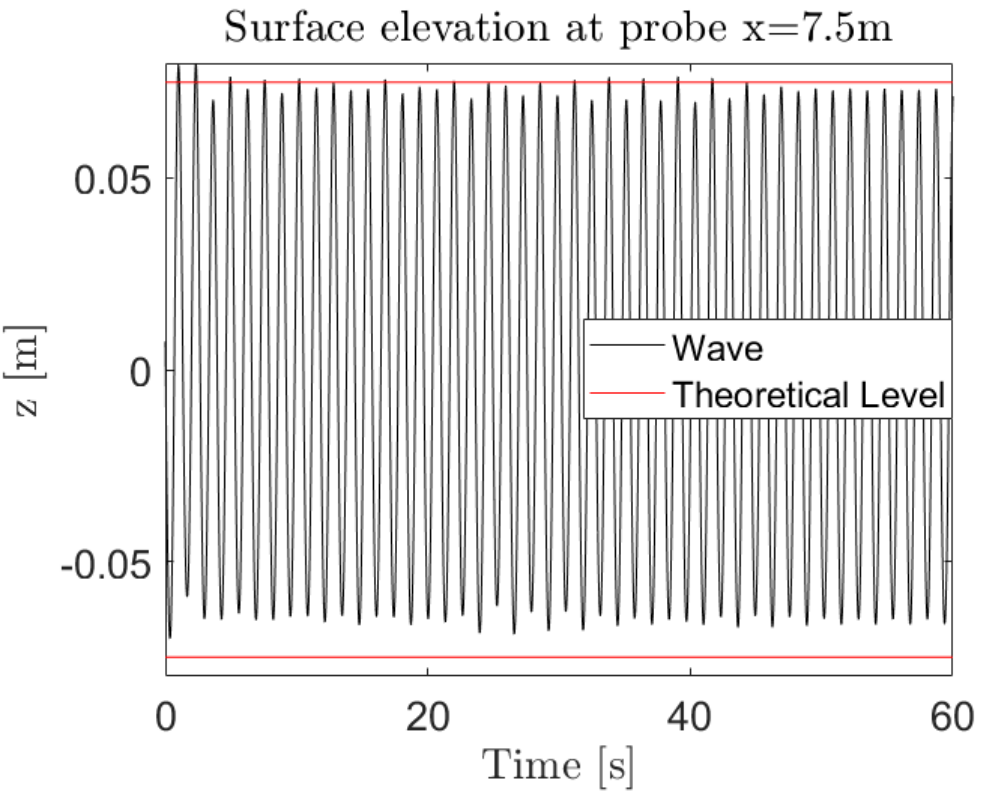

Figure 7.13: Wave probe at y=6m, x=7.5m, 1st order time discretization, $CFL > 1$

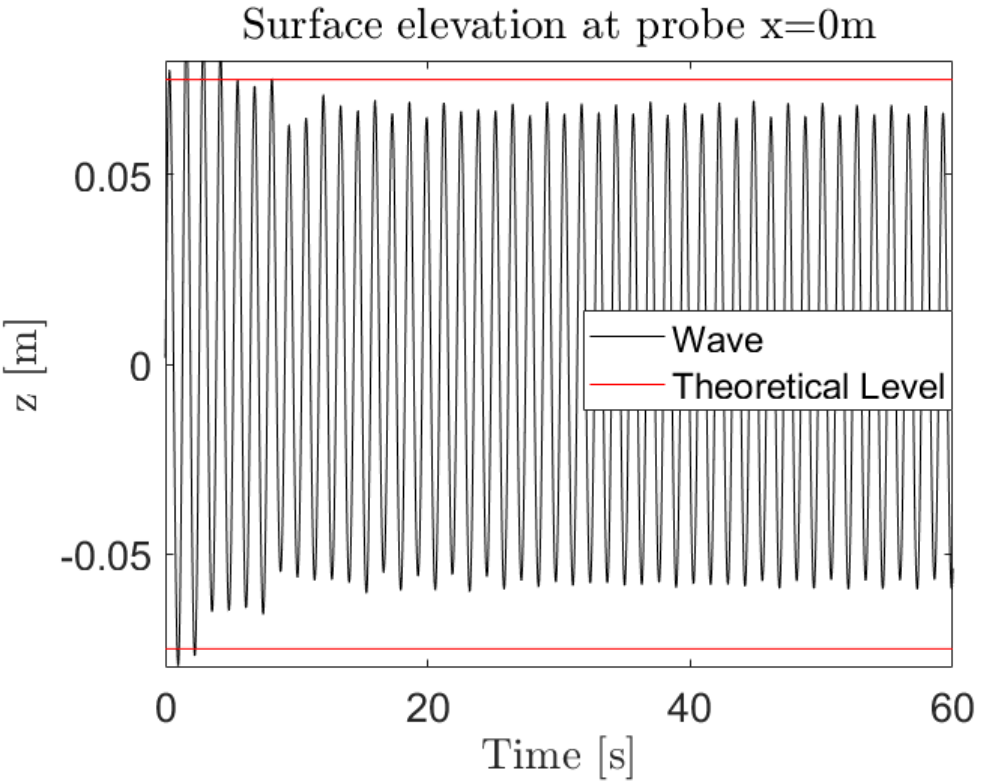

Figure 7.14: Wave probe at y=6m, x=0m, 1st order time discretization, $CFL > 1$

To cope with these problems, several issues had to be addressed. One problem is with the HRIC scheme, when the flow-velocity direction is parallel to the interface, the downwind scheme can distort the free-surface, [CD-Adapco 2018]. The smoothness of the free-surface and its ability to follow grid lines, is upheld by the angle factor, C_Θ, and for wave simulations that go on for longer than 20λ, it is recommended to increase this factor from 0.05 to 0.15-0.2 [CD-Adapco 2018].

A second problem is with the free-surface interface. The two multiphases interacting here will have solution discontinuities across the interface. This causes parasitic currents caused by discretization errors where the material properties of the two phases are discontinuous. This will undoubtedly distort the free-surface and therefore yield an uneven representation of the incoming waves. To cope with this problem, [CD-Adapco 2018] recommends using an "Interface Momentum Dissipation Model", with an artificial viscosity between 0.1-0.2. It ads an extra momentum dissipation in the proximity of the free-surface to dissipate the parasitic currents.

A problem throughout the simulations done for the regular waves, has been a high turbulence viscosity ratio value. This value expresses the ratio between the turbulent viscosity ratio and the laminar viscosity ratio, and a very high turbulent viscosity deteriorates the solution. To cope with this, the turbulent kinetic energy, k, and the turbulent dissipation rate, ϵ, is being forced to 1e-5J/kg and 1e-$4m^2/s^3$ respectively at the inlet, outlet and sides as according to recommendations from [CD-Adapco 2018].

It was found that the Stokes first order wave approximation was not able to keep an even wave amplitude throughout the simulation-time, so the 5th order Stokes approximation was instead implemented. Although, the first order wave is not the only culprit. As mentioned above, the 1st order time discretization scheme proved inefficient to model waves. The 2nd order scheme was therefore reinstated as the time-scheme, and the time-step was set accordingly to achieve $CFL < 1$ in the smallest cells.

The last problem, and one of the bigger, was to check the mesh in the free-surface. One would be inclined to believe that as long as the time-step is small enough, the finer the mesh in the free-surface the better, in regards to accuracy. However, while a finer mesh is better than a coarse one, it is important that it is refined in all directions, and not only in z-direction. While this had already been done, by enforcing 80 cells along the wavelength and 20 cells over the wave-height, the aspect-ratio between the two refinements was not taken into account. An important element of free-surface gridding, is the aspect-ratio between the cells. According to [CD-Adapco 2018], this value is also dependent on the wave steepness, and should for steep waves ($\frac{H}{\lambda} > \frac{1}{25}$) not be larger than 2, and for moderate steep waves an aspect-ratio of 4 should be kept. As the wave-simulations in this thesis uses a moderate steep wave, the number of cells over a wave height was reduced to 12, in order to get an aspect ratio of 4. Thus, the following changes was done, and the final result can be viewed in figures 7.15, 7.16 and 7.17.

- 2nd order time-discretization scheme enabled with focus on CFL-condition
- Grid refinement to keep an aspect ration of 4 in the free-surface
- 5th order Stokes wave approximation used to model the waves
- Changing the angle factor in the HRIC scheme from 0.05 to 0.15
- Enabling an "Interface Momentum Dissipation Model" with an artificial viscosity of 0.1
- k and ϵ set to spesific values at inlet, outlet and side boundaries

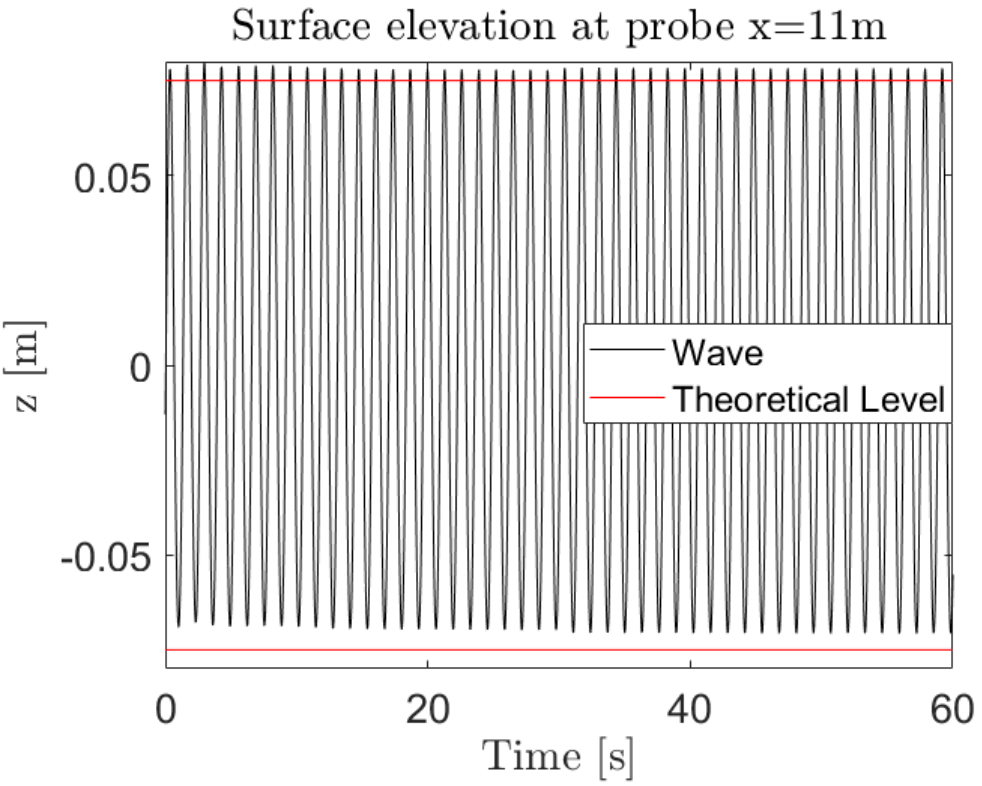

Figure 7.15: Wave probe at y=6m, x=11m, 2nd order time discretization, $CFL = 0.54$

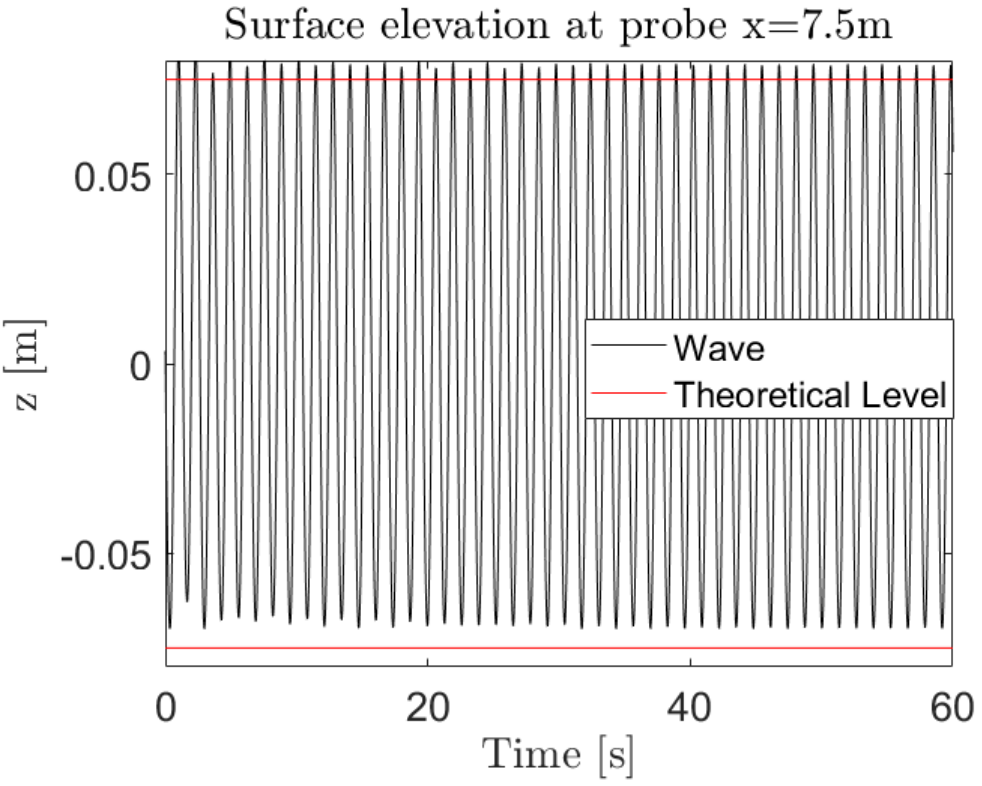

Figure 7.16: Wave probe at y=6m, x=7.5m, 2nd order time discretization, $CFL = 0.54$

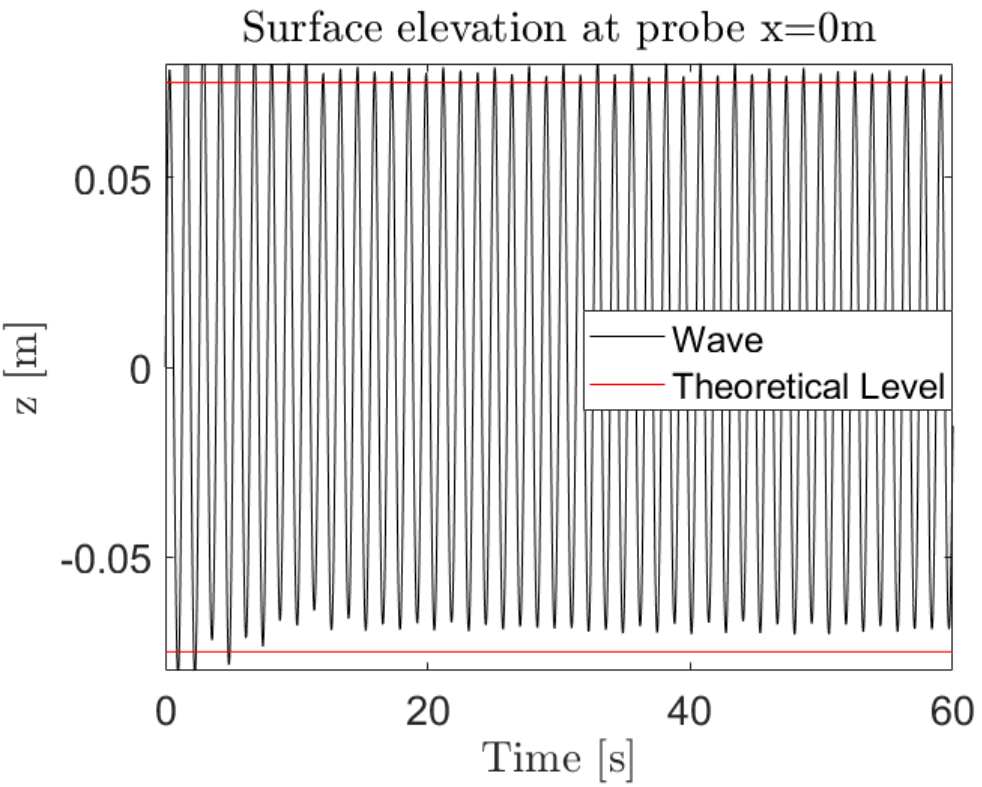

Figure 7.17: Wave probe at y=6m, x=0m, 2nd order time discretization, $CFL = 0.54$

Results

The estimations for the 0th and 1st amplitudes for the resistance, sinkage and trim can be viewed in table 7.6, along with the EFD and CFD results from the CFD workshop in Gothenburg. The time-series comparison of the pressure resistance, for the viscous and inviscid simulation, can be seen in figure 7.18. In addition, figure 7.19 shows a comparison of the maximum amplitudes. The inviscid simulation over estimates the values, but it also overestimates the negative amplitude. Extensive care has been taken to ensure that the time-series used in the Fourier-transform included only complete time-series, i.e stopped at the same position as where it started. It was found that this was extremely important, as the end result varied greatly with the chosen cut-off time-step. In Appendix B the rest of the results from the head-wave simulations can be viewed.

Table 7.6: Comparison between obtained results and EFD and CFD results from 2010 CFD workshop, from [Larsson, Stern, and Visonneu 2010]

Organization (Code)		R_T		η_3		η_5	
		0th Amp (N)	1st Amp (N)	0th Amp (mm)	1st Amp (mm)	0th Amp (deg)	1st Amp (deg)
EFD (NTNU)	D	59.359	603.078	-6.516	12.631	-0.137	1.357
ECN/CNRS	S	63.960	210.000	-5.910	13.230	-0.138	1.467
(ISISCFD)	E%D	-7.751	65.179	9.300	-4.742	-0.511	-8.106
ECN	S	65.500	230.500	-6.100	14.350	-0.145	1.504
(ICARE)	E%D	-10.35	61.78	6.38	-13.61	-5.92	-10.83
GL&UDE	S	-	-	-6.100	12.482	-0.91	1.323
(Comet)	E%D	-	-	6.38	1.18	-39.52	2.51
GL&UDE	S	-	-	-3.427	13.079	-0.118	1.358
(OpenFOAM)	E%D	-	-	47.41	-3.55	13.81	-0.07
Kyushu University	S	59.694	206.351	-8.499	9.929	-0.186	1.324
(RIAM-CMEN)	E%D	-0.56	65.78	-30.43	21.39	-35.87	2.43
Viscous Simulation	S	59.445	127.365	-6.380	9.083	-0.147	0.903
	E%D	-0.145	78.880	2.087	28.089	-7.299	33.456
Inviscid Simulation	S	43.365	113.486	-6.700	9.100	-0.149	0.945
	E%D	26.944	77.865	-2.820	27.955	-8.759	30.361

The resulting wave-plots can be seen in figures 7.20, 7.22 and 7.24. Only the latter part where the waves have reached a quasi-steady result has been included. From figure 7.24 it is noticeable that the surface-elevation becomes marginally more stable at 80s, so the part were the results have been calculated are from the interval 80-100s. It is apparent that the viscous simulation over-estimates the wave-crest and underestimates the wave-trough, by 2.5mm and 6mm at the most, respectively. The inviscid simulation agrees with the viscous simulation in regards to the crest, but is actually closer to the theoretical trough.

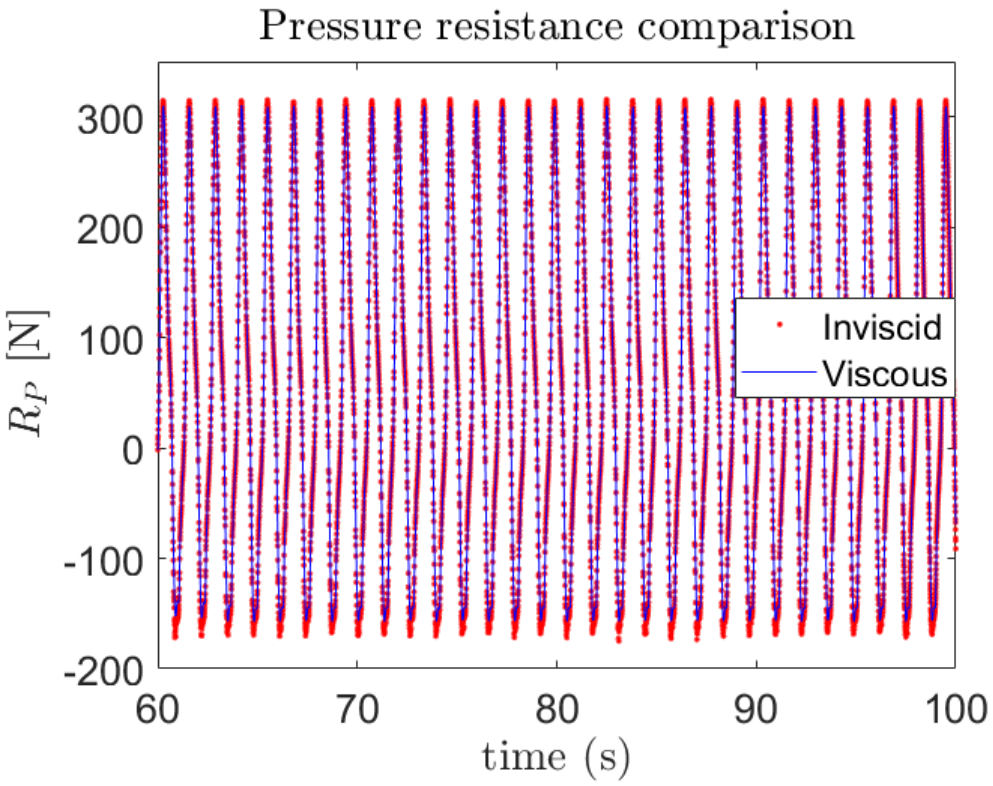

Figure 7.18: Pressure resistance comparison, head waves

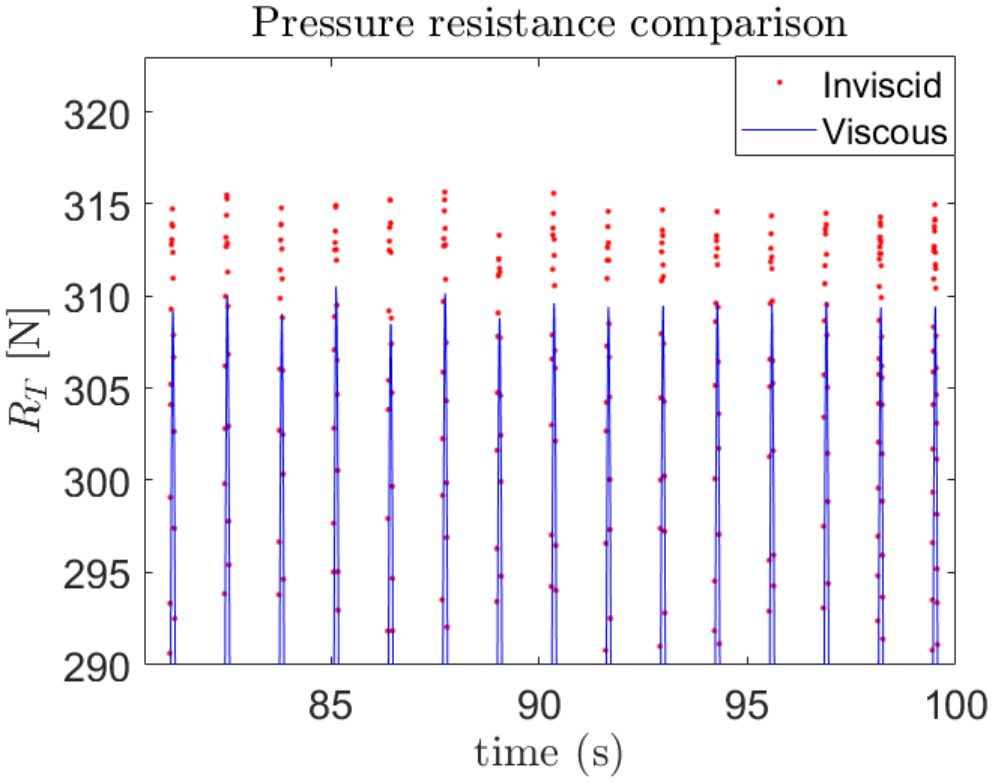

Figure 7.19: Max amplitude pressure resistance comparison, head waves

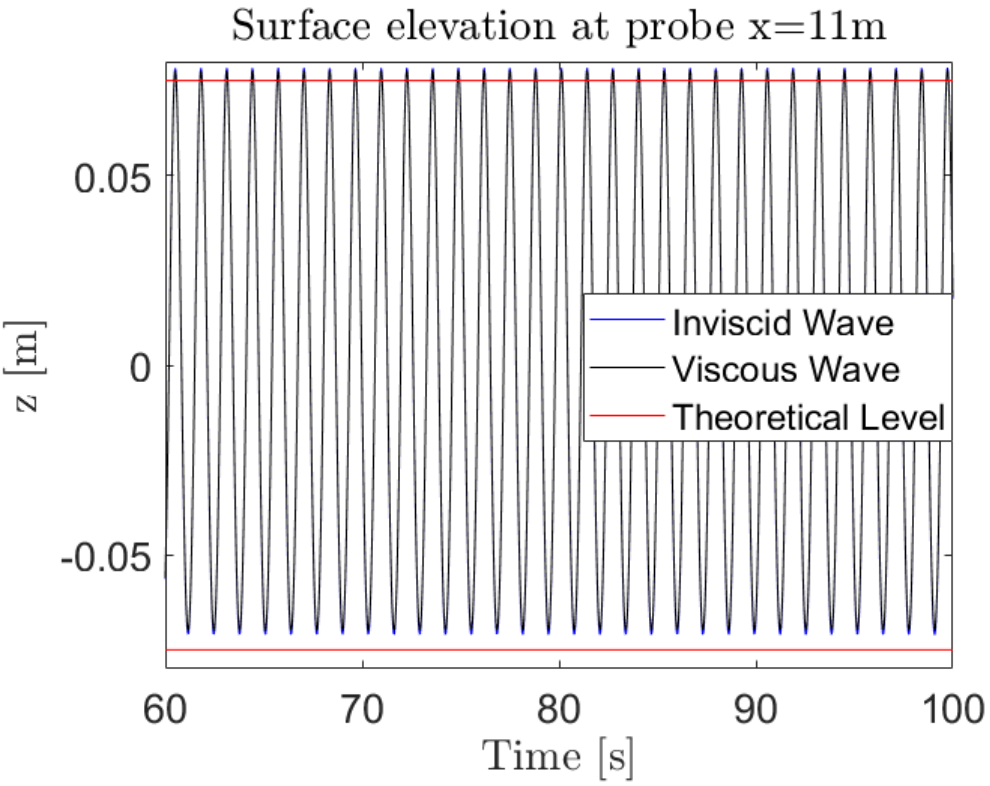

Figure 7.20: Result for wave probe at y=6m, x=11m

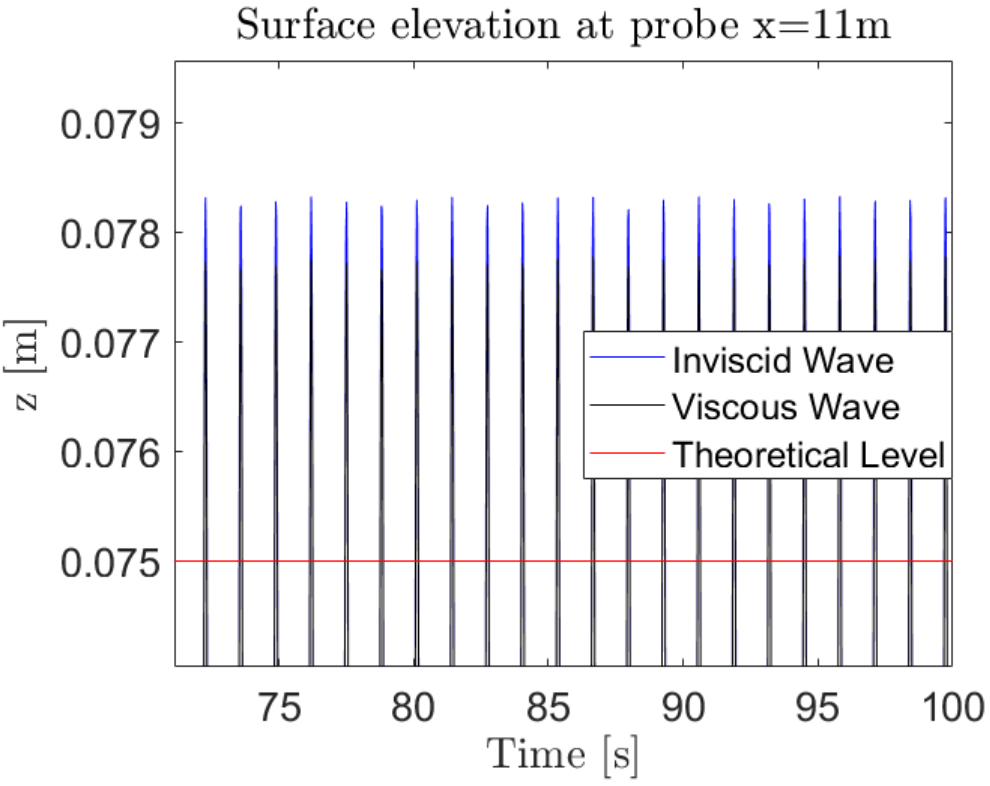

Figure 7.21: Maximum amplitude comparison for the surface elevation at y=6m, x=11m

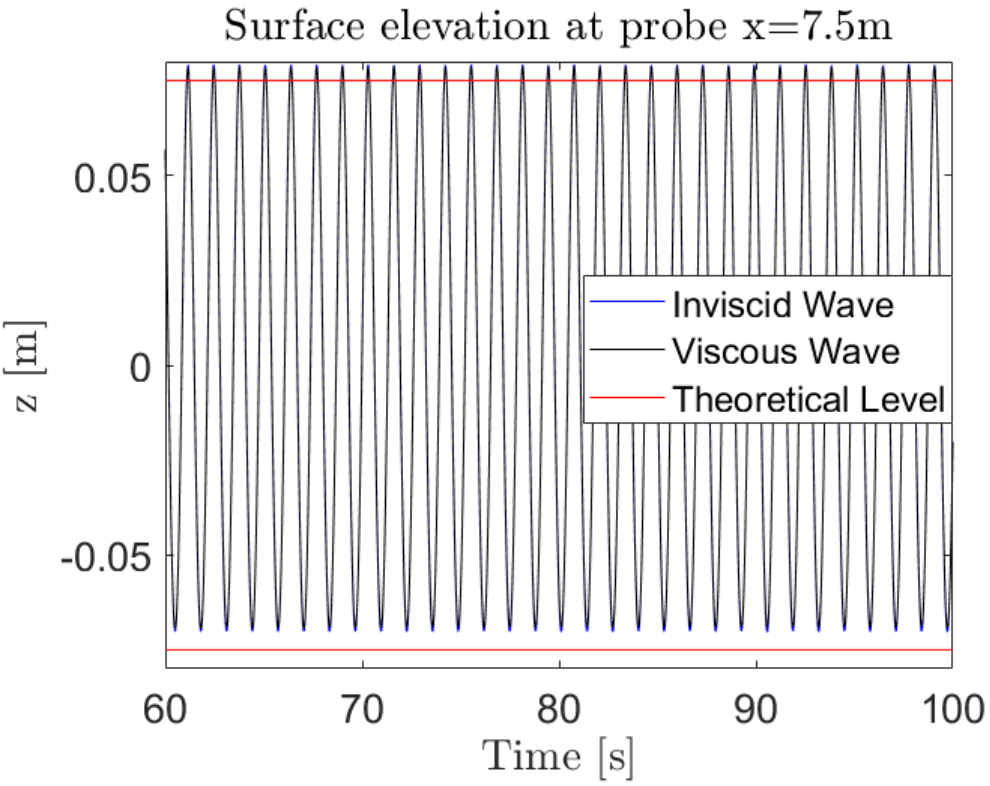

Figure 7.22: Result for wave probe at y=6m, x=7.5m

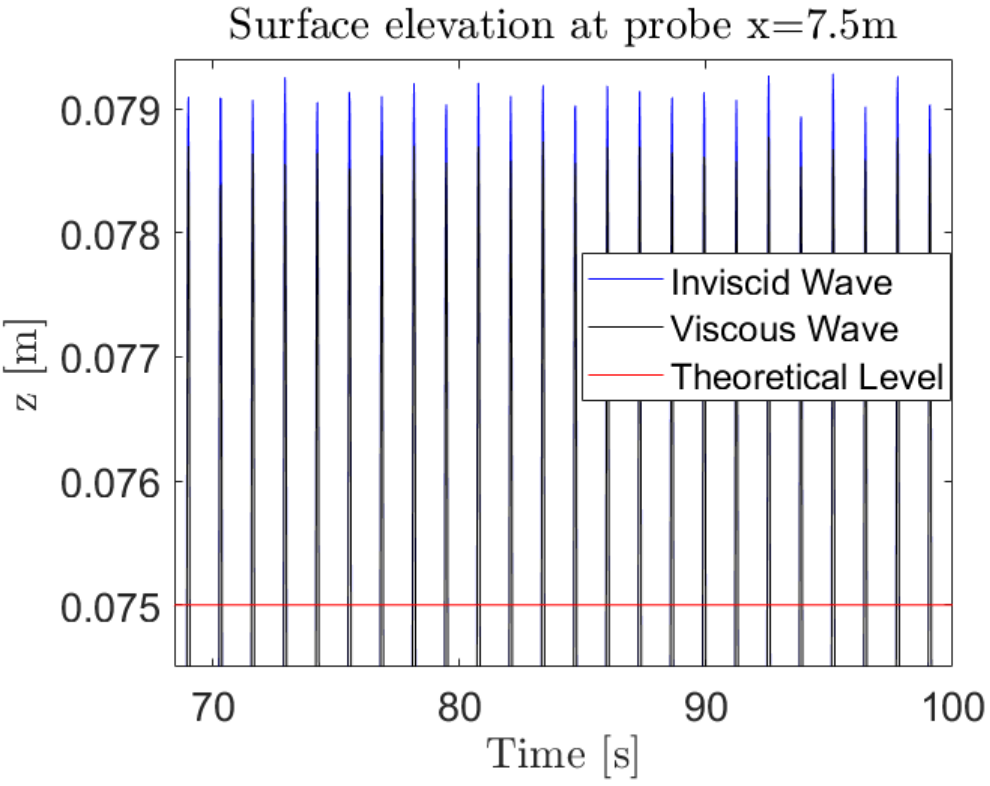

Figure 7.23: Maximum amplitude comparison for the surface elevation at y=6m, x=7.5m

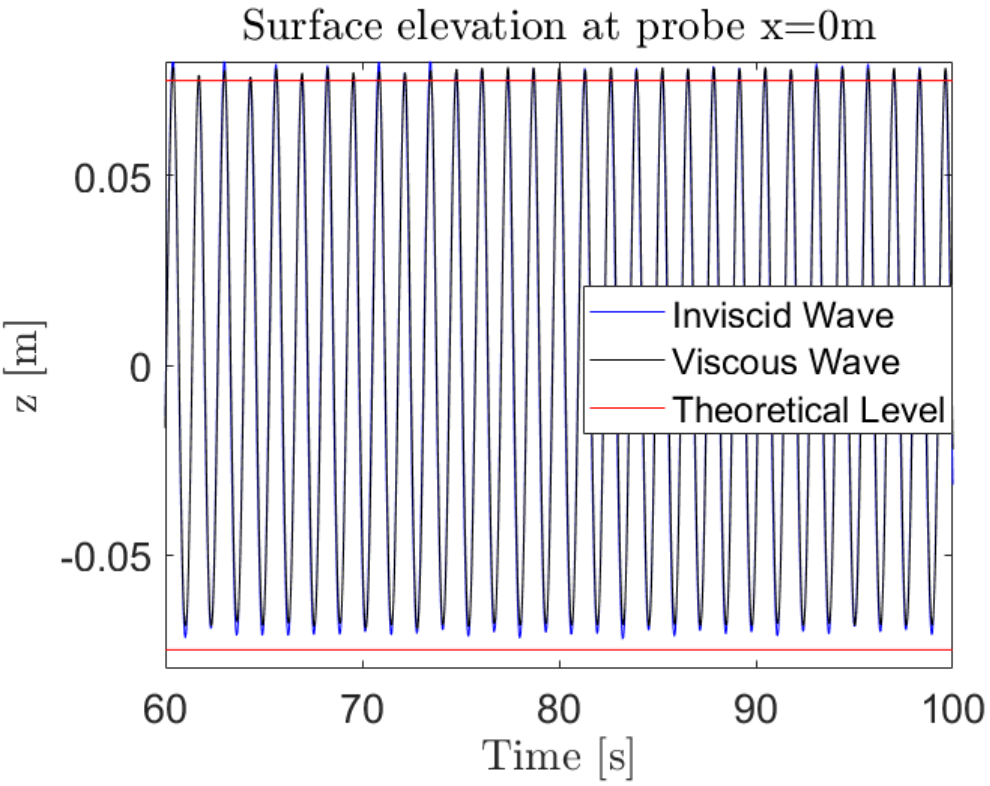

Figure 7.24: Result for wave probe at y=6m, x=0m

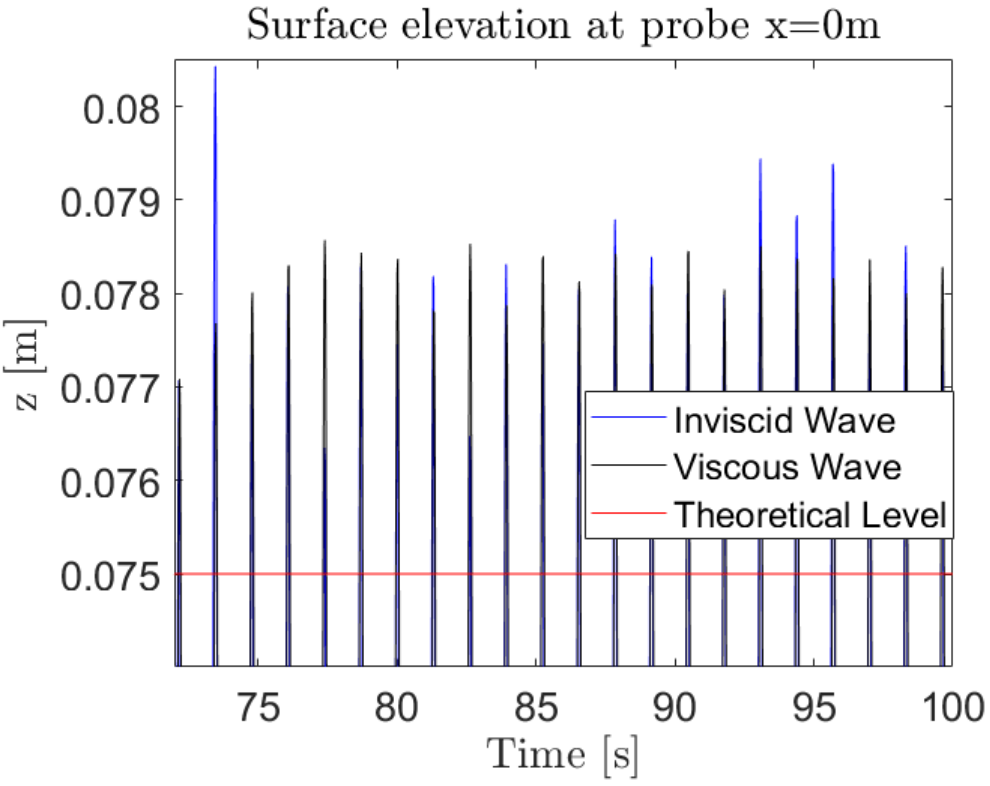

Figure 7.25: Maximum amplitude comparison for the surface elevation at y=6m, x=0m

Discussion

From table 7.6 one would be inclined to believe that the inviscid simulation is not a fitting method to compute the resistance of the vessel subjected to regular waves in head sea. An error estimate of nearly 27% is, of course, a glaring miscalculation of the resistance. However, as seen from figure 7.18, the inviscid agrees very well with the viscous simulation with regards to the pressure resistance. In fact, as the mean shear resistance is 15N, see figure B.2 in Appendix B, the inclusion of this value to the inviscid result would yield an E%D= 1.675. Therefore, while the inviscid simulation is not able to calculate an accurate estimate on its own, the calm water shear resistance could be added to render the inviscid simulation more accurate. The calm water shear resistance is equal to 14.22N, yielding an E%D=2.988 for the inviscid simulation. This indicates that added resistance simulations in head waves, can be accurately calculated by the inviscid simulation, if an accurate estimate for the shear resistance is present to supplement the inviscid calculations. As the $E\%D$ for the inviscid pressure resistance with respect to the viscous pressure resistance is only 2.42%, it is fair to assess that the added resistance in head-waves is a pressure-dominated system.

The main object of this thesis is to evaluate the applicability of a inviscid CFD solver to added resistance simulations. The goal is therefore to assess how much loss in pressure resistance the inviscid solver obtains from not including viscous forces. From figure 7.18 and 7.19 it would seem that this loss is non-existant. One would expect the viscous simulation to have the largest pressure values, so this would indicate erroneous results. From figure 7.18 it can be seen that the inviscid simulation agrees very well with the positive amplitudes of the viscous simulation, but estimates a slightly lower value for the negative amplitude. The relative difference is approximately 1.6% and 9.5% for the positive and negative amplitude, respectively. By looking at the wave elevation maximum amplitude plots, figures 7.21, 7.23 and 7.25, it is clearly visible that the inviscid simulation over-predicts the surface elevation compared to the viscous simulation. However, and even more importantly, it under-predicts the minimum amplitudes of the surface elevation by a larger margin than the over-estimate of the crest. This is why the amplitudes of the inviscid pressure resistance are larger than for the viscous, but its mean value is smaller. With an equal surface-elevation, the inviscid mean resistance would probably increase. The exact increase of the value is hard to say, but the value would probably become be closer to the viscous pressure resistance than what it is now. The problem needs to be solved by obtaining a more stable wave-model. However, as the pressure resistance is very much alike, a correct wave-model would not alter the result by much. To conclude that the inviscid simulation is not able to compute the pressure resistance correctly, would therefore be wrong.

The resistance of the RANS simulation agree very well with the 0th amplitude for resistance in comparison with the experimental results. As the amplitude-values from the wave-plots has an error of 3%-8% compared to theoretical values for the max amplitude and min amplitude respectively, the estimation could probably lessen with an increased accuracy of the wave-amplitude modelling. The 0th amplitude of the resistance is a very good estimate of the mean resistance, compared to the results of the participants of the 2010 Workshop, [Stern et al. 2014], but with a better realized free-surface the error will increase. However, the result should not rend the simulations nonphysical, as the wave amplitude only misses by $3\% - 8\%$ at the most, so the resistance should still be in the vicinity of the experimental result. It is also important to mention that the EFD result does not come from a perfect realized, regular wave with an amplitude of 7.5cm. They measured Hs= 13.8cm while having applied a nominal Hs= 15cm, [Larsson, Stern, and Visonneu 2010]. More knowledge about the values of min and max amplitudes is not published, and it is hard to make any further conclusion with regards to the accuracy of the wave modelling done in this thesis.

While the wave height seems to be around the theoretical value (3%-8% deviancy as mentioned) the wave seems to be unevenly distributed around the mean free-surface. A suspicion was that either the mean water-level was specified wrong in the wave-model option-tree, or the water density property in the wave-model was different than the one in the physics-continuum, and thus shifting the water-level. Both of these theories were checked, and both were set at the correct value. Exactly why the wave is unevenly distributed could be due to the parasitic currents, or it could be

due to a too coarse mesh. To see if the boundary conditions could infringe on the obtained free-surface, these were altered at the top, sides and bottom. Different conditions for each boundary were checked, but none gave a symmetric free-surface around the actual mean-free-surface. Doing a mesh-analysis could be beneficial, as the free-surface mesh is set at one of the more coarse, allowable settings. This should have been performed here, but a decrease in mesh-size would mean a smaller timestep, and there was not enough time to do this, as the result obtained here is acceptable. Another aspect that should be checked is the parameters for the Angle factor, in the HRIC scheme, the artificial viscosity to the momentum dissipation model, and the turbulence values. These values might have to be slightly adjusted in order to find the perfect set-up for this specific case.

The 1st order amplitude of the resistance deviates by a significant amount compared to the experimental results. As the 1st order amplitude of the Fourier transform refers to the linear term of the unsteady time history, it could be much more sensitive to small differences in set-up. For the experimental results, induced vibrations from the towing cart, and how the model is restricted to move in certain degrees of freedom, could have a large impact on the 1st order amplitude. The other participants from the workshop also achieved large underestimates of this value, so where the supposedly correct value of the amplitude should be, is hard to say. However, it is clear that the deviancy from experimental results does not indicate that the numerical set-up is wrong.

Results for the motions seem to point in the direction that the 6DOF solver, which calculates the motions on the vessel, solves the system with a satisfactory accuracy. However, as with the calm-water simulations, the 0th amplitude (mean) for the motions deviates more from the experimental results, than what the resistance estimate does. This is especially the case for the pitch-motion with the largest deviancy. The small values that are computed are partially to blame, as a small deviancy from the experimental results yields a large relative error in %. The motions do however agree more with the experimental values than what the calm water simulation does. This could be due to the overset mesh which handles motions better than what a standard mesh set-up does. It is peculiar that the 1st amplitude values for both of the motion variables are considerably poorer than what the participants of the workshop managed to obtain. However it is hard to read too much from this, as none of the participants achieved consistently small E%D values for all of the motion-variables. In fact, the results obtained in this thesis have the third lowest mean error for motions, for both 0th and 1st amplitude-values, and has the lowest mean error when only 0th amplitude value is used. It also has the most consistent result, indicating a better stability. Another good indication of stability is the good agreement between the viscous and inviscid simulation with regards to the motions. The computed values are almost identical. If the simulations were set up correctly this was expected, as the heave and pitch motions are pressure-dominated, so the viscous solver should not alter the final result too much. This has been the case for this simulation, and contributes to the validation of the results.

As with the argument made in the previous paragraph, the 1st order harmonic amplitude values do not by themselves indicate a non-physical numerical simulation. Due to the accuracy of the mean estimates of the variables, the motions are considered accurately modelled. However, how the system reacts when more complex motions are present is hard to say. Therefore, steps should be taken to decrease this potential error for the oblique simulations. These simulations will experience more complex motions than the present simulations, and the motions should be more carefully modelled. In the solver there is an option to increase the number of inner 6-DOF iterations. This option controls the number of iteration the motion solver is allowed to do before continuing on to the next outer iteration. Increasing this number could lead to more accurate results for the motions. Of course a finer mesh with a coherently fine time-step could also be beneficial for the motion-calculations, but to check this a mesh-convergence study would have to be done. This simulation was conducted with a already very fine mesh in order to assure valid results on the first run due to time-limitations. The results are already very good, so a mesh convergence study would probably point towards decreasing the mesh count for a more efficient simulation.

As the velocity of the vessel is modelled by a current and wind in the VOF-wave model, inaccuracies could stem from this type of modelling. If the water particles in the current and the wave front interact, causing the flow to achieve an intermediate velocity between the two, a doppler-effect on

the wave-front might occur and can interfere with the results. This was checked by computing the theoretical period of encounter for the wave, by the use of equation 7.10, obtained through using equations from [Pettersen 2007], and comparing it to the time series of the resistance. The resistance amplitudes should oscillate with the period of encounter. Equation 7.10 is valid for deep waters, in other words when $h > \frac{\lambda}{2}$ [Pettersen 2007], which this is. Several wave-tops were used from different areas in the time-domain that has been used to compute the final results, and the encounter period of the waves was 1.308s. The theoretical value was computed to be 1.311s, so upon this it is reasonable to conclude that the doppler-effect from this type of ship-velocity modelling is negligible.

$$T_e = \frac{2\pi}{\sqrt{kg} + kU} \tag{7.10}$$

Throughout the head-waves study, it became apparent that the CFL-condition should not be violated when the simulations involved waves. The simulations shown in this section had a time-step equal to 0.004s, yielding a CFL number of 0.54 for the smallest cell. As mentioned earlier, $CFL > 0.5$ could yield numerical inaccuracies, [Böhm and Graf 2014], so a time-step test was conducted with a time-step of 0.003s, which would yield a CFL number of 0.4. The results did not give a better modelled free-surface, and as such the time-step of 0.004 was deemed fine enough. The problem with the inaccuracy of the wave-amplitude modelling is probably connected to the mesh-size. As with the calm-water simulations, the cell-size needs to reflect the magnitude of accuracy it is supposed to measure. In this case, the error is around 3-4mm, and with a cell-size of 1.25cm, this level of error should not come as a surprise. The wave-height is measured accurately, but the min and max levels are not. However, the error this introduces to the final result compared to the significant increase in cells, points towards the conclusion that an increase in cell-count should not be performed.

The cell-count in these simulations are far higher than a lot of other published works on regular wave seakeeping analyses that has achieved satisfying results. While the free-surface has been modelled as accordingly to ITTC guidance, and other publicized works, there could be an argument made that it is possible to decrease the total number of cells without compromising the results. This could either be achieved by a domain analysis or a grid-convergence study. Had there been enough time, this would have been done, as it would surely have helped in the time-efficiency of the upcoming oblique-wave simulations. However, as time has been a scarce resource throughout the work on this thesis, there was simply not time to perform these tests. Therefore the current set-up is deemed as stable and accurate, albeit with an asymmetric surface-elevation, and is therefore used for the oblique-sea simulations.

7.3 Oblique Wave Simulations

While the wave-set-up from the regular waves could be implemented easily into the oblique simulations, there were some important changes that had to be made. The biggest one was to decide how to model the flow. As the head-waves has the benefit from having the waves and current going in the same direction, the boundaries can more easily be specified, and the numerical set-up is more intuitive.

The wave-angle chosen is 20°, due to the fact that one of the few sources found indicates that there is a higher added resistance in waves for this heading than for head-waves. Therefore, if the obtained results were to show this trend, the results would be more validated.

Set-up

The first problem was to decide how to model the vessel velocity. As mesh-generation and domain set-up are dependent on the modelling of the propagation of the vessel, this was the first thing to

look at. At first, a set-up where the outer domain was rotated 20° relative to the vessel orientation, while keeping the overset (inner) domain oriented with the vessel. This distorted the overlap mesh-region between the two meshes, making it hard to believe that accurate cell-communication could be achieved. The waves are demanded by the VOF model to be sent from one inlet and directly towards a pressure outlet boundary oriented perpendicularly to the wave-propagation direction. Therefore the outer domain and the inner domain were oriented the same way, while the vessel was oriented 20°.

The velocity of the vessel was modelled by having a current, and wind propagating in the opposite direction of the vessel orientation, while the vessel was restricted to move in any direction, apart from heave, pitch and roll. This was seen as both the easiest way to model the problem, and the most consistent compared to the set-up for the regular waves. Some information will be lost with this set-up, such as the coupled motions with the other degrees of freedom, but for the purpose of this thesis, it is deemed as a good enough approximation. Due to having an oblique current relative to the domain orientation, inlet conditions had to be used at the sides of the domain. Naturally this also applied to the side that was denoted as the "symmetry plane" in the regular waves. Due to an obliquely oriented ship, there would be no symmetry-plane and therefore flow calculations had to done over the entire domain.

The free-surface grid-realization was the same as the one used for the regular waves. While this is good enough to represent the waves, and the resulting wake of the ship, the overset mesh interface has to be given some attention. Due to the obliquely oriented ship, there exists a roll motion induced on the vessel, and as the overset mesh topology moves with the body, different, and maybe even larger, motions occur for this condition. This resulted in a crash of the simulation, due to fact that the inner domain moved too far. This shifted the inactive cells to where there should be active ones and yielding too few interpolation cells for the donor cells to communicate with. When the mesh is very fine at one point, but becomes significantly larger not too far away this can occur. To remedy this, the three volume controls for the mesh in the free-surface were increased in their vertical direction. This naturally resulted in an increase in the cell count, but now the overset mesh interface was able to move and still have a valid interface. Another reason why this has happened to the oblique simulations, and not the regular wave-simulations is that the overset mesh interface is smaller for the regular wave-simulation. Since the vessel and overset mesh are, for the regular waves, oriented the same way a much smaller domain can be used to encapsulate the entire body. When the vessel has a different orientation than the overset mesh, there are large parts of the prism-box used to make the overset mesh that winds up being far away from the center of gravity of the vessel. The resulting mesh interface for the free-surface can be viewed in figure 7.26, and the overset mesh interface with the vessel inside can be viewed in figure 7.27, where the overset mesh is colored in pink. The inner domain could probably have been reduced and thus given a more stable overset mesh communication, but due to the slow growth of the mesh cells, this was not done. A slow growth rate for the cells ensures that no abrupt change in cell-size occurs, which could have been fatal for these types of simulations, for a number of reasons, such as flow reflection, lack of interpolation cell in the overlap interface, and general smearing of the free-surface. The slow cell growth rate is necessary to have for these simulations, and it was found that the current inner domain aligned well with neighbouring cells.

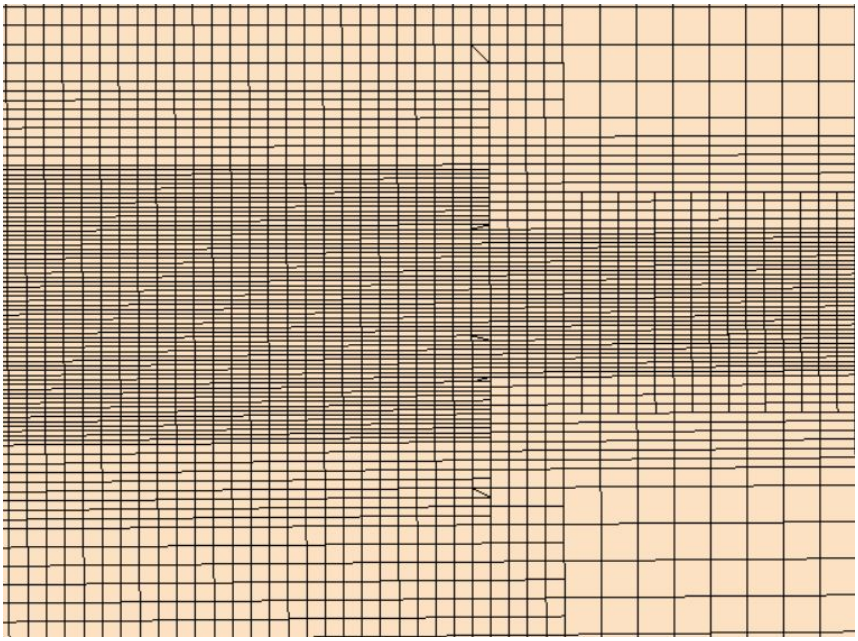

Figure 7.26: Increase of free-surface mesh interphase in the inner domain, oblique wave simulation

Figure 7.27: Size of the inner domain with the obliquely oriented vesse, oblique wave simulation

Results

The results from the viscous and inviscid oblique simulations can be viewed in table 7.7. Naturally, only the pressure resistance is compared, and the relative error is the deviancy of the inviscid result, compared to the viscous result. In figure 7.28 the inviscid and total pressure resistance is shown. As with the head-wave simulation, the inviscid simulation seems to over-estimate the amplitudes of the resistance.

In figures 7.30-7.33 the frequency spectra of the monitored parameters can be seen. These shows one of the main advantages the inviscid CFD simulations have over the potential theory simulations, namely, able to compute higher-order terms. The rest of the plots and results from the simulations can be seen in Appendix C.

Table 7.7: Oblique simulation results

	0th Amplitude	1st Amplitude
$R_{P,Viscous}$ [N]	57.822	100.163
$R_{P,Inviscid}$ [N]	60.370	111.746
$E\%D$	-4.400	-11.564
$\eta_{3,Viscous}$ [m]	0.1659	0.030
$\eta_{3,Inviscid}$ [m]	0.166	0.032
$E\%D$	-0.060	-6.667
$\eta_{4,Viscous}$ [deg]	0.378	0.080
$\eta_{4,Inviscid}$ [deg]	0.358	0.089
$E\%D$	5.290	-11.250
$\eta_{5,Viscous}$ [deg]	0.252	2.339
$\eta_{5,Inviscid}$ [deg]	0.282	2.420
$E\%D$	-11.904	-3.463

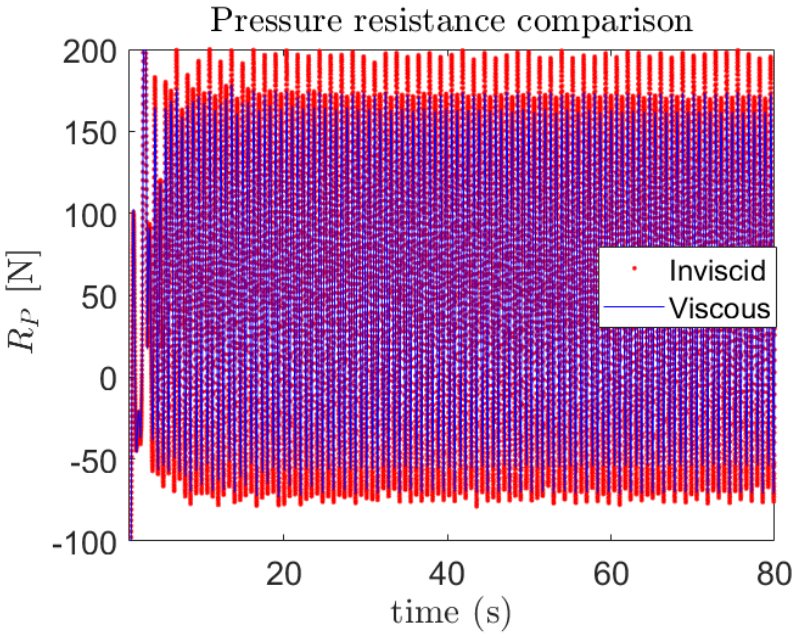

Figure 7.28: Pressure resistance comparison, oblique wave simulation

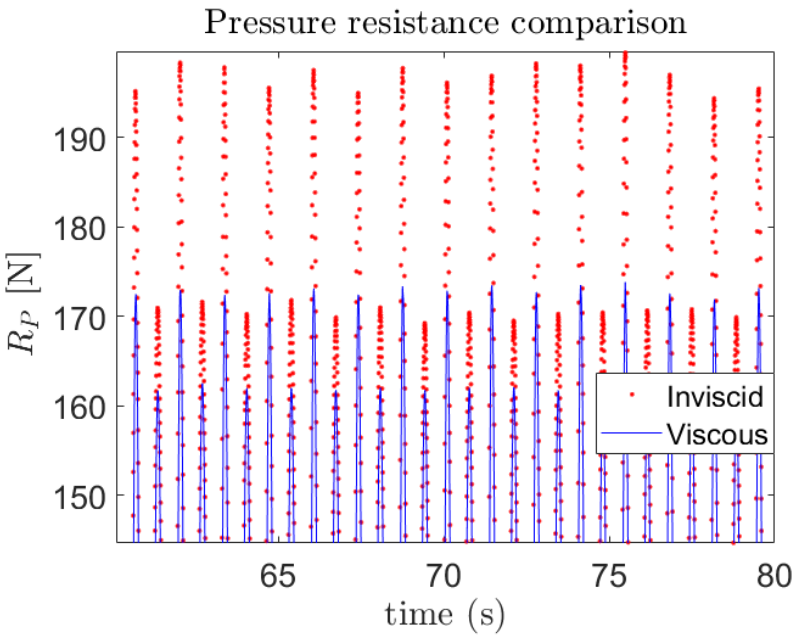

Figure 7.29: Maximum amplitude comparison of pressure resistance, oblique wave simulation

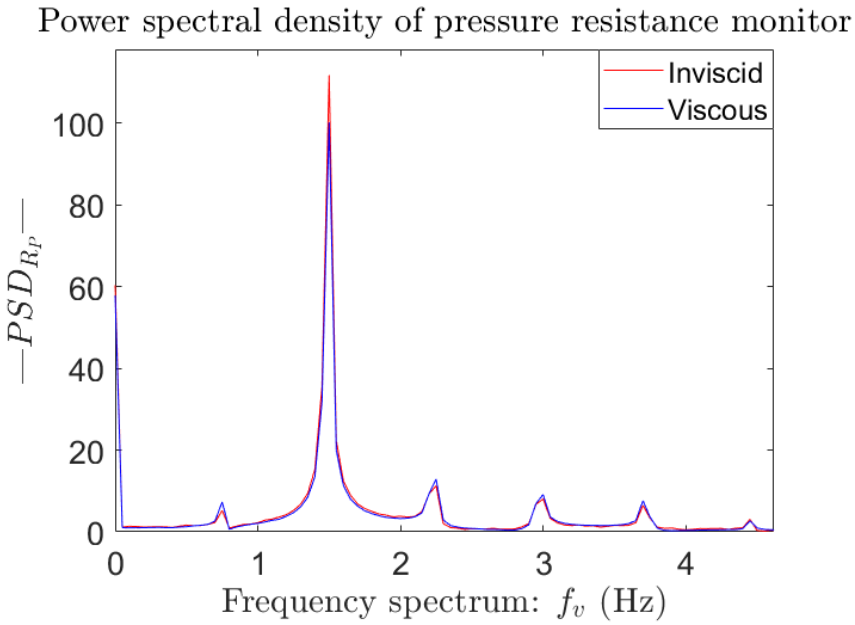

Figure 7.30: Power density spectrum of the pressure resistance

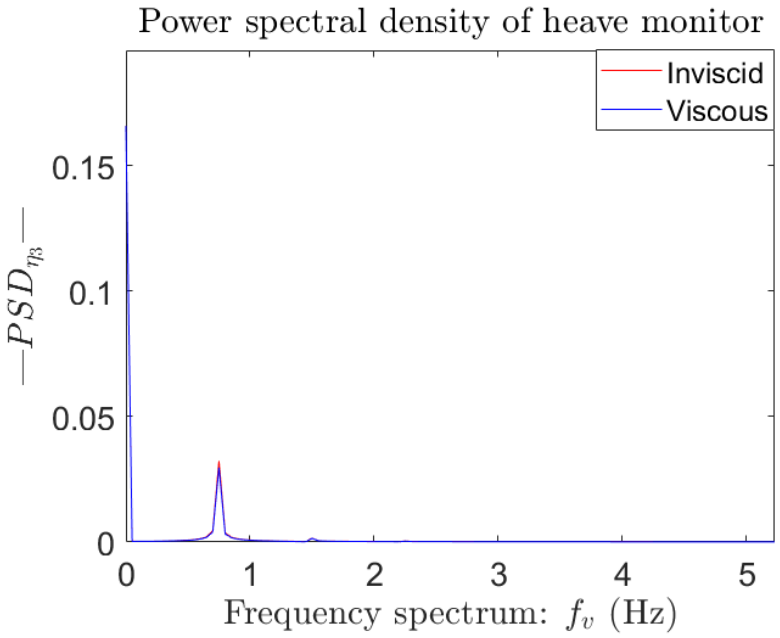

Figure 7.31: Power density spectrum of the sinkage

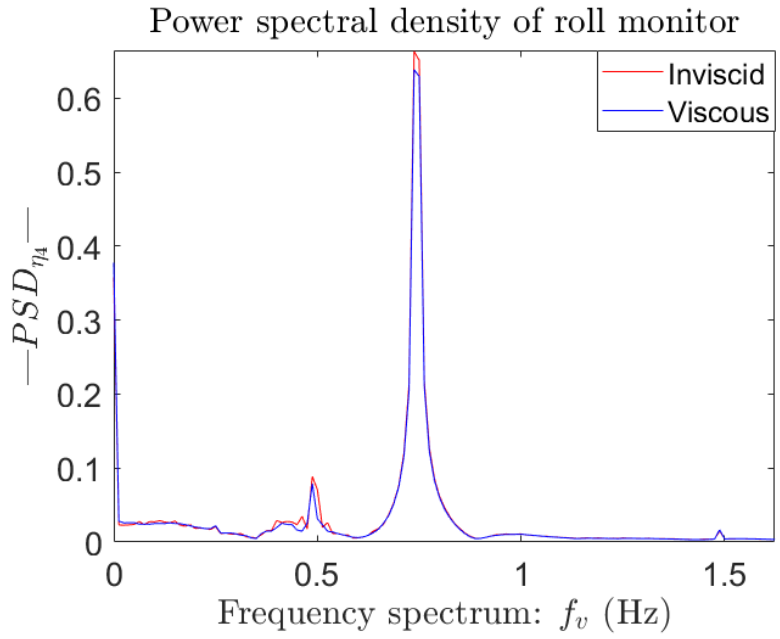

Figure 7.32: Power density spectrum of the roll motion

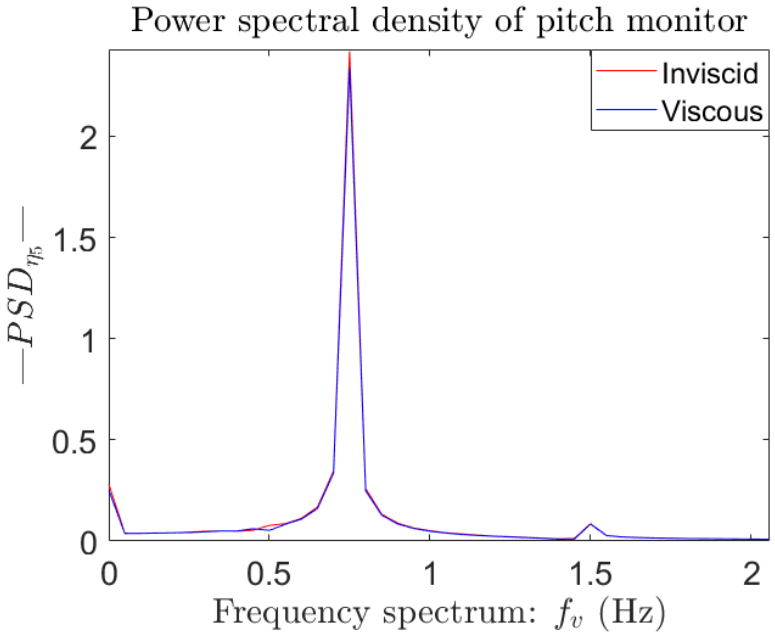

Figure 7.33: Power density spectrum of the trim

Discussion

Due to the lack of experimental results for the oblique wave conditions, it is important to assess whether or not these results are realistic. The overall agreement between the two simulations indicates a stable numerical scheme. In addition, the total resistance has a value of 67.64N, which is 8.14N higher than the head-wave condition. This corresponds well with the remarks from Volker and Couser, who states that incoming waves at 10°-20° yields the highest resistance, [Volker and Couser 2014]. Otherwise, in figures C.12-C.16 the wave-elevation plots can be seen for the two simulations. The waves are stable in front of the vessel, but from figure C.17 it is noticeable that the inviscid simulation is not able to model a stable free-surface. This was also present for the head-wave simulation, but as the simulation was allowed to continue to 100s, this error was diminished. This could indicate that the inviscid solver needs a longer time to achieve a stable free-surface which diminishes its computational efficiency compared to the viscous simulation. Having the oblique simulation running up to 100s was not possible for this simulation, due to time-limitations, but from the head-wave results it is visible that this time-increase does not alter the results with any substantial amount. In figure C.18 the contour plot for the free-surface is included, and this yields no reason to doubt the results, as there are no inaccuracies, or errors with the free-surface.

What is interesting, is that the max amplitudes for the total resistance is lower than the head-wave simulation. Since the max amplitude is lower and the min amplitude is higher, the average resistance becomes higher. As the reference literature found for this thesis does not go into detail with regards to the oscillation of the resistance, it is hard to conclude anything. However, one would be inclined to believe that with the vessel oriented 20° to the incoming waves, the frontal area of the vessel that the wave hits should be bigger than in head-waves. A larger frontal area should imply a larger pressure, and thus a larger resistance amplitude. This effect might be reduced since the vessel is rather full-bodied. A more slender vessel might experience this, as the bow would cut the wave, rather than push through it as this tanker does. In addition, with the vessel obliquely oriented, its length in the wave-direction is 5.18m. This results in the wavelength having a relative size of 0.9768, instead of the original scale of 0.9171. At such wavelengths, the resistance is very dependent on the relative length of the wave compared to the vessel, as seen by figure 3.1. The higher amplitudes in head-waves could be explained by the fact that the relative wave length is closer to the resonance peak than what it is in the oblique condition. The period of encounter is also altered, since the ship now traverses with an angle relative to the wave-heading, resulting in a lower ship-velocity in the wave-parallel direction. As seen from 3.1, this could have a large impact on the resistance.

From figure C.1 one can see that the resistance has an "extra" positive amplitude of the resistance oscillating with almost half of the encounter frequency. This is due to the orientation of the vessel, since the highest peaks are when the wave hits the bow of the vessel, and these oscillates with the encounter frequency. The smaller amplitudes occur when the wave hits the aft part of the body which has not been hit by the wave. Consequently, the energy of the PSD-spectra for the pressure resistance is shifted to almost 1.5Hz, which is twice the value of the incoming wave frequency. Naturally, this means that the resonance area is shifted for oblique-conditions compared to head-wave conditions. With this extra positive amplitude, the negative resistance amplitude is reduced, and consequently the mean resistance is increased.

As with the head-wave simulation, the waves modelled are asymmetric around the mean-free-surface. This can be seen in figures C.12-C.17 in Appendix C. Another similarity is that the inviscid simulation estimates a higher pressure resistance than the viscous solver. As with the head-wave condition, the inviscid solver has higher wave-crests, and lower wave-troughs, leading to higher absolute values for the pressure-resistance amplitudes. Since the inviscid simulation struggles with the resistance amplitudes where the wave hits the bow of the vessel, it becomes more credible that these over-estimations are related to the erroneous wave-modelling. While the inviscid and viscous simulation has an identical surface-elevation for wave-probe x=11m, they deviate, albeit marginally, at probe x=7.5. This is a better agreement than what the head-wave simulations are able to get. However, as the wave-modelling worsens over the length of the vessel, resulting in what is measured at wave-probe x=0m, the only conclusion is that the oblique simulation has the same

error as the head-wave simulation. Since this error is consistent for both of the wave-conditions it is still possible to compare them to one-another. However, a thorough parameter-analysis with the respect to the wave-modelling should be conducted.

C. Liu et al. presented a paper focusing on mean wave forces and motions on the DTC vessel, computed by a CFD solver, in oblique wave conditions. They reported increased values for trim and sinkage as the wave-angle got larger (0° being head-waves), [C. Liu et al. 2018]. This trend is also visible from comparing table 7.6 and 7.7. As this trend is captured by the simulations, it indicates that these results are correct. The DTC ship is of similar size as the KVLCC2, but it is longer and more slender. This will influence the results, naturally, but the trends witnessed by these results, are comparable. However, without any sources that are directly comparative to the simulations done here, it is impossible to be completely certain that these results are in fact correct. While there are many elements that points towards such a conclusion, none can validate the simulations completely. However, the results are deemed good enough to use them for the evaluation of the applicability of the inviscid CFD solver. While experimental results are needed to be conclusive, these results can be used as a starting point for further analysis. The experimental results for the DTC vessel stem from the OMAE conference in 2016, [Sprenger et al. 2016]. Experimental seakeeping tests for the KVLCC2 is also present in this conference paper. The author was not able to require the raw data, but when these results are made available it will be much easier to validate oblique added resistance simulations.

The inviscid simulation holds up very well compared to the viscous simulation, albeit with a surprisingly large relative deviancy for the trim. If one is to assume that the viscous simulation has the same level of precision as the head-wave simulation had with its experimental counter-part, the inviscid simulation achieves a high level of accuracy, on par with the 2010 Workshop results. This is only speculation, since there are no experimental results to compare with, but as reasoned above, there are no serious indications of non-physical results.

While the agreement on the pressure resistance is well and good, it is also very important that the frictional resistance resembles the calm water frictional resistance. Adding the calm water frictional resistance to the inviscid pressure resistance, yields a total resistance of 74.59N. Compared to the total resistance from the viscous simulation, this is an overestimate of 10.27%. The frictional resistance in the oblique condition is approximately 70% of the calm water frictional resistance. This is a severe drop in equality, compared to the value from the head-wave simulation. It is expected that the frictional resistance would change with respect to change in wave heading. However, if the trend continues, using the calm water frictional resistance as an estimate would not be good enough. If the inviscid simulations are to be used with success, the frictional resistance needs to be better accounted for than what the calm-water estimate achieves.

The computed values for the heave motion are very consistent, between the viscous and inviscid simulation. This was expected, as the heave motion of a vessel is pre-dominantly a pressure-related phenomenon. It is also a very linear term, which is why potential theory methods have such a success with computing them. However, as with all the motions computed, it over- and under-estimates the max and min amplitudes respectively. This is connected to the deviation of the 1st order harmonic amplitude of the Fourier transform. As the min and max amplitude deviates with the same magnitude, the mean estimate becomes equal to that of the viscous simulation. However it was expected that the agreement between the two estimates would be less, due to the difference in the free-surface modelling. It would appear that the heave-motions is not as sensitive as the resistance and the other motions to the wave-amplitude. This could be connected to the linearity of the motion, as the other parameters have much higher values for the higher order harmonic amplitudes.

There is a surprising amount of agreement between the two simulations with regards to the roll motion. The overall difference is 5.29%, for the 0th amplitude, suggesting that the roll motion, for this angle, is a pressure dominated motion. From figure 7.32 it is visible that the inviscid simulation accurately computes the phases of the different harmonic amplitudes. With an incoming angle in the area of $45° - 90°$, the dependency of the roll motion to viscous forces should be much higher, and it is reasonable to assume that the inviscid simulation would have more trouble modelling this

motion under such conditions. Still, the inviscid simulation is able to model the roll motion with a good accuracy, and it would be very interesting to see how large the interval of wave-heading angles is for accurate, inviscid, computation of the roll motion. In addition, the non-linearity of the motion is clearly visible from figure 7.32, so both of the solvers would most likely outperform any PF-solver in regards to roll-motion calculations. It is worth mentioning that from figure C.6, the values of the roll motion seems to have converged around 55s. The small oscillations are expected due to non-linear effects, but with the values so recently converged it is possible that the roll-motion is not finished converging. Either running the simulation for a longer period, or increasing the number of inner iterations of the 6DOF-solver might have proven beneficiary for the roll-calculation.

It is surprising that the level of inaccuracy of the trim is as high as it is. From figure 7.33 the higher-order dependency of the pitch motion is very visible. It would seem that there is a higher level of dependency on viscous forces than what was first assumed. However, it is important to notice the small values that are being computed, and therefore while the actual difference in values is only $0.03°$, the difference almost becomes 12%. Therefore, as was argued in the case of the calm-water and partially head-wave condition, the result is deemed as within the acceptable limit of accuracy.

Under realistic conditions this sea-condition would induce a more complex motion on the vessel than what is modelled here. Sway and yaw motions would be present, and these would yield coupled motions with the already present motions. This could increase the viscous presence in the physical phenomenon occurring, making the inviscid solver less applicable. To model the realistic motions, a maneuvering function would have to be present, or even better, a rudder would have to be modelled with a steering-function, and the steering force would be directly computed by the lift on the rudder. To model to a propulsive force on the vessel, and have the domain move with it would be even more realistic. However, this would significantly increase the computational time, and the gain in realism compared to this increase would not be justifiable with the types of simulations done here. The coupling of motions would give different values for the computed amplitudes, but as the purpose of these simulations is to model the forces and motions in regular waves, and thus achieving quasi-steady, comparable results, this type of realism is deemed non-important.

From figure C.18 the asymmetric wake is clearly visible. As are the wave-forcing models implemented at the boundaries. It is important that the wave-forcing is implemented far enough from the ship, so that it does not interfere with the wake-flow, as the obtained result is dependent on it. This should have been checked by commencing a domain-analysis, but due to time-limitations it was not.

The over-all agreement between the two simulations points towards the conclusion that the added resistance in waves is a pressure-dominated phenomenon. This is also true for the motions occurring, as witnessed by the roll-motion. However, the frictional resistance does oscillate with the encounter frequency, so the added resistance in waves is also affected by viscous forces. This effect is large enough to render the calm-water frictional resistance estimate as insufficient for oblique conditions. While more simulations and experimental results are needed to obtain anything conclusive, the results here has given a good indication in regards to the applicability of the inviscid solver. A better free-surface modelling, and parametric analyses in regards to the simulation length, mesh cell-count, 6DOF iterations could all help in giving the obtained results more validity and could have given a more efficient simulation. Due to time-limitations this was not possible, as the initial simulations had to be used to make the overset-mesh function properly.

Chapter 8

Discussion

As the inviscid simulation does not compute the viscous forces, its applicability needs to be assessed on the basis of including an accurate estimate of the frictional force. This estimate would also need to be a valid substitute for the actual frictional resistance in oblique conditions. In addition, the inviscid simulations would have to offer a substantial decrease in computational time compared to viscous simulations, because if this is not the case then there is no point in going for a less accurate solver. Also, there is the element of how well it manages to estimate the seakeeping parameters of interest. This chapter will try to shed some light on these topics, and will try to make the case whether or not the inviscid solver is a good option.

With regards to the frictional resistance, it is evident from the oblique wave simulation that the frictional resistance varies substantially from the calm-water condition. With the oblique frictional resistance being approximately 30% lower than the calm water friction, it is not valid to use the calm water frictional resistance as an estimate. Even by decomposing the frictional force with the cosine of the wave angle, the difference is still at 20%. How large the difference would be with different wave-angles, is difficult to say, but it is naive to assume that they would be closer to the calm water estimate. Other, more accurate, estimates for the frictional resistance need to be applied, and they need to be semi-accurate for multiple sea-conditions. The results obtained in this thesis points towards the conclusion that the calm water frictional resistance can be used as an estimate in head-waves, but not for oblique conditions.

To obtain a comparative database on the computational time, the viscous and inviscid simulations were completed with the same number of cores. The number of cores varied with each condition that was tested, but at each condition the number was the same for the inviscid and viscous simulations. A time efficiency factor was computed, showing the factor of how much faster the inviscid simulation was than the viscous. The result can be seen in figure 8.1. It is clearly visible how much more faster the inviscid simulation is for the calm water condition. This is most likely due to the fact that the viscous simulation must solve the two-equation turbulence model, and the boundary layer mesh makes up a larger part of the total cell-count than what it does for the other two conditions. However, the drop in efficiency is substantial when waves and the overset mesh are included. While the inviscid head wave simulation reduces computational time by 30%, it is far from the efficiency obtained for the calm water condition. At every iteration the overset mesh needs to interpolate values between the inner and outer domain, and this probably reduces the inviscid efficiency. For every additional model and time-demanding process that the inviscid and viscous simulation have in common, the smaller the overall gain in efficiency from the turbulence exclusion becomes. The wave simulations have more complex motions to solve than the calm water simulation. For the calm water simulation, the 6DOF solver is pre-emptively requested to iterate towards a state of equilibrium. For the wave simulation, this is not possible as the simulation does not approach a steady-state, and therefore the model is set to free-motion. It is surprising that the oblique condition experiences a larger time-efficiency for the inviscid simulation than the head-wave simulation. The only difference is that the oblique condition has more complex motions and a bigger overset mesh area where it has to interpolate values. One would therefore expect it

to be either as efficient or more inefficient than the head-wave condition. However, some problems occurred with the computer used during this thesis, which have affected this analysis. Occasionally, some of the parallel processors would keep working after a simulation was completed. This bled into the next simulation as the communication between the processors were diminished and thus yielding a longer computational time. This was observed during this analysis, actually making the computational time for the same analysis twice as big. The author was not aware of this error at the time of the head-wave simulations, so it is possible that the efficiency of the inviscid simulation would be larger than what is shown in figure 8.1. However, this was checked for the oblique condition, and with the error present, the inviscid and viscous simulations were equal in computational time. Without the error, the inviscid simulation was more efficient than the viscous solver, by a factor of 1.5. So even with the computer running at its highest potential, for both cases, the efficiency will not reach the levels of the calm-water condition. The trend of computational efficiency is alarming, and in order to regard the inviscid solver applicable for seakeeping-analyses, it should have a higher computational efficiency for wave-simulations than what it has.

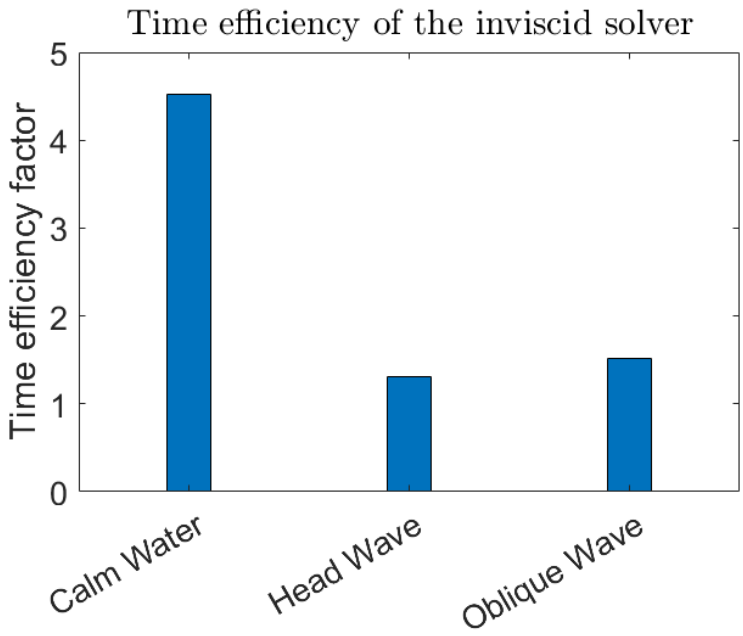

Figure 8.1: Time efficiency of the inviscid simulation compared to the viscous simulation

It was evident that, while pressure resistance was influenced by viscous forces, the measured seakeeping parameters were pressure dominated. The results were similar, but due to the incoherency of the wave modelling, an exact conclusion on the subject is difficult to make. If the surface-elevation were equal for the inviscid and viscous simulation it is highly likely that the inviscid simulation would yield a lower pressure resistance, than the viscous but not by a significant amount. The waves were similar enough to make the argument that the added resistance in waves is a pressure dominated system. Even the roll motion was accurately modelled by the inviscid solver. Its ability to precisely compute this motion will probably lessen as the wave angle becomes larger. This needs to be checked, but the results obtained here indicate that the inviscid solver is able to calculate the forces and motions the vessel experiences both in head waves, and oblique waves.

With no experimental results for the oblique condition, it is impossible to conclude anything with respect to the validity of the oblique simulations. However, the results seem to be realistic, based on the results from the head-wave simulations, and the results can therefore be seen as a good starting point for further research. While the gain in computational efficiency is small for inviscid wave-simulations, their accuracy seems fairly good, as they achieve the same level of accuracy as some viscous solvers do. Due to time-limitations there was simply not enough time to try to optimize the computational time and the over-all performance of the simulations. A better

numerical set-up which would yield a greater efficiency for the inviscid solver is probably possible to achieve. However it is unrealistic to think that the computational efficiency can be doubled for the wave-conditions, and that is probably the level of efficiency it needs to be deemed as applicable.

For the inviscid solver to be useful, it needs to be able to produce accurate results for a large variety of vessels. It is probable that a smaller vessel with larger relative motions could prove a difficult case, as viscous damping could play a larger role. The larger motions themselves would not necessarily pose a problem to the solver, as the overset mesh technique seemed very capable to monitor large motions. The KVLCC2 is a very large ship, so the frictional resistance is a large part of the total resistance, at least in calm waters. A smaller ship, with less influence of the frictional resistance, could give better results in the oblique-wave conditions, as it wouldn't be as dependent on a good frictional resistance-estimate. Of course any viscous flow-generating appendages, such as bilge keels, would render the inviscid solver more inaccurate, but apart from that it seems able to capture the seakeeping environment. The over-all pressure-dominance of these analyses are evident, and the inviscid solver would probably be able to handle most vessels with the same level of accuracy, as obtained in this thesis. Of course without a good estimate for the frictional resistance, it seems to be in-applicable for the large tankers. As most other ships are smaller than a VLCC, it would seem that the inviscid solver could be very useful for many ship-types. This needs to be checked, and different wave-headings need to be analyzed to see their viscous dependence. On the basis of what was obtained in this thesis, there is no indication that the inviscid solver would not be able to handle different vessel-types.

In chapter 3 it was described how dependent the added resistance in waves is on the characteristics of the incoming wave. The chosen wave-model in this thesis represents a long wave, with a relative length that puts the vessel in the resonance-motion area of figure 3.1. This could have introduced challenges to the inviscid solver by the large motions occurring, as viscous damping could have been a large contributor to the resulting motions. However, this was not the case, at least not for the two wave-conditions present in this thesis, so it would seem that long waves do not pose a problem for the inviscid solver. Short-waves, however, could infringe upon the accuracy of the inviscid solver. This is because the forces occurring are mainly caused by diffraction of the incoming wave, by the ship, and not induced motions from the radiated wave. These wave-conditions could be dependent on viscous forces, and this should be further analyzed. It has been reported that the added-resistance accuracy for both PF and viscous CFD, in short waves, are dependent on the steepness of the wave, [Sigmund and El Moctar 2018]. As discussed in the result chapter, the steepness of the wave is a very important factor when it comes to the mesh-generation of the free-surface. [Söding and Shigunov 2015] reported that added-resistance in waves were not accurately calculated by RANS-, Euler- or PF-methods, for short waves, $\lambda < \frac{L_{PP}}{2}$. Since both the viscous and the inviscid solver proved to be inaccurate, the problem could reside in a poorly free-surface mesh. If this is the case, the mesh-set-up shown in this thesis could prove to solve this problem as it takes the characteristics of the wave into account. There is sufficient reason to believe that, with a better gridding of the free-surface, the viscous solver would improve for short-wave simulations. Whether or not the inviscid solver would obtain an improved accuracy, should be checked.

Chapter 9

Conclusion

The goal of this thesis was to assess the applicability of the inviscid solver to wave simulations, both in head waves and oblique waves. Acceptable concurrence was found between the experimental results and the inviscid simulation in head waves, with the calm water frictional resistance used as an estimate for the shear force. The result from the oblique simulation indicates that the inviscid solver was able to compute the pressure resistance and motions to a satisfactory level of accuracy. However, as the frictional resistance differed substantially between the calm water resistance and the oblique resistance, the inviscid solver would still be inaccurate. In addition, for the two wave-conditions, the gain in computational efficiency was severely diminished compared to the calm-water condition. Thus, without an accurate estimate for the frictional resistance for any wave-heading angle and a profound increase in computational efficiency, the inviscid solver is not applicable for oblique seakeeping analysis. Further research is needed to confirm these results, but this thesis is regarded as a good starting point for further analysis.

Chapter 10

Suggestion for Further Work

While the work done in this thesis gave good indications of the applicability of the inviscid CFD solver, there is still a lot of work to do, before drawing any conclusion with regards to its usefulness. This is also closely connected to the wave-modelling as this is an area a lot of solvers are struggling with.

First of all, testing for one oblique condition is not enough, and a more extensive research with wave-orientation should be conducted. For instance, it would be interesting to see what the results would be when the waves hits the vessel at an angle close to 90°, as this is a condition which is supposedly more viscous-dominated. Of course, a ship would, if possible, avoid such a heading, but the tests could give useful information as an extreme-condition test. In addition, following waves are very much of interest, as this is a condition with which not a lot of numerical research has been conducted.

The oblique simulations were very time-consuming, and could benefit from being made more efficient. Doing domain tests for different oblique conditions to find out how large the domain has to be, and how far away the wave forcing needs to be is interesting. Here, only one condition was tested, and it is hard to say whether the domain could have been shrunk, or if it had to be increased. Setting up a practice for how large the domain and the wave forcing needs to be with respect to how the vessel is oriented, would help with the future efficiency of such seakeeping analyses.

A recurring problem for the wave-simulations done in this thesis, has been the wave-modelling. While the free-surface became much more stable after a lot of changes was implemented to the wave modelling and solver, the result is still asymmetric. Finding out why this is the case and then establishing a good way to model an arbitrary wave, with the grid-discretization and solver set-up that follows, would be very beneficiary for further research.

[Söding and Shigunov 2015] concluded that the added resistance in waves were not accurately computed by RANS-, Euler- or potential methods for $\lambda < \frac{L}{2}$. Sigmund and El Moctar also concluded that for small wavelengths added resistance is very dependent on wave-steepness, so this could be the reasons for inaccuracies at small wavelengths, [Sigmund and El Moctar 2018]. While [Söding and Shigunov 2015] does not share in the paper which grid-discretization he uses for the different tests, this thesis arrived at the conclusion of the importance of the cohesion between the grid in the free-surface and the wave modelled. What would be interesting to see, is if the grid set-up found in this thesis also could generate an accurate free-surface for short waves. That is, after the asymmetric problem of the wave modelling has been solved. [Sigmund and El Moctar 2018] used the same grid for all the different wavelengths they tested, and this is, based on the results in this thesis, unwise. Therefore, it could be that the problems with small wave-lengths has been due to an incorrectly gridding of the free-surface. In regards to potential methods, their inability to compute accurate results for added resistance in short waves is most likely to be rooted in the non-linearities that are more dominant for diffraction cases, than for radiation cases. The grid-fix would therefore not help the potential methods in increasing their accuracy as they are by

their definition inept to capture those physical subtleties. However, the grid-fix could increase the applicability of both RANS and Euler methods, and should be further researched.

The KVLCC2 tanker is a rather conventional tanker and the results obtained in this thesis could have been very different if another vessel, much more connected to the viscous domain, had been used. The current model has small relative motions, and larger relative motions could introduce larger viscous damping, and new challenges for the inviscid solver. A smaller ship with larger relative motions could prove a challenging case, or a ship with challenging appendages, such as a bilge keel. Which ship-designs the Euler solver is applicable for, and for which it is not, is necessary to assess. If its use stops at high C_B-valued, conservative ships, it might not be an engineering tool for the future.

In this thesis, the velocity was modelled by restraining the body's ability to move in certain DoFs while a current of water and air, equivalent of $Fn = 0.142$, approached the vessel. While this method has it advantages in its simplicity in set-up, it neglects certain aspects of realism, at least in an oblique wave-condition. With wave approaching the vessel at anything but directly head-waves, or following waves, there will be a lot of coupled motions, such as roll, yaw and sway. If the vessel was allowed to move in yaw and sway, it would lose its direction, and the current would suddenly not monitor the velocity anymore. To cope with this, either the domain would have to move with the vessel's motions, or the vessel would have to be equipped with a maneuvering function, modelling a rudder. What would then happen to the Euler solver, compared to the RANS-solver? And would the rudder force have to be modelled from computing the lift on the rudder itself, or could it be controlled by a function responding to the motions of the vessel, tuned to always get the vessel back to its original course? Of course this would mean that the vessel would have to move, and not the current, but this could also be modelled by a constant force equivalent to the calm water resistance, or a force-function responding to the oscillating wave force, or even more realistically, modelling the propeller geometry and computing its lift-force. Testing how the different simplifications work, and whether or not the Euler-solver can be used in those situations, would be very useful.

Bibliography

CD-Adapco (2018). *USER GUIDE*. accessed 15.01.2018 - 01.06.2018. URL: https://mdx.plm.automation.siemens.com/star-ccm-plus.

Arribas, F. Pérez (2007). "Some methods to obtain the added resistance of a ship advancing in waves". In: *Ocean Engineering* 34.7, pp. 946–955. ISSN: 0029-8018. DOI: https://doi.org/10.1016/j.oceaneng.2006.06.002. URL: http://www.sciencedirect.com/science/article/pii/S0029801806001818.

Azcueta, Rodrigo (2001). *Computation of turbulent free-surface flows around ships and floating bodies*. eng. Hamburg.

Böhm, Christoph and Kai Graf (2014). "Advancements in free surface RANSE simulations for sailing yacht applications". In: *Ocean Engineering* 90.Supplement C. Innovation in High Performance Sailing Yachts - INNOVSAIL, pp. 11–20. ISSN: 0029-8018. DOI: https://doi.org/10.1016/j.oceaneng.2014.06.038. URL: http://www.sciencedirect.com/science/article/pii/S0029801814002510.

Boom, H.V.D, I. van der Hout, and M. Flikkema (2008). "Speed-Power Performance of Ships during Trials and in Service". In: *SNAME*. URL: http://www.marin.nl/upload/5175b16b-86b1-4a24-bde0-3ab094ff7a13_SNAME_2008.doc__Speed-Power_Performance.pdf.

Cengel, Yunus A. and John M. Cimbala (2010a). *Fluid Mechanics Fundamentals and Applications, 2nd Edition*. 1221 Avenue of the Americas, New York, NY 10020: McGraw-Hill. Chap. 10.6, p. 556. ISBN: 978-007-128421-9.

– (2010b). *Fluid Mechanics Fundamentals and Applications, 2nd Edition*. 1221 Avenue of the Americas, New York, NY 10020: McGraw-Hill. Chap. 5, p. 202. ISBN: 978-007-128421-9.

– (2010c). *Fluid Mechanics Fundamentals and Applications, 2nd Edition*. 1221 Avenue of the Americas, New York, NY 10020: McGraw-Hill. Chap. 4.5, p. 155. ISBN: 978-007-128421-9.

– (2010d). *Fluid Mechanics Fundamentals and Applications, 2nd Edition*. 1221 Avenue of the Americas, New York, NY 10020: McGraw-Hill. Chap. 8, pp. 364–365. ISBN: 978-007-128421-9.

– (2010e). *Fluid Mechanics Fundamentals and Applications, 2nd Edition*. 1221 Avenue of the Americas, New York, NY 10020: McGraw-Hill. Chap. 10, pp. 576–577. ISBN: 978-007-128421-9.

Choi, Junwoo and Sung Bum Yoon (2009). "Numerical simulations using momentum source wavemaker applied to RANS equation model". In: *Coastal Engineering* 56.10, pp. 1043–1060. ISSN: 0378-3839. DOI: https://doi.org/10.1016/j.coastaleng.2009.06.009. URL: http://www.sciencedirect.com/science/article/pii/S0378383909000970.

Faltinsen, O. M. (1990). *Sea Loads on Ships and Offshore Structures*. The Pitt building, Trumpington Street, Camebridge CB2 1RP, United Kingdom: Camebridge University Press. Chap. 2, pp. 39–40. ISBN: 9780521178730.

– (2005). *Hydrodynamics of High-Speed Marine Vehicles*. 32 Avenue of the Americas, New York, NY 10013-2473, USA: Camebridge University Press. Chap. 2, pp. 22–25. ISBN: 0521458706.

Faltinsen, O.M, K Minsaas, N Liapis, and S Skjørdal (1980). *Prediction of resistance and propulsion of a ship in a seaway. In Proc. Thirteenth Symp. on Naval Hydrodynamics*. Tokyo: Symposium on Naval Hydrodynamics.

Fenton, John D (1985). "A Fifth-Order Stokes Theory for Steady Waves". eng. In: *Journal of Waterway, Port, Coastal, and Ocean Engineering* 111.2, pp. 216–234. ISSN: 0733-950X.

Gerritsma, J and W Beukelman (1971). *Analysis of the resistance increase in waves of a fast cargo ship*. eng. Delft.

Guo, B.J., S. Steen, and G.B. Deng (2012). "Seakeeping prediction of KVLCC2 in head waves with RANS". In: *Applied Ocean Research* 35, pp. 56–67. ISSN: 0141-1187. DOI: https://doi.org/10.1016/j.apor.2011.12.003. URL: http://www.sciencedirect.com/science/article/pii/S0141118711001040.

Hadzic, Hidajet (2006). "Development and Application of Finite Volume Method for the Computation of Flows Around Moving Bodies on Unstructured, Overlapping Grids; Entwicklung und Anwendung einer Finiten Volumen Methode fuer die Berechnung der Stroemung um einen bewegten Koerper mit unstrukturierenden, ueberlappenden Gittern; Entwicklung und Anwendung einer Finiten Volumen Methode fuer die Berechnung der Stroemung um einen bewegten Koerper mit unstrukturierenden, ueberlappenden Gittern". en. Advisor: Perić, Milovan; http://tubdok.tub.tuhh.de/handle/11420 PhD thesis. URL: http://hdl.handle.net/11420/233.

Hong, Liang, Ren-chuan Zhu, Guo-ping Miao, Ju Fan, and Shuai Li (2016). "An investigation into added resistance of vessels advancing in waves". In: *Ocean Engineering* 123, pp. 238–248. ISSN: 0029-8018. DOI: https://doi.org/10.1016/j.oceaneng.2016.07.033. URL: http://www.sciencedirect.com/science/article/pii/S0029801816302797.

IMO (2017). *Energy Efficiency Measures. Available at http://www.imo.org/en/OurWork/Environment/PollutionPrevention/AirPollution/Pages/Technical-and-Operational-Measures.aspx*. accessed 22.11.2017.

Islam, Hafizul, Md. Mashiur Rahman, M. Rafiqul Islam, Hiromichi Akimoto, and Laboni Afroz (2017). "Comparative Study of RaNS and PF based Solver for Predicting Added Resistance of a Very Large Crude Carrier". In: *Procedia Engineering* 194. 10th International Conference on Marine Technology, MARTEC 2016, pp. 74–81. ISSN: 1877-7058. DOI: https://doi.org/10.1016/j.proeng.2017.08.119. URL: http://www.sciencedirect.com/science/article/pii/S1877705817332599.

ITTC (2014a). *ITTC – Recommended Procedures and Guidelines: Speed and Power Trials, Part 2 Analysis of Speed/Power Trial Data*. eng. URL: http://www.staimo.org/Publications/Documents/ITTC_7_5-04-01-01_2_rev_1_1_11_Mar2014.pdf.

– (2014b). "Practical Guidelines for Ship CFD Applications". In: 6. URL: https://ittc.info/media/4196/75-03-02-03.pdf.

Jin, Yuting, Shuhong Chai, Jonathan Duffy, Christopher Chin, and Neil Bose (2017). "URANS predictions of wave induced loads and motions on ships in regular head and oblique waves at zero forward speed". In: *Journal of Fluids and Structures* 74, pp. 178–204. ISSN: 0889-9746. DOI: https://doi.org/10.1016/j.jfluidstructs.2017.07.009. URL: http://www.sciencedirect.com/science/article/pii/S0889974616307605.

Kim, Jang, Jim O'Sullivan, and Alex Read (2012). "RINGING ANALYSIS OF A VERTICAL CYLINDER BY EULER OVERLAY METHOD". In: *International Conference on Ocean, Offshore and Arctic Engineering OMAE* 4, pp. 855–866. DOI: https://doi.org/10.1016/j.coastaleng.2009.06.009. URL: http://proceedings.asmedigitalcollection.asme.org/proceeding.aspx?articleID=1732900.

Klein, T.S, T.J Craft, and H. Iacovides (2014). "Assessment of the performance of different classes of turbulence models in a wide range of non-equilibrium flows". In: *International Journal of Heat and Fluid Flow* 51, pp. 250–251.

Kreitner, J (1939). *Heave, Pitch and Resistance of Ships in a Seaway. Transactions of the Royal Institute of Naval Architects,'London,87*. eng.

Larsson, Lars, Frederick Stern, and Michel Visonneau (2013). "CFD in Ship Hydrodynamics—Results of the Gothenburg 2010 Workshop". In: *MARINE 2011, IV International Conference on Computational Methods in Marine Engineering: Selected Papers*. Ed. by Luís Eça, Eugenio Oñate, Julio García-Espinosa, Trond Kvamsdal, and Pål Bergan. Dordrecht: Springer Netherlands, pp. 237–259. ISBN: 978-94-007-6143-8. DOI: 10.1007/978-94-007-6143-8_14. URL: https://doi.org/10.1007/978-94-007-6143-8_14.

– (2014). *Numerical Ship Hydrodynamics*. eng. Dordrecht: Springer Netherlands. ISBN: 9400771886.

Larsson, Lars, Frederick Stern, and Michel Visonneau (2010). "Proceedings, Volume 2". In: *Gothenburg 2010 A Workshop on Numerical Ship Hydrodynamics*. Ed. by Lars Larsson, Frederick Stern, and Michel Visonneau. Gothenburg, Sweden: CHALMERS UNIVERSITY OF TECHNOLOGY. URL: http://extras.springer.com/2014/978-94-007-7188-8.

Lindstad, Haakon, Egil Jullumstrø, and Inge Sandaas (2013). "Reductions in cost and greenhouse gas emissions with new bulk ship designs enabled by the Panama Canal expansion". In: *Energy Policy* 59, pp. 341–349. ISSN: 0301-4215. DOI: https://doi.org/10.1016/j.enpol.2013.03.046. URL: http://www.sciencedirect.com/science/article/pii/S0301421513002243.

Liu, Cong, Jianhua Wang, and Decheng Wan (2018). "CFD Computation of Wave Forces and Motions of DTC Ship in Oblique Waves". In: *International Journal of Offshore and Polar Engineering* 28.2, pp. 154–163. ISSN: 10535381.

Liu, Shukui, Baoguo Shang, Apostolos Papanikolaou, and Victor Bolbot (2016). "Improved formula for estimating added resistance of ships in engineering applications". In: *Journal of Marine Science and Application* 15.4, pp. 442–451. ISSN: 1993-5048. DOI: 10.1007/s11804-016-1377-3. URL: https://doi.org/10.1007/s11804-016-1377-3.

Malenica, S., Y.M. Choi, Ch. Monroy, S. Seng, X.B. Chen, and V. Vukcevic (2017). *Some aspects of coupling the RANS based CFD with the potential flow models for seakeeping applications.* eng. China. URL: http://www.iwwwfb.org/Abstracts/iwwwfb32/iwwwfb32_35.pdf.

Maruo, H (1957). *The excess resistance of a ship in rough seas.* eng. URL: https://content.iospress.com/download/international-shipbuilding-progress/isp4-35-01?id=international-shipbuilding-progress%2Fisp4-35-01.

Molland, Anthony F., Stephen T. Turnock, and Dominic A. Hudson (2011a). *Ship Resistance and Propulsion - Practical Estimation of Ship Propulsive Power.* 32 Avenue of the Americas, New York, NY 10013-2473, USA: Cambridge University Press. Chap. 3, p. 12.

– (2011b). *Ship Resistance and Propulsion - Practical Estimation of Ship Propulsive Power.* 32 Avenue of the Americas, New York, NY 10013-2473, USA: Cambridge University Press. Chap. 3, pp. 17–20.

Newman, John Nicholas (1977). *Marine hydrodynamics.* eng.

Pettersen, Bjørnar (2007). *TMR4247 Marin teknikk 3 - Hydrodynamikk.* 7005 Trondheim: Kompendieforlaget, Akademika. Chap. 1, p. 2.

Pletcher, Richard H., John C. Tannehill, and Dale A. Andersen (2013a). *Computational Fluid Mechanics and Heat Transfer - Third Edition.* 6000 Broken Sound Parkway NW, Suite 300, Boca Raton: CRC Press Taylor Francis Group. Chap. 5, p. 251. ISBN: 9781591690375.

– (2013b). *Computational Fluid Mechanics and Heat Transfer - Third Edition.* 6000 Broken Sound Parkway NW, Suite 300, Boca Raton: CRC Press Taylor Francis Group. Chap. 5, p. 249. ISBN: 9781591690375.

– (2013c). *Computational Fluid Mechanics and Heat Transfer - Third Edition.* 6000 Broken Sound Parkway NW, Suite 300, Boca Raton: CRC Press Taylor Francis Group. Chap. 5, p. 276. ISBN: 9781591690375.

– (2013d). *Computational Fluid Mechanics and Heat Transfer - Third Edition.* 6000 Broken Sound Parkway NW, Suite 300, Boca Raton: CRC Press Taylor Francis Group. Chap. 5.4, pp. 294–312. ISBN: 9781591690375.

– (2013e). *Computational Fluid Mechanics and Heat Transfer - Third Edition.* 6000 Broken Sound Parkway NW, Suite 300, Boca Raton: CRC Press Taylor Francis Group. Chap. 5.4, pp. 294–312. ISBN: 9781591690375.

– (2013f). *Computational Fluid Mechanics and Heat Transfer - Third Edition.* 6000 Broken Sound Parkway NW, Suite 300, Boca Raton: CRC Press Taylor Francis Group. Chap. 3, pp. 43–56. ISBN: 9781591690375.

Ransau, Samuel R. (2003a). *Numerical Methods for Flows with Evolving Interfaces.* 7005 Trondheim: NTNU, Faculty of Science and Engineering, Department of Marine Technology. Chap. 1.

– (2003b). *Numerical Methods for Flows with Evolving Interfaces.* 7005 Trondheim: NTNU, Faculty of Science and Engineering, Department of Marine Technology. Chap. 0.

– (2003c). *Numerical Methods for Flows with Evolving Interfaces.* 7005 Trondheim: NTNU, Faculty of Science and Engineering, Department of Marine Technology. Chap. 1.

Rhee, Shin Hyung, Boris P. Makarov, H. Krishinan, and Vladimir Ivanov (2005). "Assessment of the volume of fluid method for free-surface wave flow". In: *Journal of Marine Science and Technology* 10.4, pp. 173–180. ISSN: 1437-8213. DOI: 10.1007/s00773-005-0205-2. URL: https://doi.org/10.1007/s00773-005-0205-2.

Rørvik, Jørgen (2016). "Application of Inviscid Flow CFD for prediction of Motions and Added Resistance of Ships". In:

Salvesen, N, E.O Tuck, and E.O Faltinsen (1971). *Ship motions and sea loads*. eng. Oslo.

Sclavounos, Paul D. and Henning Borgen (2004). "Seakeeping analysis of a high-speed monohull with a motion-control bow hydrofoil". In: *Journal of Ship Research* 48.2, pp. 77–117. ISSN: 00224502.

Seo, Min-Guk, Dong-Min Park, Kyung-Kyu Yang, and Yonghwan Kim (2013). "Comparative study on computation of ship added resistance in waves". In: *Ocean Engineering* 73, pp. 1–15. ISSN: 0029-8018. DOI: https://doi.org/10.1016/j.oceaneng.2013.07.008. URL: http://www.sciencedirect.com/science/article/pii/S0029801813002965.

Shao, Y.L and O.M Faltinsen (2010). *Numerical Study on the Second-Order Radiation/Diffraction of Floating Bodies with/without Forward Speed*. China: IWWWFB. URL: http://www.iwwwfb.org/Abstracts/iwwwfb25/iwwwfb25_39.pdf.

Sigmund, Sebastian and Ould El Moctar (2018). "Numerical and experimental investigation of added resistance of different ship types in short and long waves". eng. In: 147, pp. 51–67. ISSN: 0029-8018.

Simonsen, Claud D., Janne F. Otzen, and Soizic Joncquez (2013). "EFD and CFD for KCS heaving and pitching in regular head waves". In: *Journal of Marine Science and Technology* 18, p. 443.

Simonsen, Claus D., Janne F. Otzen, Soizic Joncquez, and Frederick Stern (2013). "EFD and CFD for KCS heaving and pitching in regular head waves". In: *Journal of Marine Science and Technology* 18.4, pp. 435–459. ISSN: 1437-8213. DOI: 10.1007/s00773-013-0219-0. URL: https://doi.org/10.1007/s00773-013-0219-0.

Söding, Heinrich and Vladimir Shigunov (2015). "Added resistance of ships in waves †". eng. In: *Ship Technology Research* 62.1, pp. 2–13. ISSN: 0937-7255.

Sprenger, Florian, Vahid Hassani, Adolfo Maron, Guillaume Delefortrie, Thibaut Van Zwijnsvoorde, Andrés Cura-Hochbaum, and Antonio Lengwinat (2016). "Establishment of a Validation and Benchmark Database for the Assessment of Ship Operation in Adverse Conditions". eng. In: *Proceedings of the 35th International Conference on Ocean, Offshore & Arctic Engineering (OMAE)*. Busan, South-Korea: ASME, pp. 1–12. ISBN: 9780791849927. URL: http://dx.doi.org/10.1115/omae2016-54865.

Steen, Sverre (2014). *TMR4247 Marin teknikk 3 - Hydrodynamikk Motstand og propulsjon Propell og foilteori*. 7005 Trondheim: Kompendieforlaget, Akademika. Chap. 1, p. 16.

Stern, Frederick, Hamid Sadat-Hosseini, Maysam Mousaviraad, and Shanti Bhushan (2014). "Evaluation of Seakeeping Predictions". In: *Numerical Ship Hydrodynamics: An assessment of the Gothenburg 2010 Workshop*. Ed. by Lars Larsson, Frederick Stern, and Michel Visonneau. Dordrecht: Springer Netherlands, pp. 141–202. ISBN: 978-94-007-7189-5. DOI: 10.1007/978-94-007-7189-5_4. URL: https://doi.org/10.1007/978-94-007-7189-5_4.

Subramanian, Rahul and Robert F. Beck (2015). "A time-domain strip theory approach to maneuvering in a seaway". In: *Ocean Engineering* 104, pp. 107–118. ISSN: 0029-8018. DOI: https://doi.org/10.1016/j.oceaneng.2015.04.071. URL: http://www.sciencedirect.com/science/article/pii/S0029801815001584.

Tennekes, H. and J. L. Lumley (1972). *A First Course in Turbulence*. Cambridge, Massachusetts: The MIT Press. Chap. 2 and 5. ISBN: 978-0-262-20019-6.

Volker, Bertram (2012). *Practical ship hydrodynamics*. eng. Amsterdam.

Volker, Bertram and Patrick Couser (2014). *Computational Methods for Seakeeping and Added Resistance in Waves*. eng. Hamburg: International Conference on Computer and IT Applications in the Maritime Industries.

White, Frank M. (2006). *Viscous Fluid Flow 3rd Edition*. 1221 Avenue of the Americas, New York, NY 10020: McGraw-Hill. Chap. 6-4, pp. 416–417. ISBN: 978-0-07-240231-5.

Wu, H.Y., C. Ma, W. Li, D.C. Wan, and F Noblesse (2017). *Local-flow component in the Green function for diffraction radiation of water waves*. eng. China. URL: http://www.iwwwfb.org/Abstracts/iwwwfb32/iwwwfb32_53.pdf.

Yang, Kyung-Kyu, Yonghwan Kim, and Bo-Woo Nam (2015). "Cartesian-grid-based computational analysis for added resistance in waves". In: *Journal of Marine Science and Technology* 20.1, pp. 155–170. ISSN: 1437-8213. DOI: 10.1007/s00773-014-0276-z. URL: https://doi.org/10.1007/s00773-014-0276-z.

Appendix A

Calm Water Simulation

A.1 Viscous Simulation

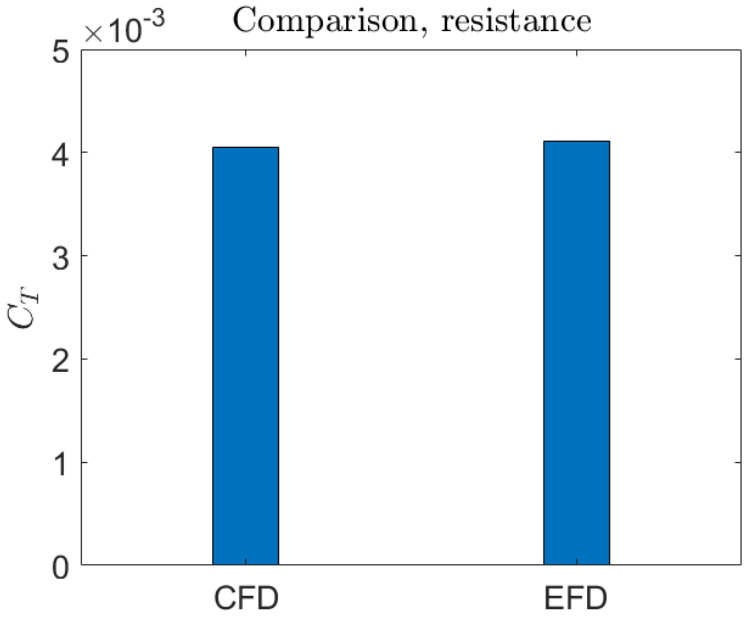

Figure A.1: Viscous total resistance coefficient comparison, calm-water

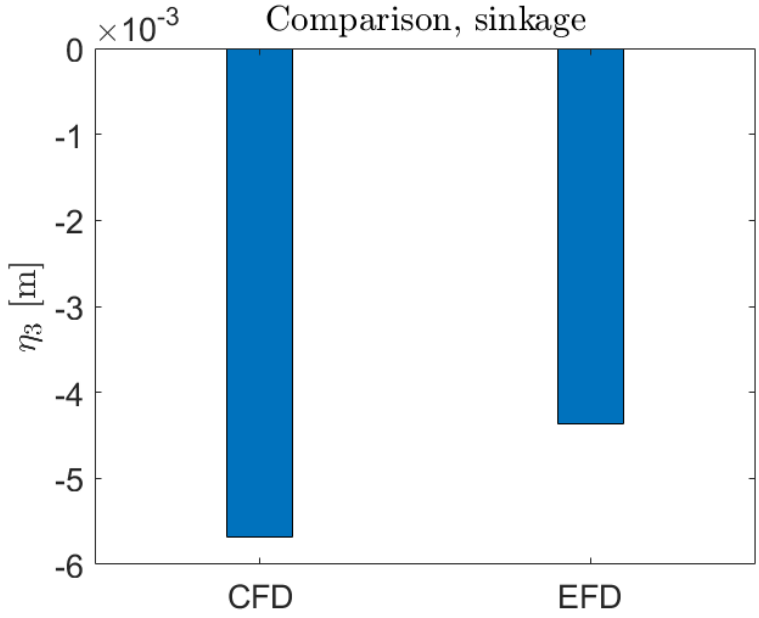

Figure A.2: Viscous sinkage comparison, calm-water

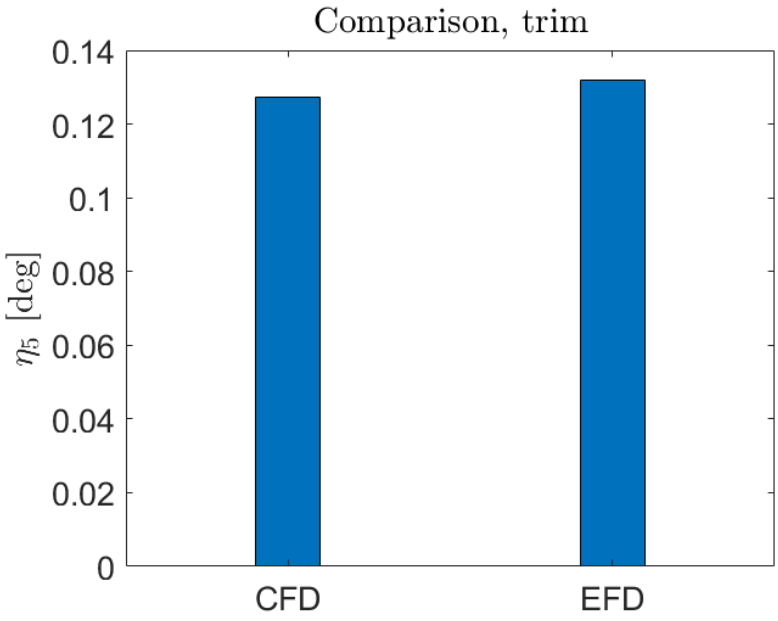

Figure A.3: Viscous trim comparison, calm-water

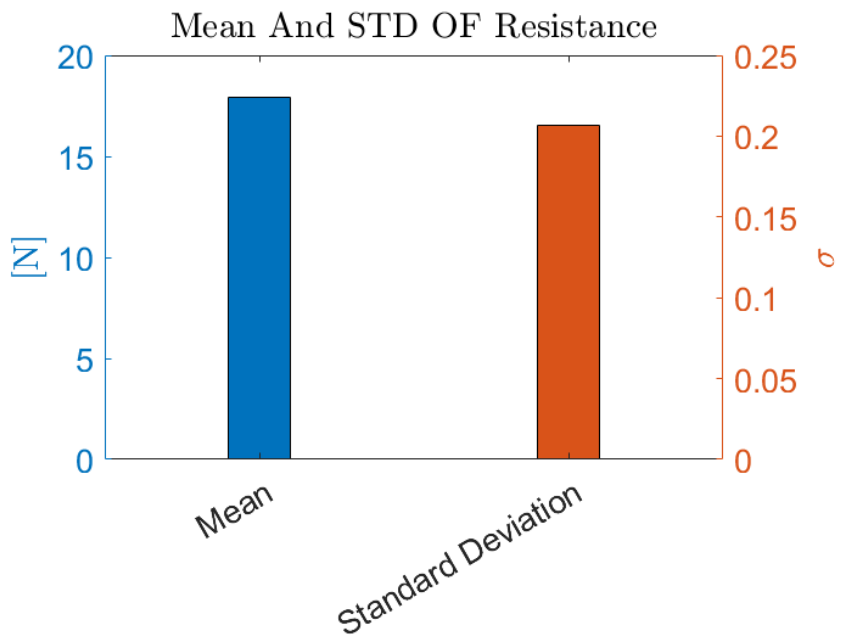

Figure A.4: Viscous mean and standard deviation, total resistance, calm water

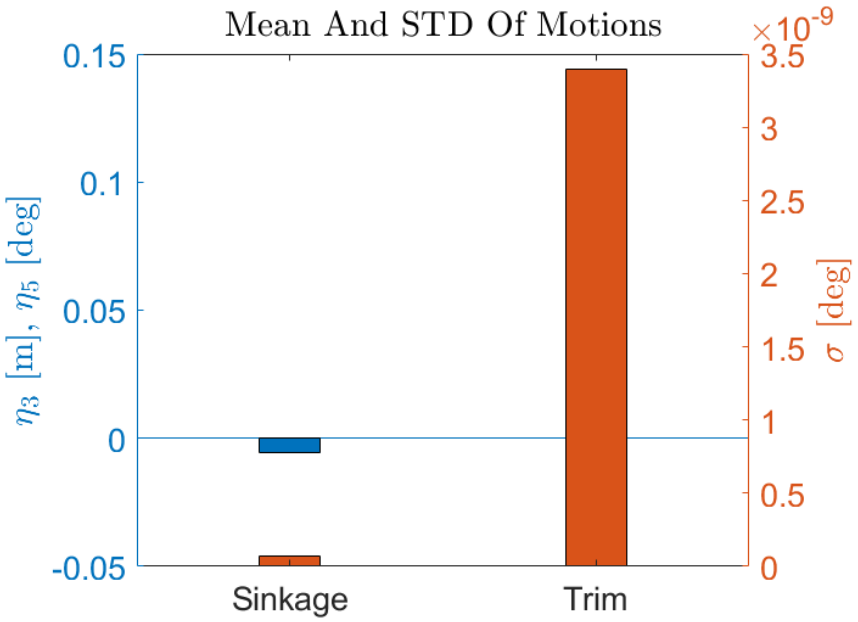

Figure A.5: Viscous mean and standard deviation, motions, calm water

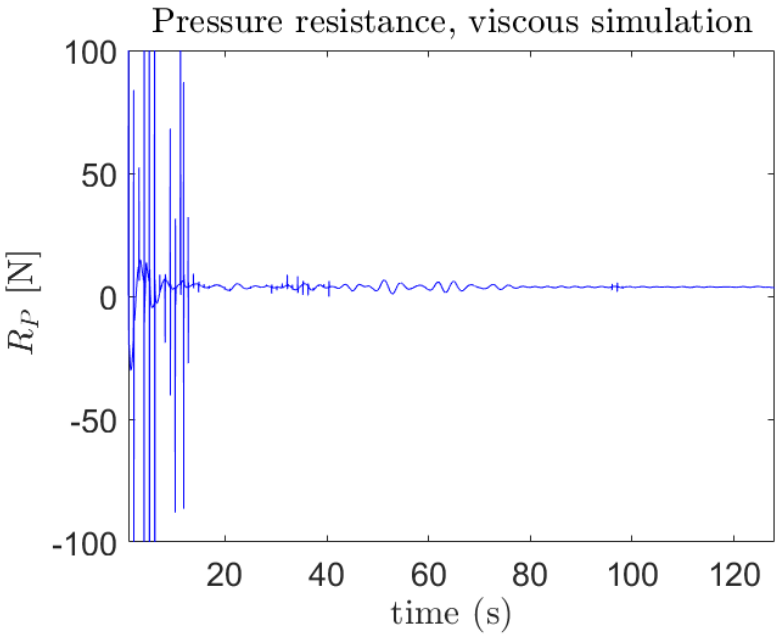

Figure A.6: Total pressure resistance, calm water

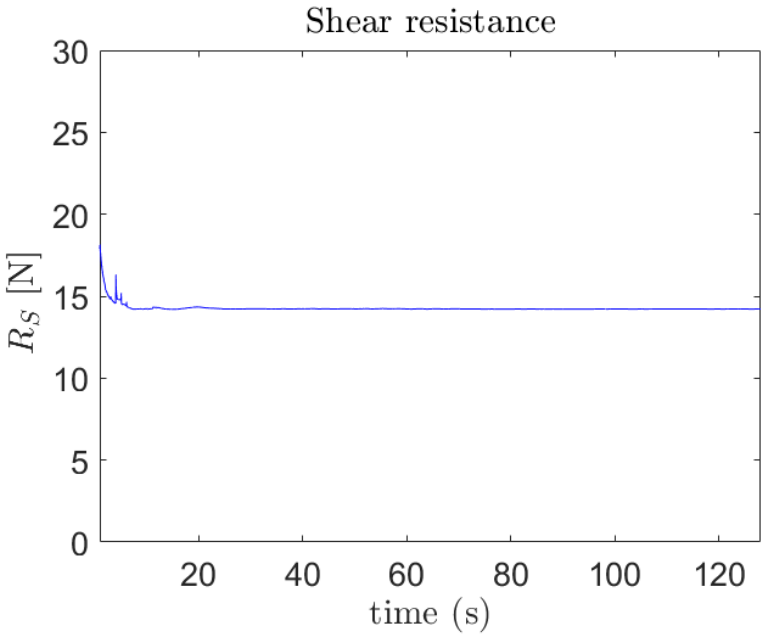

Figure A.7: Shear resistance, calm water

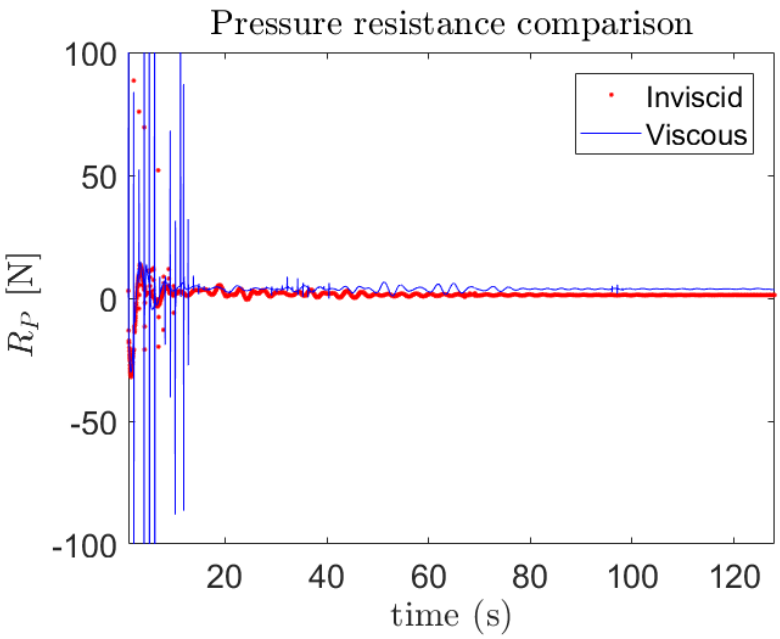

Figure A.8: Viscous and inviscid pressure resistance, calm water

A.2 Inviscid Simulation

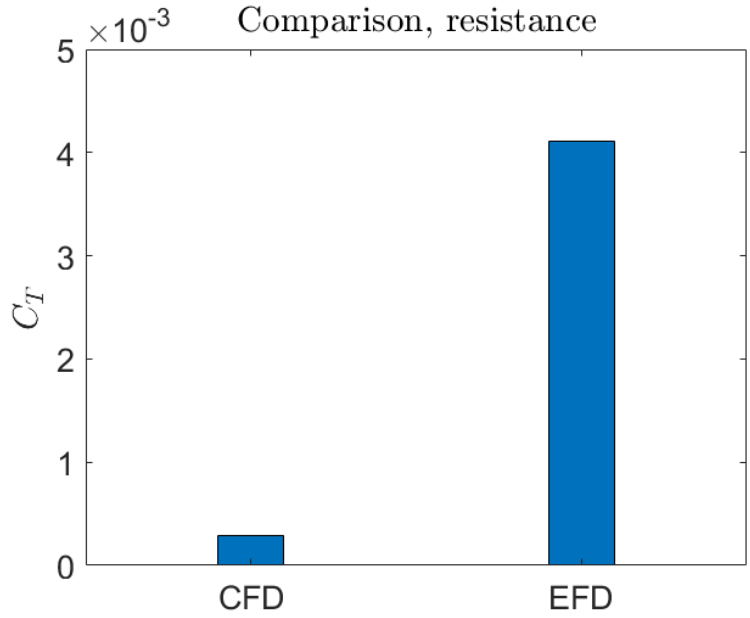

Figure A.9: Inviscid total resistance coefficient comparison, calm-water

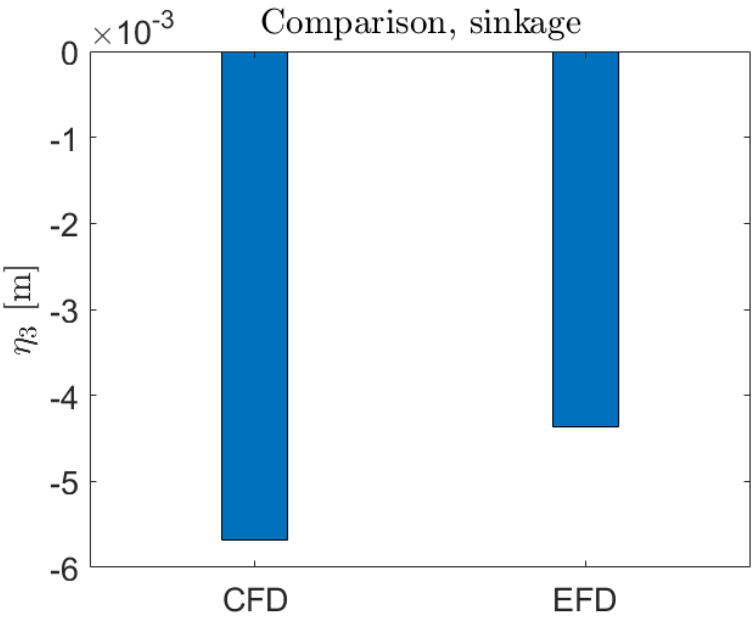

Figure A.10: Inviscid sinkage comparison, calm-water

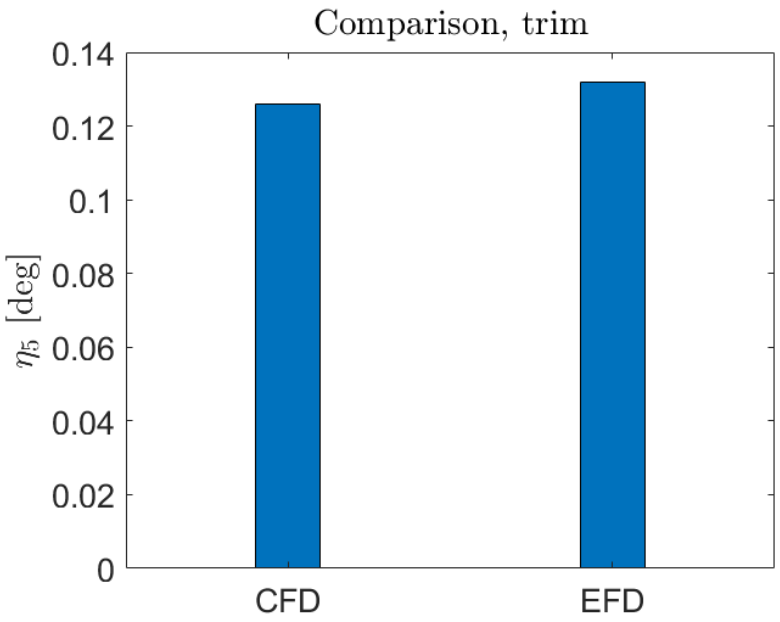

Figure A.11: Inviscid trim comparison, calm-water

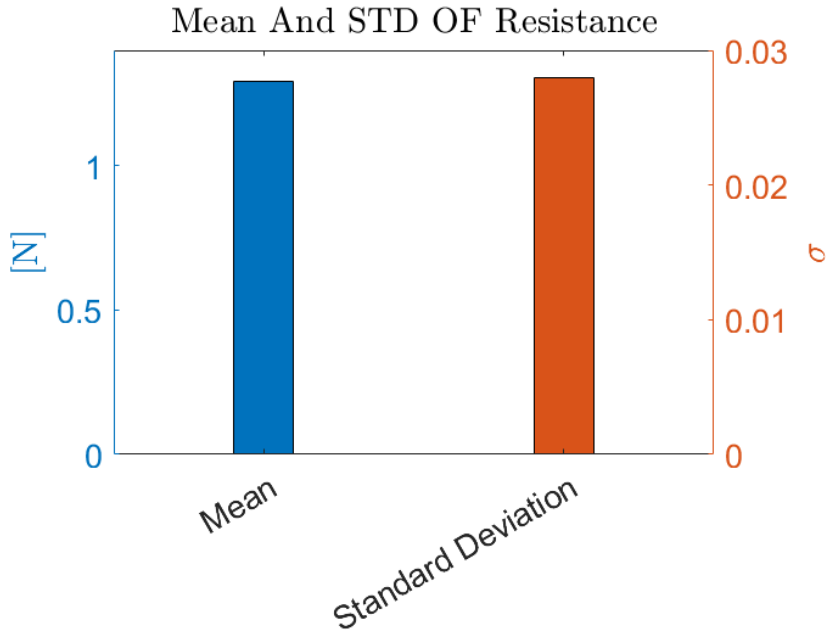

Figure A.12: Inviscid mean and standard deviation, total resistance, calm water

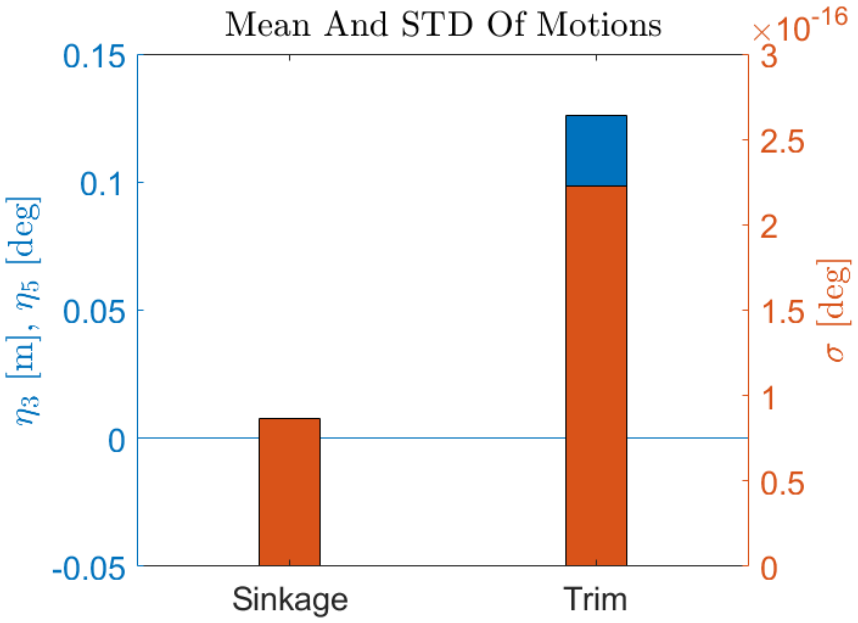

Figure A.13: Inviscid mean and standard deviation, motions, calm water

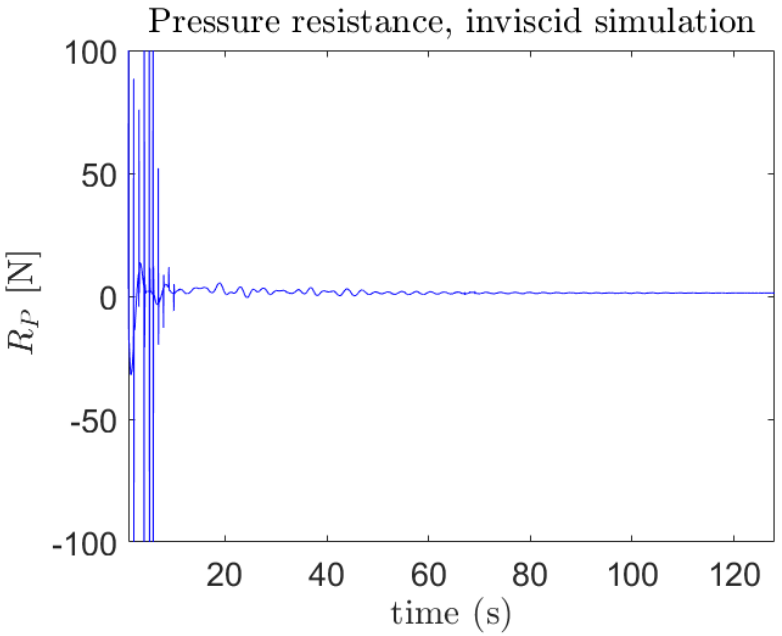

Figure A.14: Inviscid pressure resistance, calm water

Appendix B

Head Wave Simulation

B.0.1 Viscous Simulation

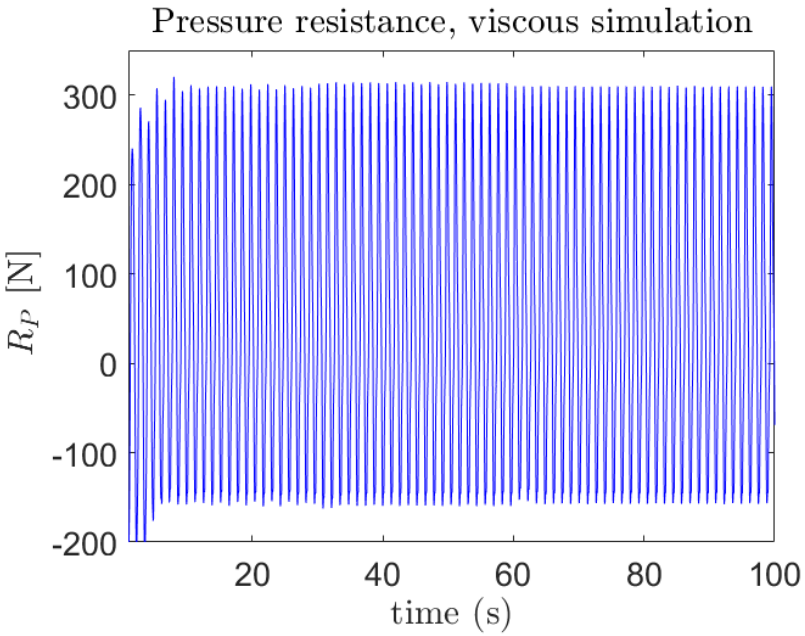

Figure B.1: Time-series of the pressure resistance

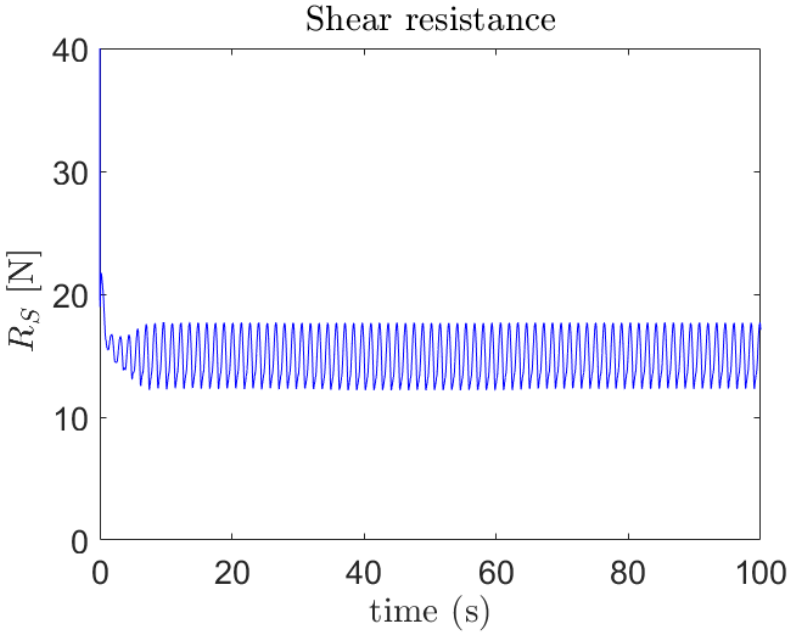

Figure B.2: Time-series of the shear resistance

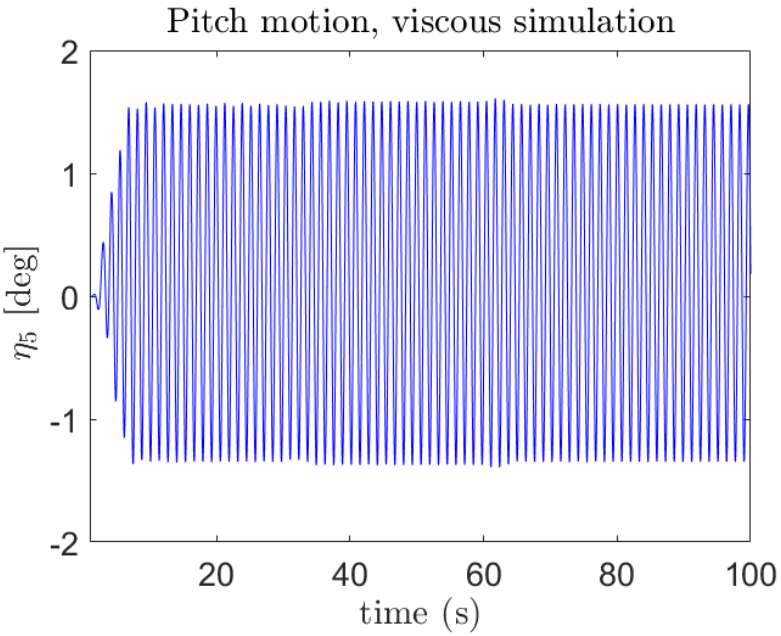

Figure B.3: Concentrated time series, pitch motion

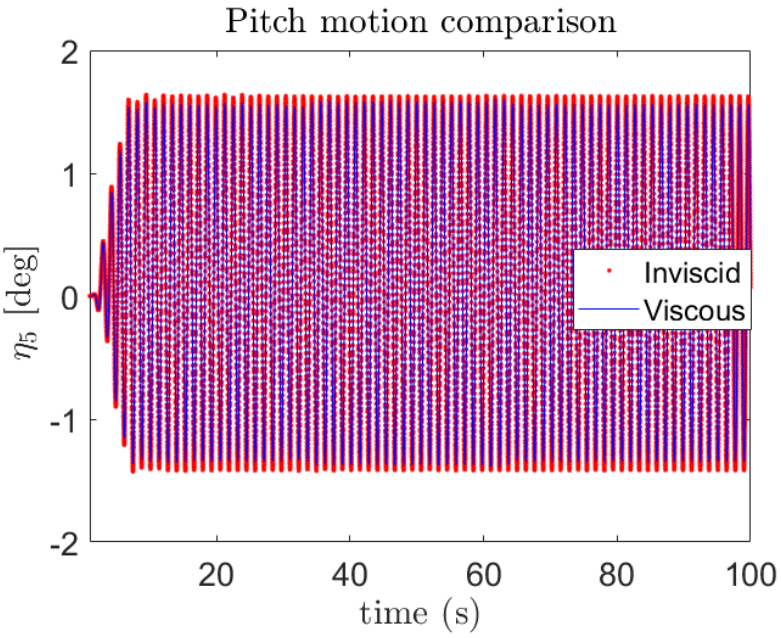

Figure B.4: Pitch motion comparison, head waves

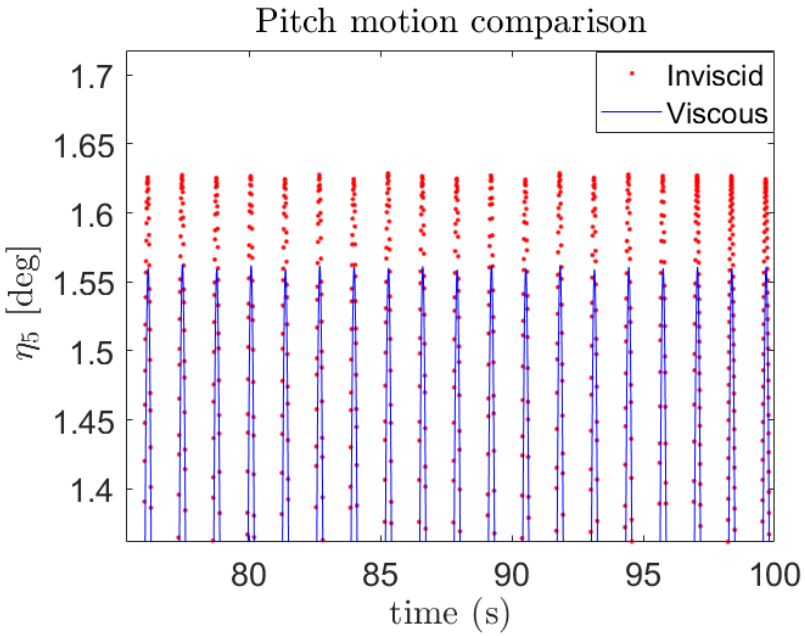

Figure B.5: Pitch motion maximum amplitude comparison, head waves

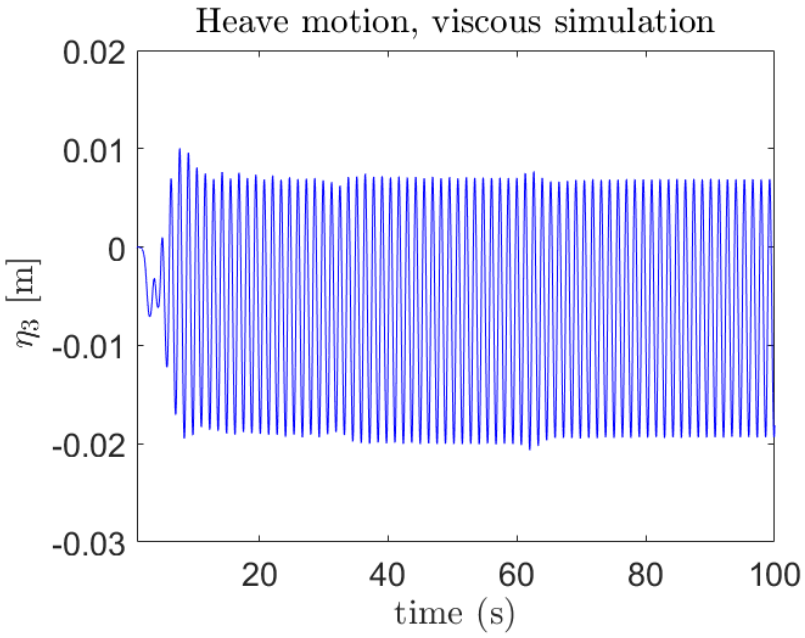

Figure B.6: Concentrated time series, heave motion

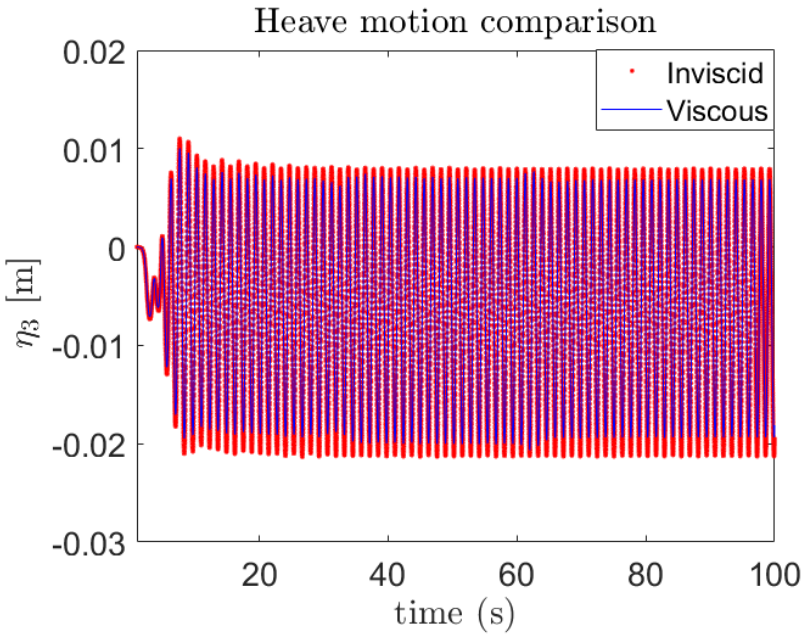

Figure B.7: Heave motion comparison, head waves

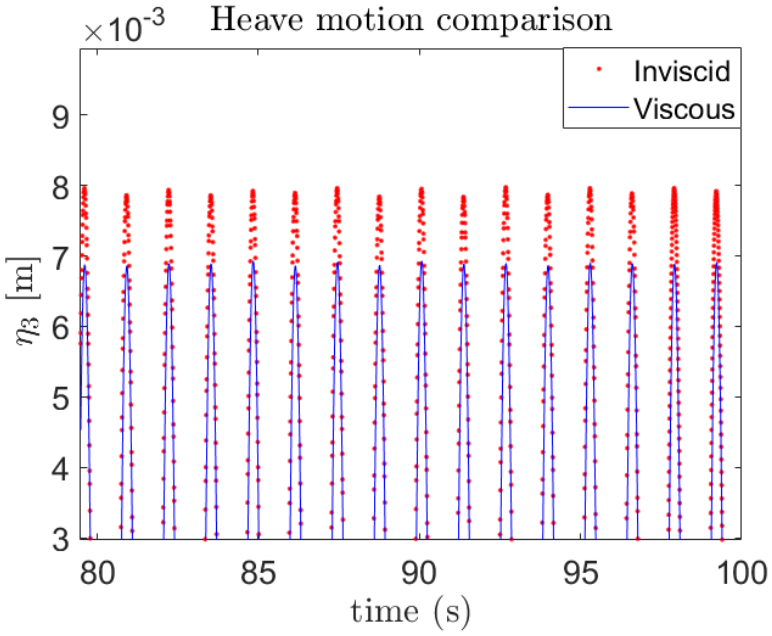

Figure B.8: Heave motion maximum amplitude comparison, head waves

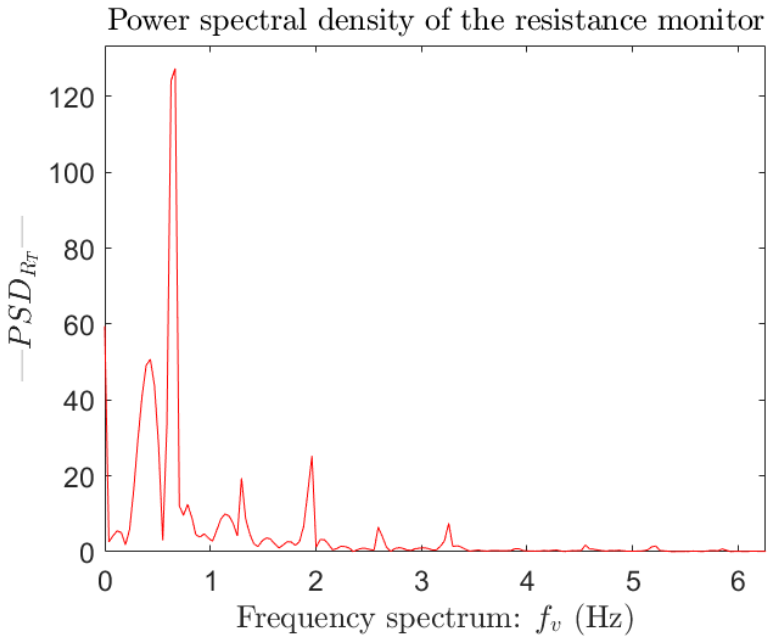

Figure B.9: Power spectral density plot, resistance

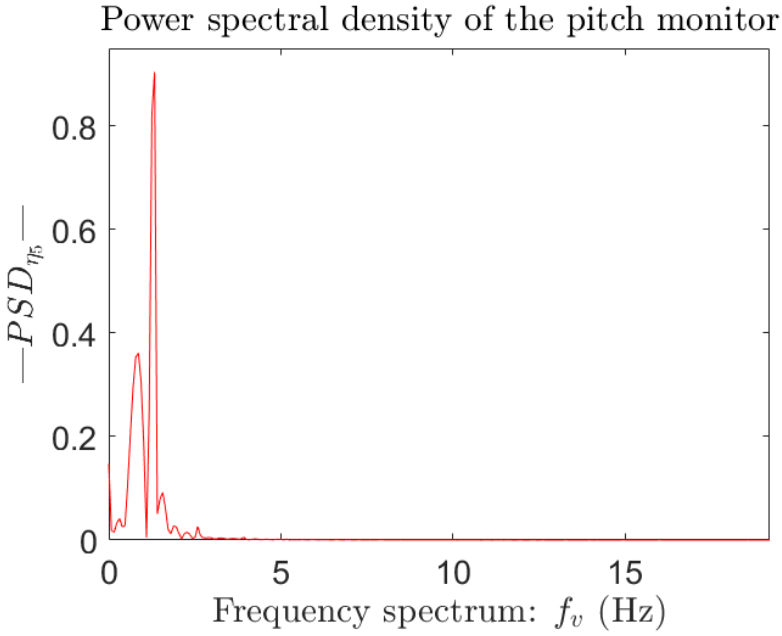

Figure B.10: Power spectral density plot, pitch

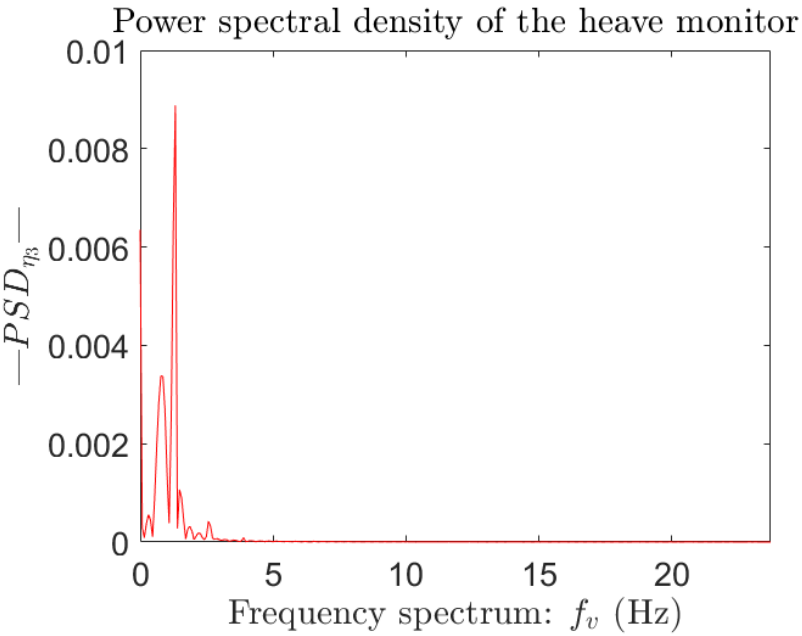

Figure B.11: Power spectral density plot, heave

B.0.2 Inviscid Simulation

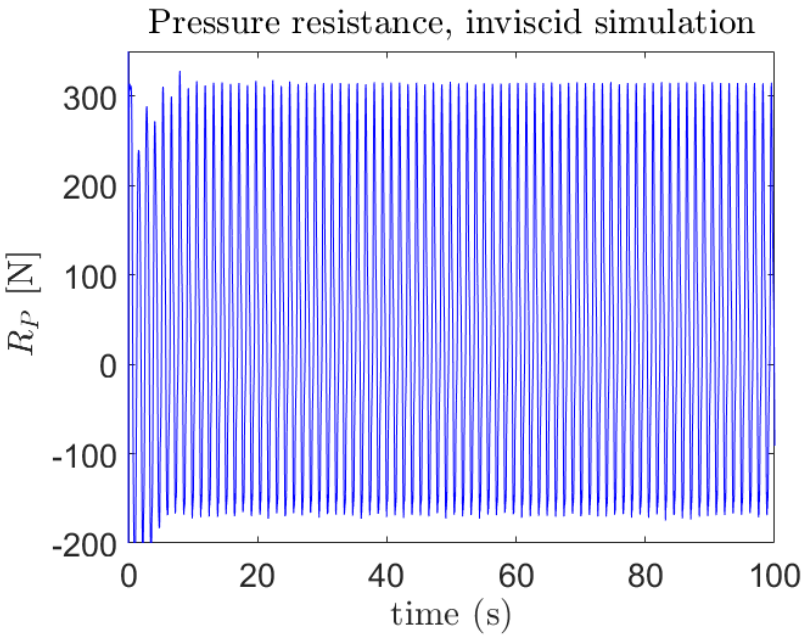

Figure B.12: Time-series of the pressure resistance

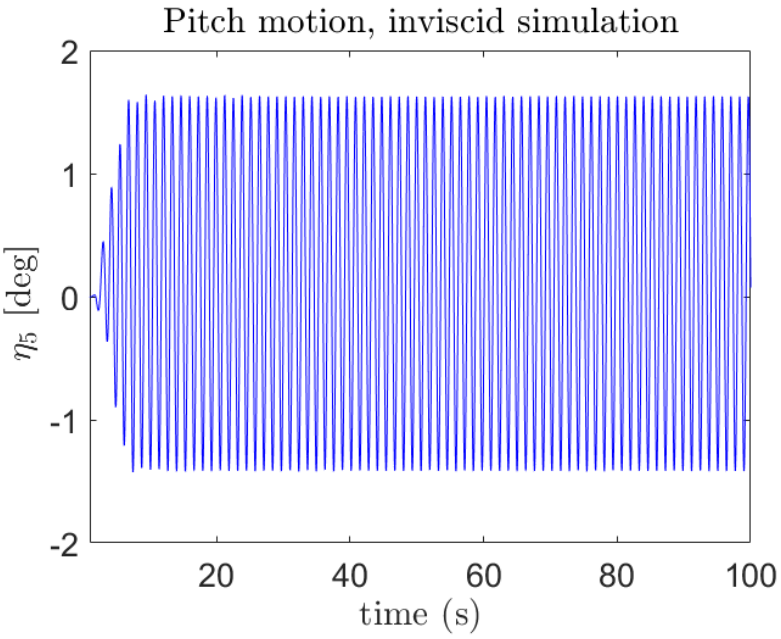

Figure B.13: Concentrated time series, pitch motion

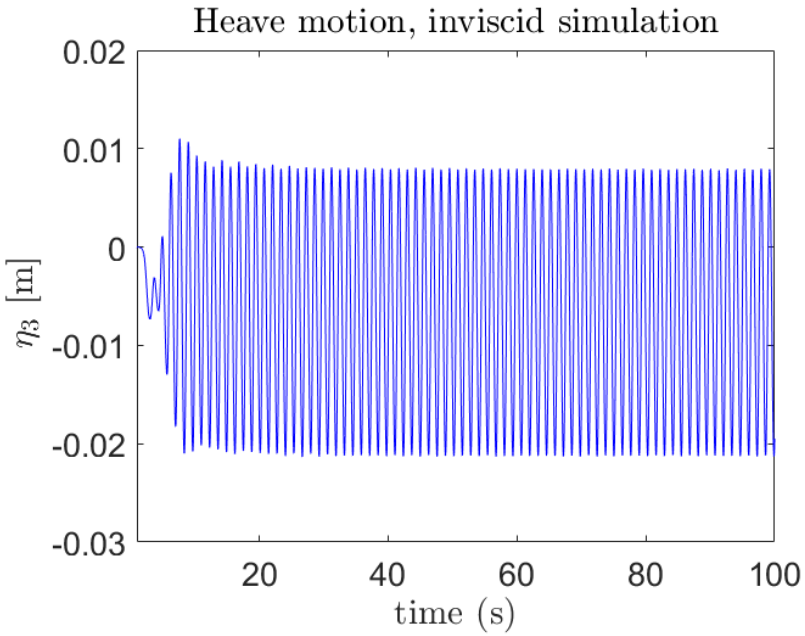

Figure B.14: Concentrated time series, heave motion

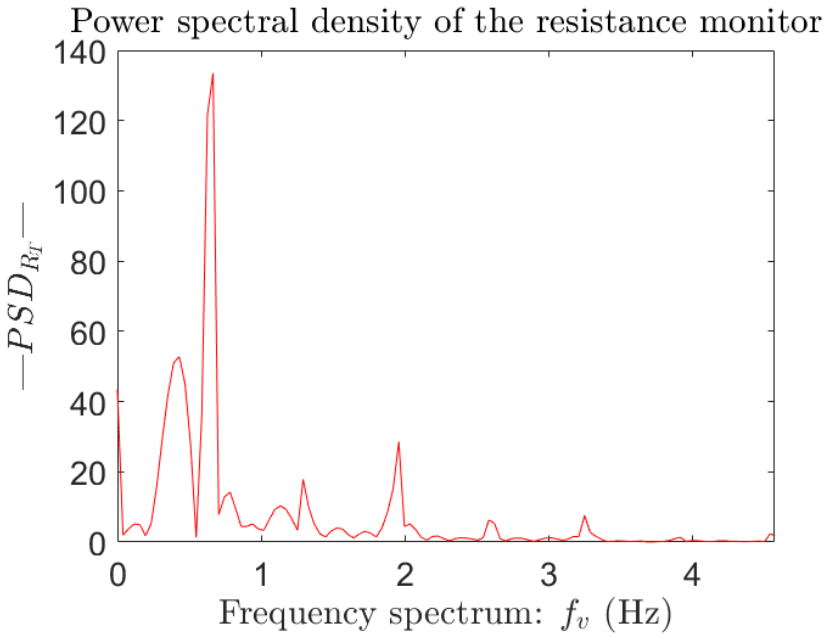

Figure B.15: Power spectral density plot, resistance

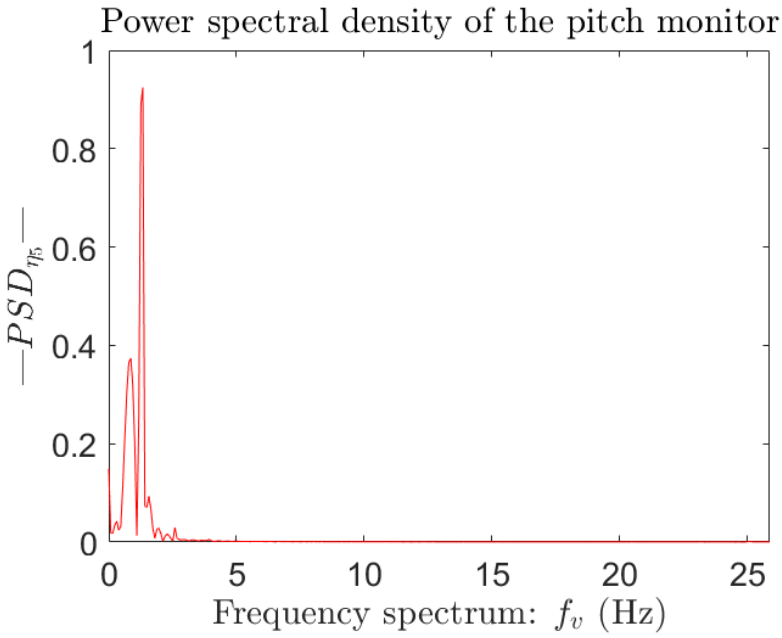

Figure B.16: Power spectral density plot, pitch

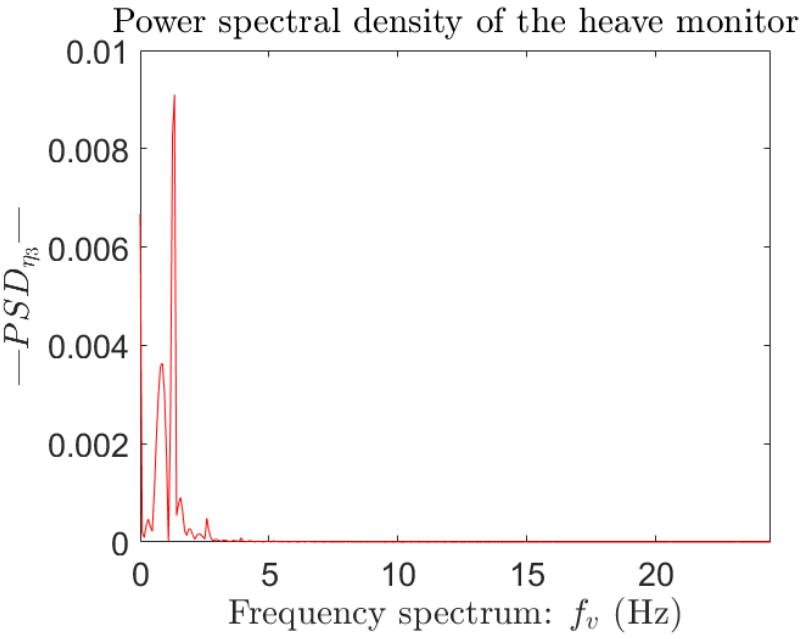

Figure B.17: Power spectral density plot, heave

Appendix C

Oblique Wave Simulation

C.1 Viscous Simulation

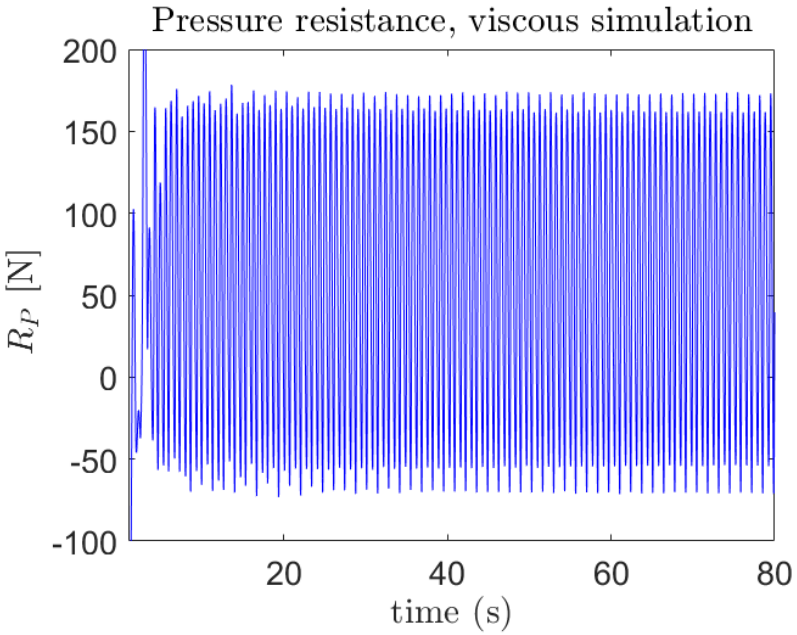

Figure C.1: Viscous pressure resistance, oblique wave

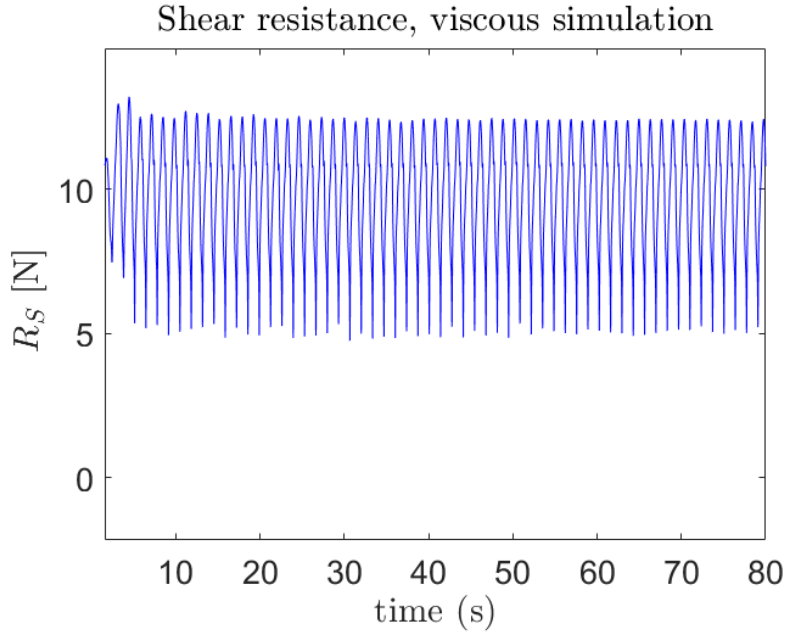

Figure C.2: Time-plot of viscous shear resistance, oblique wave

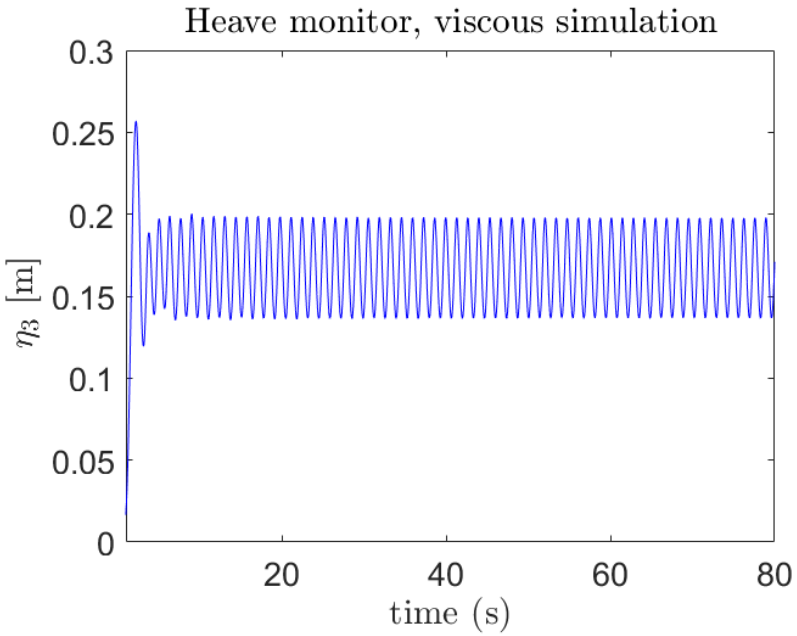

Figure C.3: Viscous Heave motion, oblique wave

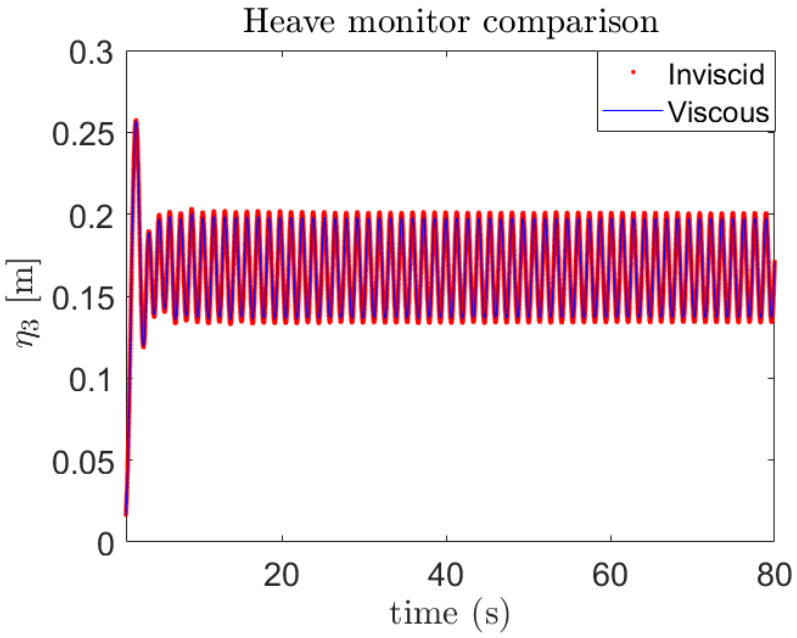

Figure C.4: Heave motion comparison, oblique wave

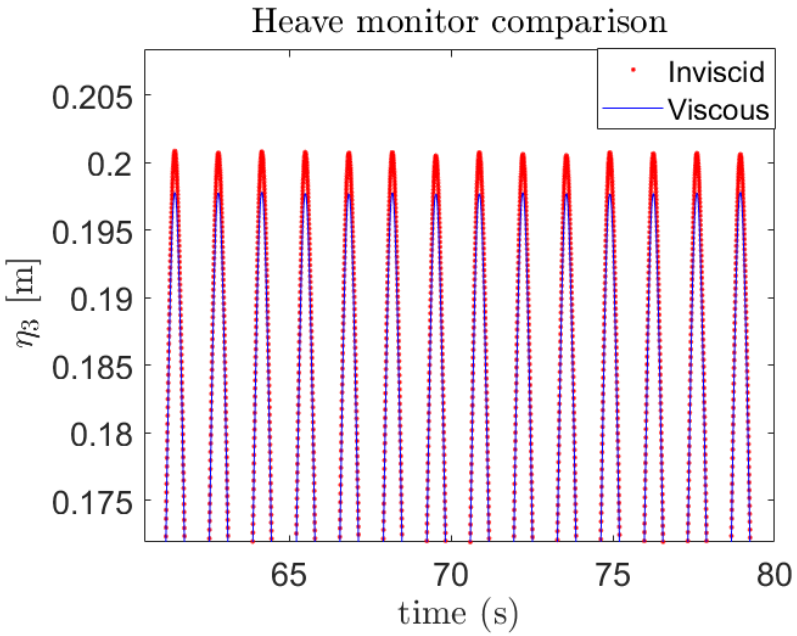

Figure C.5: Heave motion comparison, oblique wave

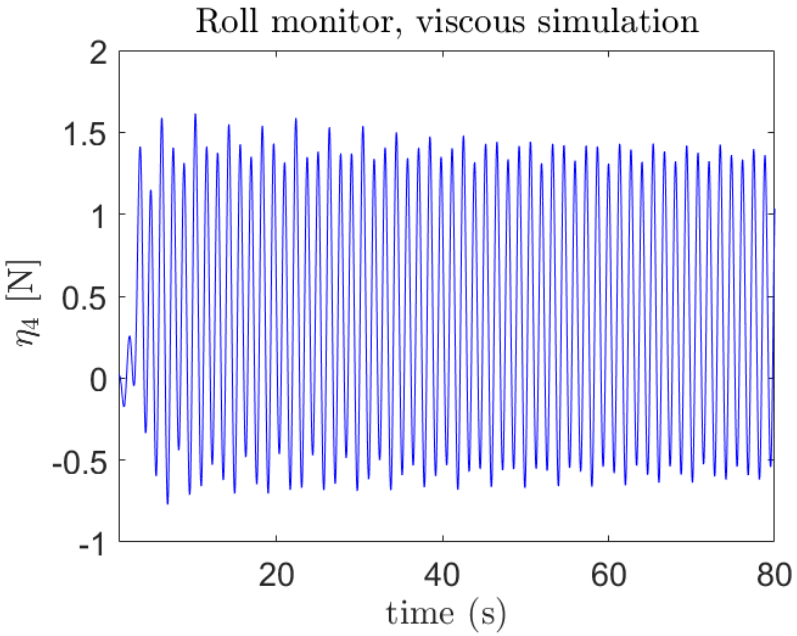

Figure C.6: Viscous roll motion, oblique wave

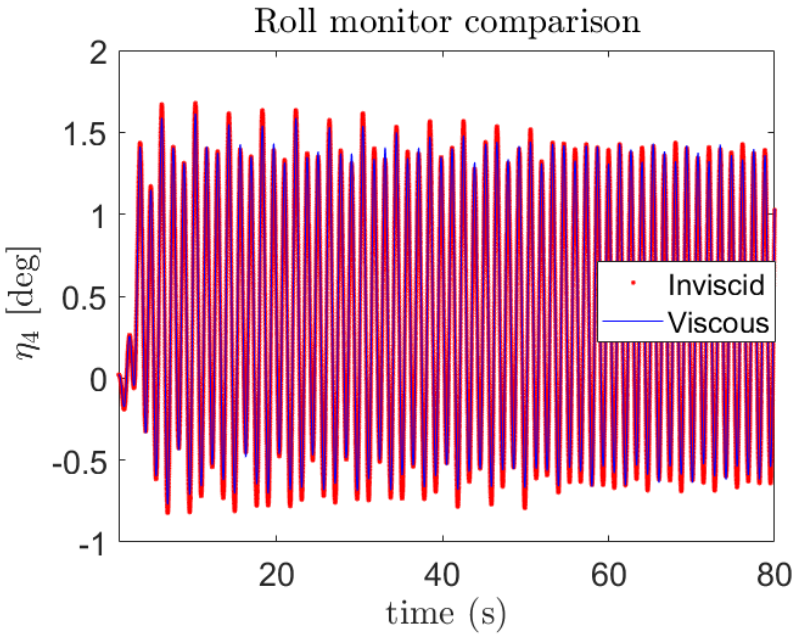

Figure C.7: Roll motion comparison, oblique wave

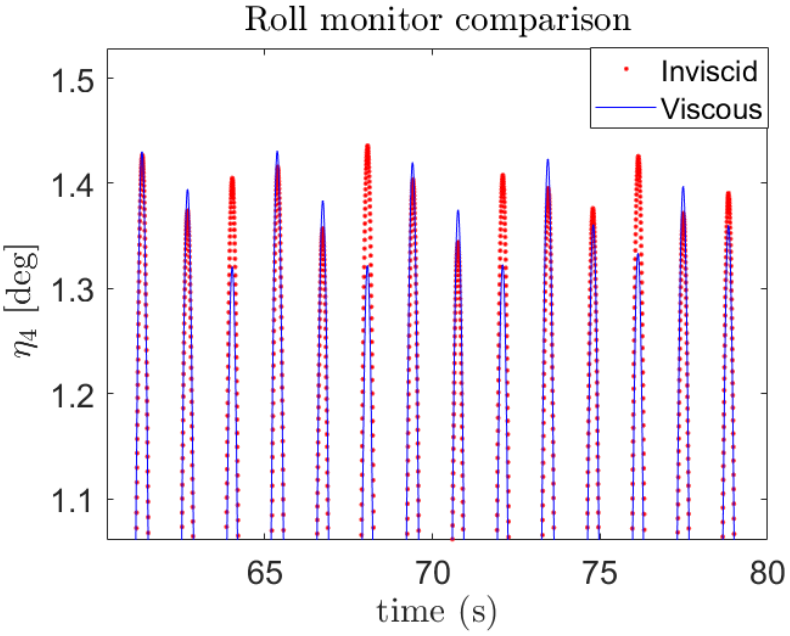

Figure C.8: Roll motion maximum amplitude comparison, oblique wave

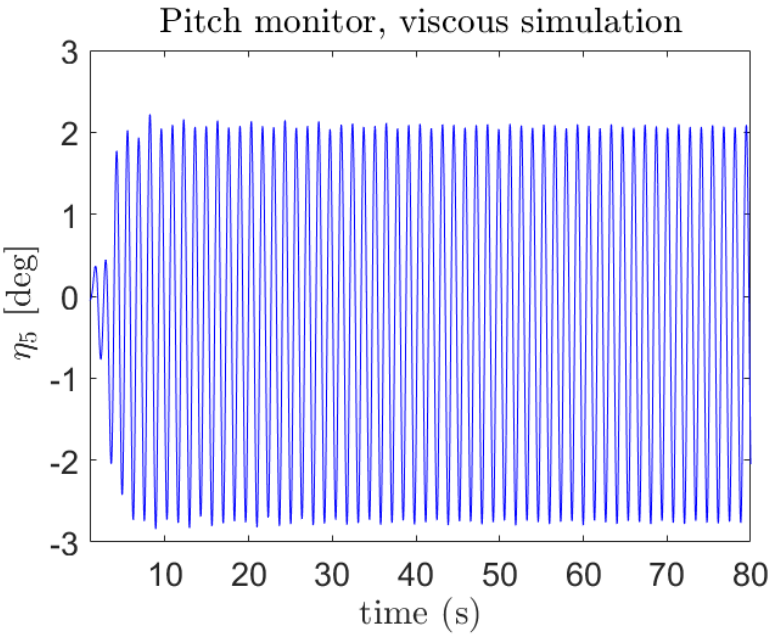

Figure C.9: Viscous pitch motion, oblique wave

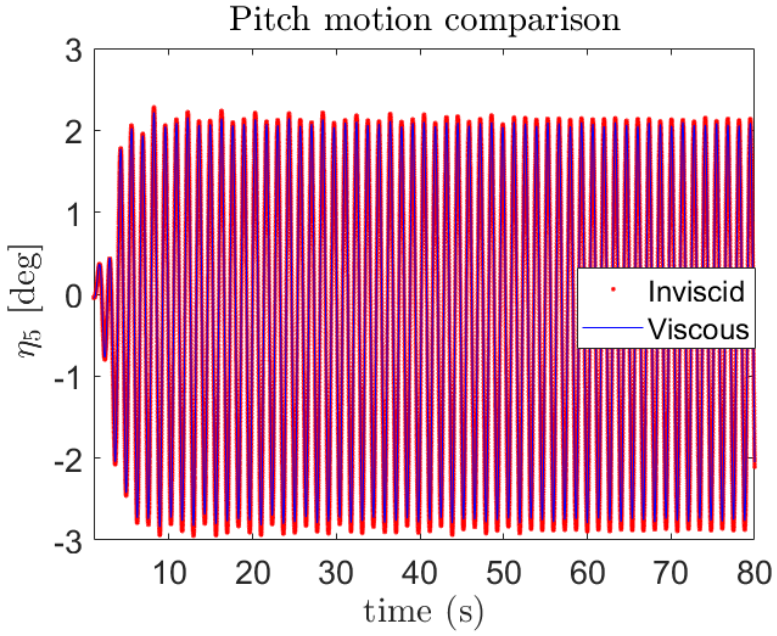

Figure C.10: Pitch motion comparison, oblique wave

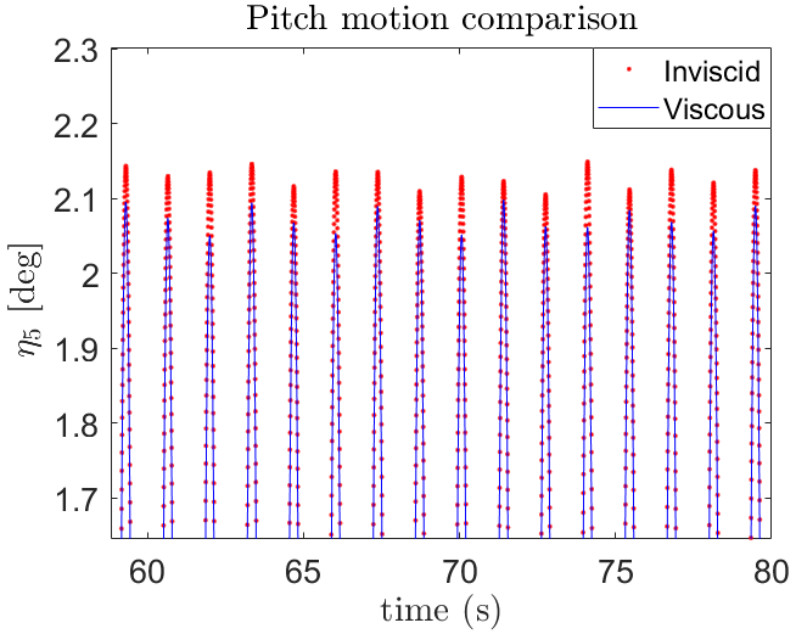

Figure C.11: Pitch motion maximum amplitude comparison, oblique wave

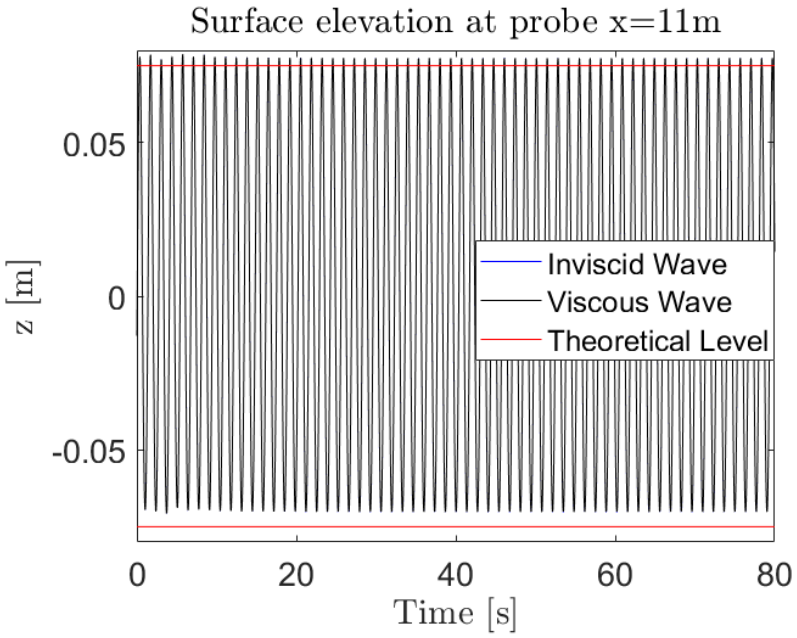

Figure C.12: Wave-probe at y=6m, x=11m, oblique wave

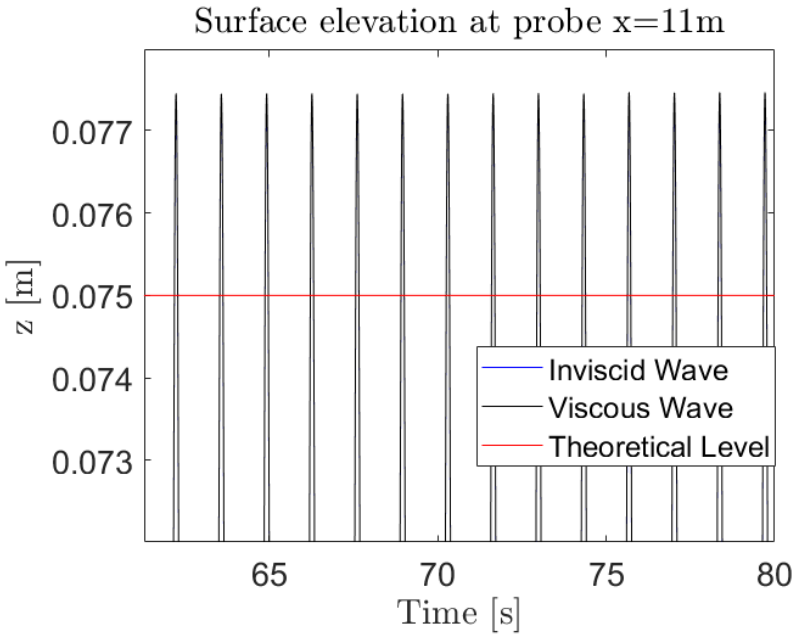

Figure C.13: Wave max amplitude comparison at y=6m, x=11m, oblique wave

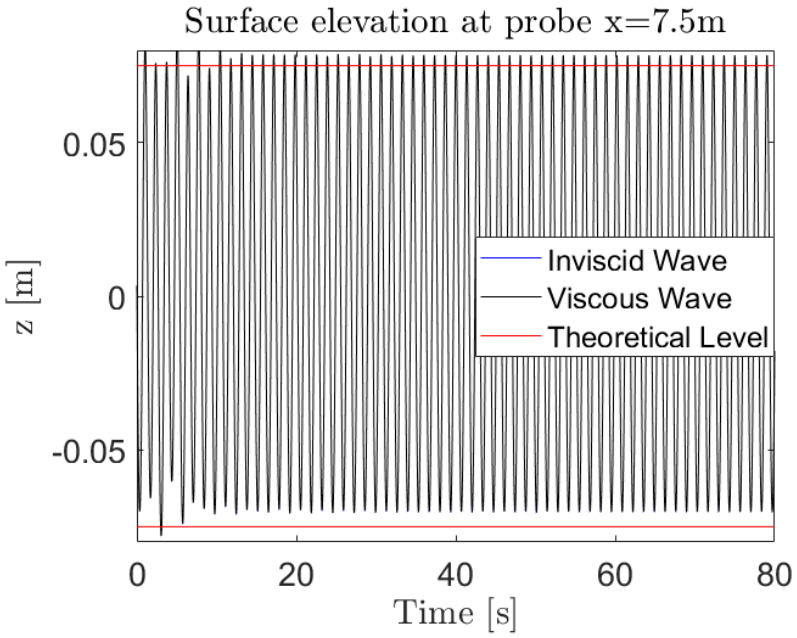

Figure C.14: Wave-probe at y=6m, x=7.5m, oblique wave

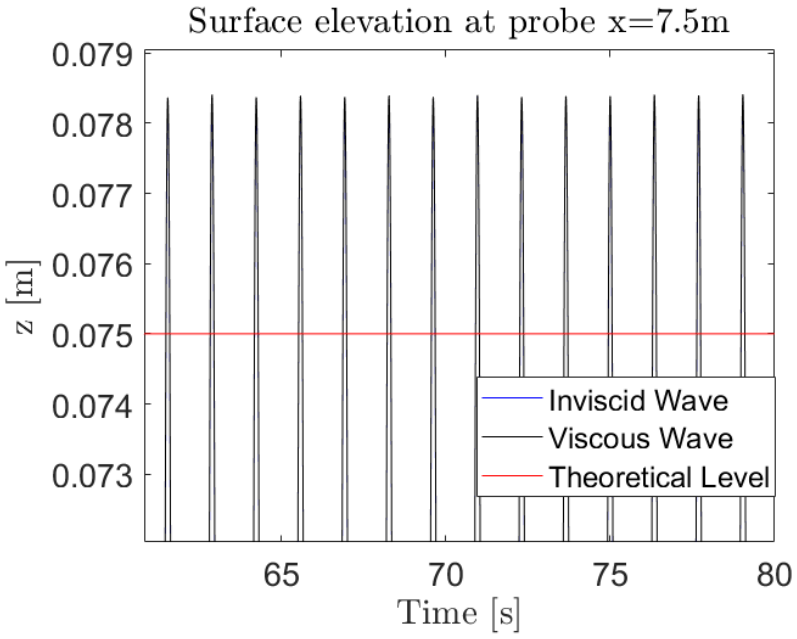

Figure C.15: Wave max amplitude comparison at y=6m, x=7.5m, oblique wave

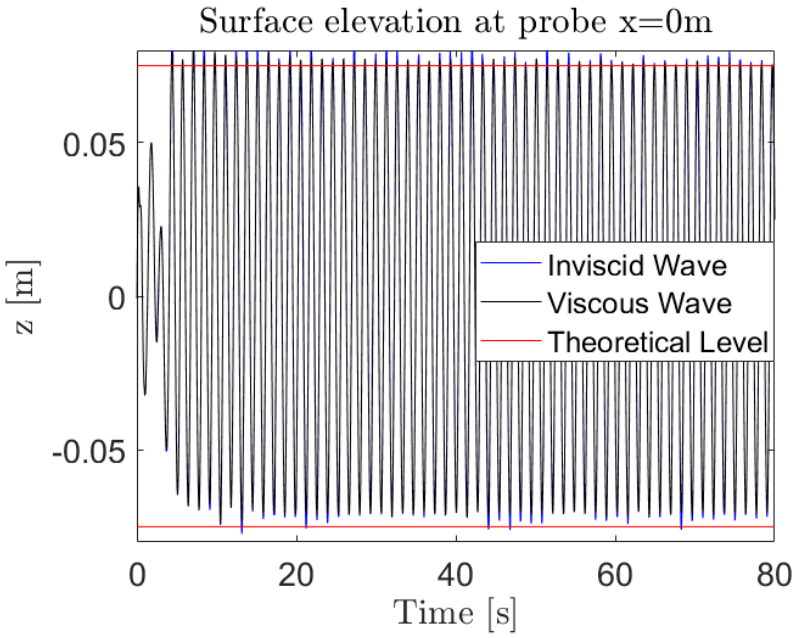

Figure C.16: Wave-probe at y=6m, x=0m, oblique wave

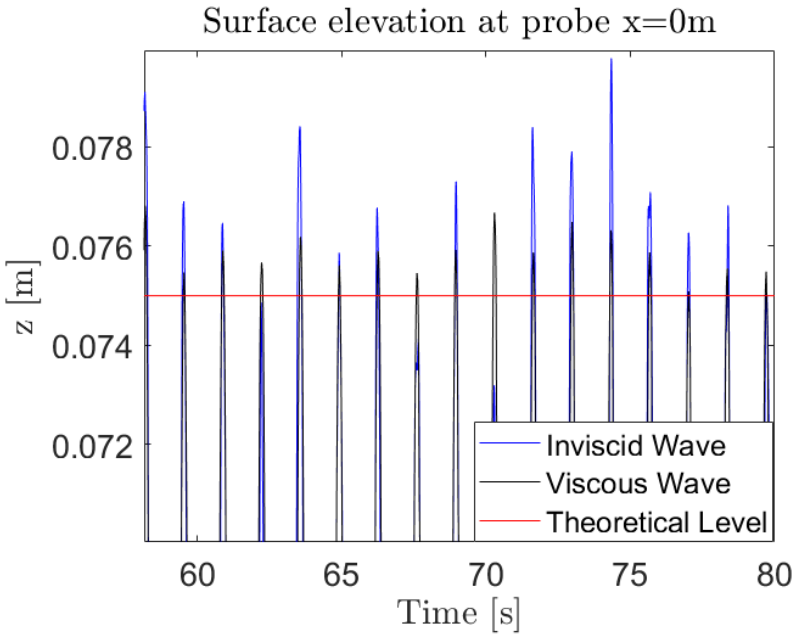

Figure C.17: Wave max amplitude comparison at y=6m, x=0m, oblique wave

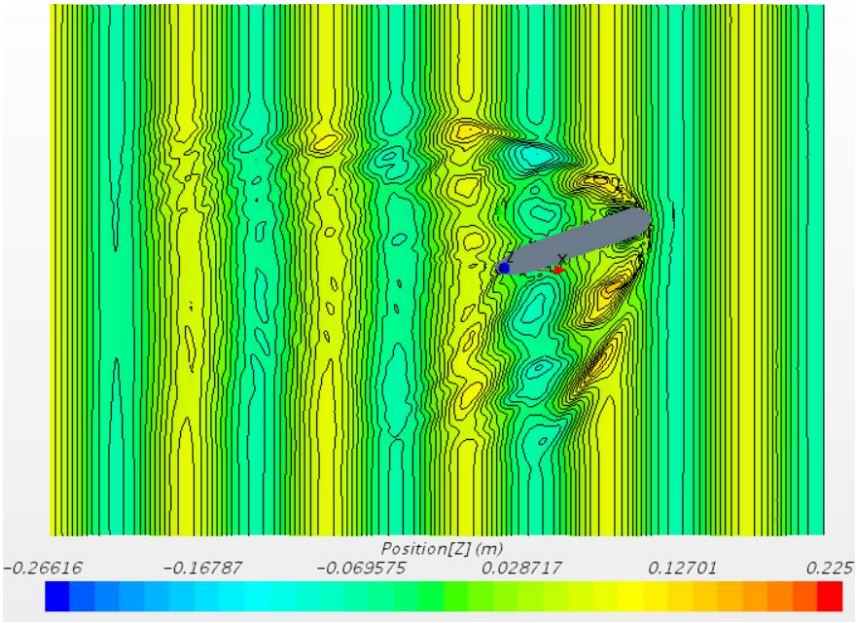

Figure C.18: Contour plot of the surface elevation, oblique wave

C.2 Inviscid Simulation

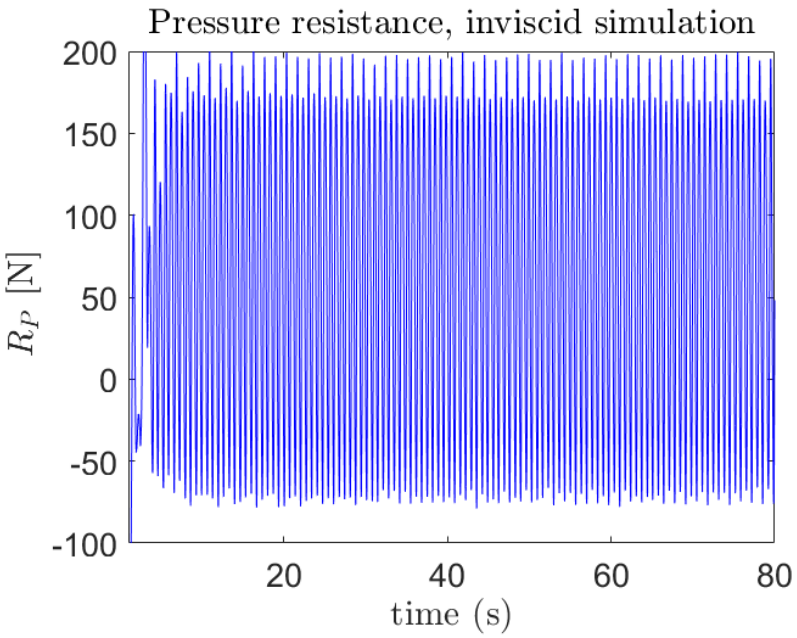

Figure C.19: Inviscid pressure resistance, oblique wave

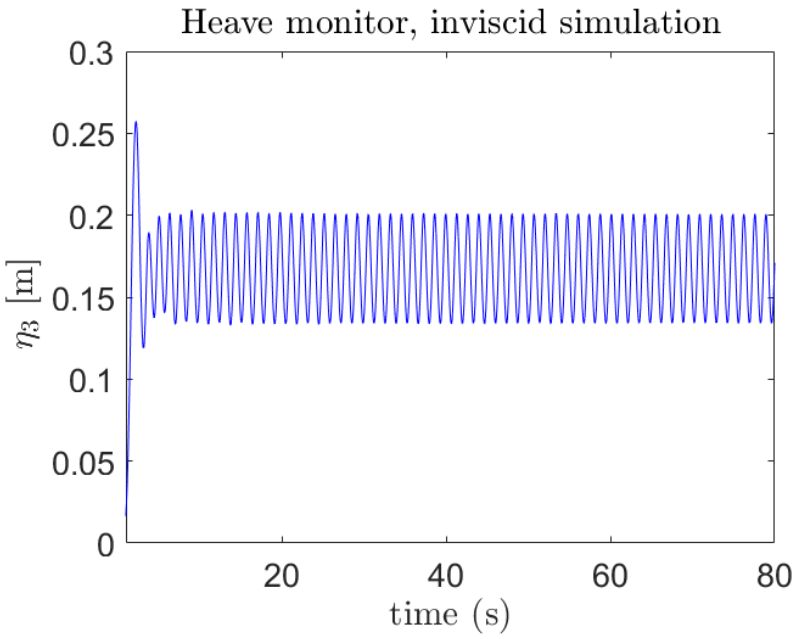

Figure C.20: Inviscid heave motion, oblique wave

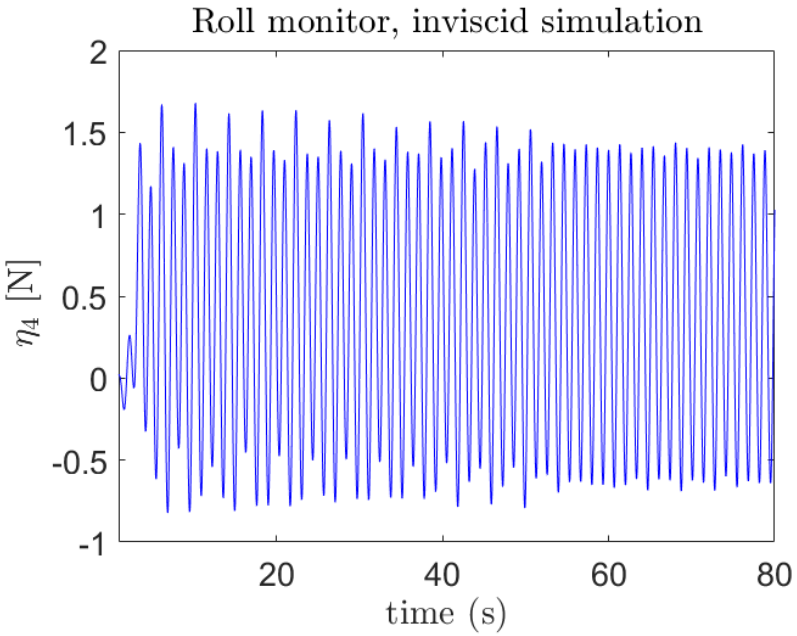

Figure C.21: Inviscid roll motion, oblique wave

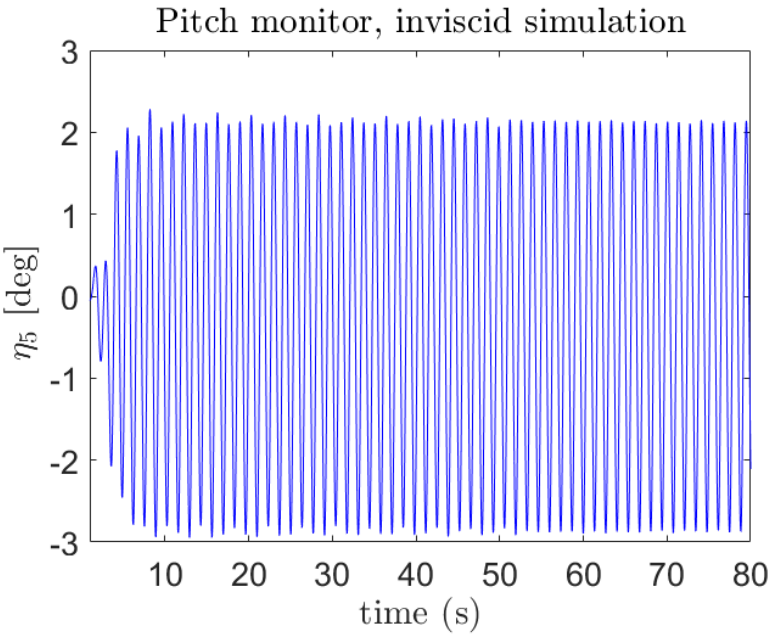

Figure C.22: Inviscid pitch motion, oblique wave